

A 5D gyrokinetic full- f global semi-Lagrangian code for flux-driven ion turbulence simulations



V. Grandgirard^{a,*}, J. Abiteboul^b, J. Bigot^c, T. Cartier-Michaud^a, N. Crouseilles^e,
G. Dif-Pradalier^a, Ch. Ehrlacher^a, D. Esteve^a, X. Garbet^a, Ph. Ghendrih^a, G. Latu^a,
M. Mehrenberger^d, C. Norscini^a, Ch. Passeron^a, F. Rozar^a, Y. Sarazin^a,
E. Sonnendrücker^b, A. Strugarek^f, D. Zarzoso^g

^a CEA, IRFM, 13108 Saint-Paul-lez-Durance Cedex, France

^b Max-Planck-Institut für Plasmaphysik, Boltzmannstr. 2, 85748 Garching, Germany

^c Maison de la Simulation, CEA Saclay, 91191 Gif-sur-Yvette Cedex, France

^d IRMA, 67084 Strasbourg Cedex, France

^e IRMAR, 35065 RENNES Cedex, France

^f GRPS, Physics Department, Montreal University, H3C 3J7 Montreal, Canada

^g Aix-Marseille Université, PIIM, UMR 7345 Marseille, France

ARTICLE INFO

Article history:

Received 9 June 2015

Received in revised form

25 April 2016

Accepted 9 May 2016

Available online 28 June 2016

Keywords:

Plasma turbulence

Gyrokinetic global full- f flux-driven simulations

Semi-Lagrangian method

High-performance computing

ABSTRACT

This paper addresses non-linear gyrokinetic simulations of ion temperature gradient (ITG) turbulence in tokamak plasmas. The electrostatic GYSELA code is one of the few international 5D gyrokinetic codes able to perform global, full- f and flux-driven simulations. Its has also the numerical originality of being based on a semi-Lagrangian (SL) method. This reference paper for the GYSELA code presents a complete description of its multi-ion species version including: (i) numerical scheme, (ii) high level of parallelism up to 500k cores and (iii) conservation law properties.

© 2016 Elsevier B.V. All rights reserved.

1. Introduction

In magnetic fusion devices, the power gain increases non-linearly with the energy confinement time. The quality of the plasma energy confinement then largely determines the size and therefore the cost of a fusion reactor. This confinement time is mainly governed by the plasma turbulence as deserved in such devices – leading to fluctuations with relative magnitude of a few percents in the hot core – and the associated transport. Understanding its origin and properties in view of a possible control is one of the critical issues in fusion science [1]. The inhomogeneities in density, temperature, and magnetic field place the plasma naturally out of thermodynamical equilibrium, and tend to excite several micro-instabilities over a wide spectral range. These plasmas

exhibit a low collisionality so that conventional fluid models are questionable and kinetic descriptions are more appropriate. A kinetic formalism is also needed to account for wave-particle interaction. In such first-principle descriptions of plasmas, the six dimensional evolution equation for the distribution function – Vlasov or Fokker-Planck equations – is solved for each species, coupled to the self-consistent equations for the electromagnetic fields, namely Maxwell's equations. Fortunately, as far as turbulent fluctuations are concerned, they develop at much lower typical frequencies than the high frequency cyclotron motion. Therefore, this 6D problem can be reduced to a 5D one by removing, using phase space reduction, the gyromotion and other high-frequency dynamics. The useful part of the distribution function then evolves in a five dimensional phase space generated by four slow variables and an adiabatic invariant. This model is known as the gyrokinetic model. For detailed gyrokinetic theory see review papers by Brizard & Hahm (2007) [2] and Krommes (2012) [3]. But even with this dimensional reduction, building such a simulation tool remains quite challenging.

* Corresponding author.

E-mail address: virginie.grandgirard@cea.fr (V. Grandgirard).

The first-principle gyrokinetic codes, developed for this purpose, make already an intensive use of massively parallel supercomputers and require state-of-the-art high performance computing (HPC). Nevertheless, solving 5D non-linear gyrokinetic equations for several ion species proves so challenging that to date no code is able to treat all the physics involved. Several strategies based on different simplifications have been developed to decrease these extreme numerical costs. We encourage the reader to refer to the paper by Garbet et al. (2010) [4] for an overview of these different strategies for numerical simulations and their comparisons with fusion experiments. A first strategy is to reduce the simulation domain to a small plasma volume aligned with the magnetic field lines and sufficiently small to neglect the radial variations of macroscopic quantities such as the density and temperature fields and their gradients. Such so called *flux-tube* codes (e.g. GS2 [5], GENE [6], GYRO [7], GKW [8]) have the advantages to drastically reduce CPU time and memory consumption compared to the *global* approach where computing over the whole plasma domain requires huge 3D meshes. Despite this constraint, a global approach must be considered whenever the “global” scales are comparable to that of the turbulence. This allows one in particular to address some aspects of the barrier physics. Gyrokinetic models can also be split in two distinct families with respect to the representation of the distribution function: either full- f or δf models. In the δf model, only perturbations with respect to some prescribed background equilibrium (usually Maxwellian in velocity) are computed. Conversely, in full- f models, the whole distribution function is evolved. Especially, the back reaction of turbulent transport is accounted for in the time evolution of the equilibrium. In global and full- f simulations, the turbulent regime is evanescent if no free energy is injected in the system to prevent the inevitable relaxation of equilibrium profiles below the – linear or non-linear – threshold of the underlying instability. A heat source is mandatory in view of exploring the long time, typically on energy confinement times, behavior of turbulence and transport, leading to the so-called *flux-driven* simulations.

Finally, the existing codes differ also by their numerical schemes which have evolved all along the last twenty-five years, in direct link with the evolution of HPC resources. Historically, particle in cell methods (PIC) – pioneered for gyrokinetics by Lee [9] – have been most popular, and represent widely adopted approaches to numerical simulations of kinetic plasmas. They used to be considered as the most efficient tool to describe plasma dynamics, essentially because they are capable of describing many physical phenomena in the full dimensional case, at relatively small computational costs. Many gyrokinetic codes are PIC codes. Let us mention, Parker’s code [10], Sydora’s code [11], PG3EQ [12], GTC [13], ELMFIRE [14], GT3D [15], ORB5 [16,17], GTS [18] and XGC1 [19]. However, it is well known that the relative numerical noise inherent to PIC methods constitutes a strong limiting factor to accurately describe the distribution function in phase space on long time scales. Moreover, the numerical noise only slowly decreases, like $1/\sqrt{N}$, when the number N of particles is increased. The main problem for non-linear gyrokinetic simulations is that the noise level *a priori* accumulates in time [20]. Even small errors in the evaluation of these moments can cause a systematic corruption of the simulation results on relatively short periods of time. Consequently, the reduction of numerical noise has been right from the start a matter of intense research, and many improvements have taken place during the past ten years, making use of different statistical methods: (i) control variate method of variance reduction (with δf scheme [21,10] or “adjustable control variate” method [22]); (ii) importance sampling (with “optimized loading” [23]). These techniques have enabled to reduce the numerical noise by orders of magnitude. Let us specifically mention the achievements made on the ORB5 gyrokinetic PIC-code

[17] on the noise issue, which are summarized in [24]. Another approach to avoid the issue of marker sampling noise is the Eulerian approach. It consists in discretizing the phase space on a fixed grid, and in applying finite differences, finite volumes and/or Fourier transforms to model the differential and integral operators (see e.g. [25] for a review). The main drawback stems from the fact that these numerical schemes are based on explicit time integration, so they are limited by the Courant–Friedrichs–Lewy (CFL) stability condition, which slaves the maximum time step to the grid space resolution. Several gyrokinetic codes are based on this approach as proved by this non-exhaustive list of Eulerian codes: GS2 [26,5], GENE [6,27], GYRO [7], GKV [28], GKW [29] and GT5D [30,31].

As described in the following, one peculiarity of the GYSELA code is to be based on a semi-Lagrangian method, which is a mix between PIC and Eulerian approaches. The objective is to try to take advantages of both methods, namely limited numerical dissipation with limited numerical noise. We had shown good properties of energy conservation of semi-Lagrangian scheme for a 4D drift-kinetic model [32]. The GYSELA code exhibits now not only accurate radial force balance [33] but also good properties of local conservation laws for charge density, energy and toroidal momentum [34]. These conservation properties are detailed in the following in Section 5. Such conservation properties are comparable to those obtained with the GT5D code [35], which is based on a fourth-order non-dissipative conservative finite difference scheme [36,30] which conserves both L^1 and L^2 norms. Anyway, each of these three numerical approaches – PIC, Eulerian or semi-Lagrangian – has advantages and drawbacks (see [37] for a review). But for sure, the wide variety of gyrokinetic codes, coming from all these different choices, is a strength for the fusion community. Indeed, due to the extremely challenging computing requirements, each gyrokinetic code runs at the limit of its applicability range. For instance significant advances like taking into account kinetic electrons and electromagnetic effects are extremely time consuming for global codes. This has been firstly achieved in the GYRO code [38], then in the GENE code [39] and in the ORB5/NEMORB code¹ [40] and more recently in the GKW code [41]; this list is not exhaustive. Conversely, the full- f and flux-driven regimes are two necessary ingredients to investigate, among others, the mechanism underlying self-consistent transport barrier creation. Benchmarks between the different approaches are therefore primordial (e.g. [42,43]). Difficulties reside generally in finding common domains of validity (set of parameters, initial and boundary conditions, ...). The choice of a global full- f approach has been done for the electrostatic non-linear 5D gyrokinetic code GYSELA described in this paper. Electrons are at present considered adiabatic. Within the community of the 5D gyrokinetic codes, GYSELA is close to GT5D code [44] in the sense that they are both global full- f flux-driven codes. They mainly differ by their numerical schemes and their flux driven choice where the source term is compensated by a sink term in GT5D [45].

In the following, all the components of the semi-Lagrangian GYSELA code will be detailed both in terms of physical equations and numerical methods as well as the verification and benchmarks that have been performed. Such flux-driven ITG simulations are extremely challenging and would not be possible without a high level of parallelism which will also be addressed. The code is currently using Petaflops HPC resources and is actively preparing its evolution for the future exascale era. The paper is

¹ NEMORB seems to have been the first electromagnetic branch of ORB5. Apparently, the ORB groups have meanwhile decided to avoid distinction between the different branches. So for the rest of the paper, we will refer to the code with the unique ORB5 name.

a comprehensive description of the multi-ion species version of the code with a detailed description of all the numerical schemes employed and with a precise presentation of the parallelization of the code. The last same exercise has been performed in 2006 [32] on the initial 4D drift-kinetic version of the code. The upgrade to a 5D gyrokinetic version in 2007 [46] and the recent development of a multi-ion version [47] have completely changed the needs in parallelization. Several important physical results have been obtained with the 5D version of the GYSELA code in the flux-driven regime, although there was so far no reference paper for it. These results will be highlighted in the various sections of the paper. They deal with: (i) flux driven regime and non-local transport [48,49], (ii) neoclassical theory with the implementation of a collision operator [50,51], (iii) poloidal and toroidal rotation issues and [52,53] (iv) the possible control of turbulence by means of sheared flows, including transport barrier generation and stability [54,55]. Each of these physical studies has been made possible thanks to the constant upgrade of the code and critical numerical developments, which are exhaustively detailed (and benchmarked whenever it is relevant) in the present paper. It is organized as follows. The physical model is presented in Section 2. The numerical methods and the hybrid OpenMP/MPI parallelism are described in Section 3. The code verification via invariance tests and benchmarks are detailed in Section 4. The conservation law properties are analyzed in Section 5. Discussion and conclusion close the paper in Section 6.

2. GYSELA gyrokinetic global full-f model

GYSELA is a global code presently used with a simplified concentric circular magnetic configuration (Section 2.2) similar to the Tore Supra equilibria. The new version of the code still considers adiabatic electrons but the possibility to address transport of impurities has been added. The time evolution of the full distribution function of each ion species (major species as e.g. Deuterium + one minor impurity) is governed by a 5D non-linear gyrokinetic Vlasov equation (Section 2.3) self-consistently coupled to a 3D Poisson equation (Section 2.4). The required gyroaverage operator (Section 2.5) that used to be approximated by a Padé expansion in the past versions of GYSELA can now be computed with a direct average on gyro-circles. Collisions are taken into account. With a linearized intra-species collision operator (Section 2.7) neoclassical effects are recovered. Inter-species collisional transfers are now also considered (Section 2.8). The problem of initialization and radial boundary conditions inherent to global full-f codes like GYSELA are addressed in Section 2.6. Concerning boundary conditions, three modes are available in the code: (i) the *fixed-gradient* mode where the temperature profile is fixed at both radial boundaries, corresponding to decaying turbulence regimes (relaxation of equilibrium profiles below instability thresholds cannot be avoided); (ii) the *gradient-driven* mode, equivalent to the previous one but where gradient profiles are maintained by an artificial Krook-type operator and finally (iii) the *flux-driven mode* (the most often used) where temperature is still fixed at the outer boundary but can evolve freely at the inner one. In the gradient-driven mode the strength of the drag force of the Krook operator governs the dynamics of the mean (flux surface averaged) gradient profiles: they remain all the more stucked to their initial value if the Krook coefficient ν_k is large. More precisely, significant departures of the mean profiles w.r.t. their initial value are only possible on short time scales ($t \ll \nu_k^{-1}$), while the long time behavior ensures that they remain unchanged when time averaged. Concerning the flux-driven mode, the turbulence is forced with a constant-in-time incoming flux generated by a heat source independent of the distribution function (Section 2.9)

leading to possible long-time simulation. A simulation over several confinement times has been recently performed for comparison to Tore-Supra experiments [56].

2.1. Toroidal coordinate system

Let us introduce the notations used in the paper. We consider a set of coordinates labeled $\{x^i\}$, the metric tensor $\{g_{ij}\}$ is the product of the transposed Jacobian matrix J^T and the Jacobian matrix J , i.e $\{g_{ij}\} = J^T J$. For a set of cartesian coordinates X^i , the elements J_{ij} of the Jacobian matrix are defined as $J_{ij} = \partial_{x^i} X^j$. Let g represents the determinant of the metric tensor (i.e $g = \det\{g_{ij}\}$), then the Jacobian in space J_x is defined as $J_x = \sqrt{g}$ and is equal to $J_x = [(\nabla x^1 \times \nabla x^2) \cdot \nabla x^3]^{-1}$, i.e the volume element is $J_x d^3\mathbf{x}$. The tensor $\{g^{ij}\}$ is the inverse of the tensor $\{g_{ij}\}$. The element of the contravariant metric tensor verifies the relation $g^{ij} = \nabla x^i \cdot \nabla x^j$. With these notations, each vector \mathbf{A} can be defined in terms of its covariant components A_i as $\mathbf{A} = A_i \nabla x^i$ and the equivalent norm is given by $\|\mathbf{A}\| = \sqrt{(A_1)^2 g^{11} + (A_2)^2 g^{22} + (A_3)^2 g^{33}}$. At present, in the code, the coordinate system used is the toroidal one, i.e the set of coordinates (x^1, x^2, x^3) is equal to (r, θ, φ) where r is the radial position, θ is the poloidal angle and φ the toroidal angle. Therefore, $g^{11} = g^{rr} = 1$, $g^{22} = g^{\theta\theta} = 1/r^2$, $g^{33} = g^{\varphi\varphi} = 1/R^2$ and $g^{ij} = 0$ for all $i \neq j$. $R(r, \theta) = R_0 + r \cos \theta$ with R_0 the major radius of the torus at the magnetic axis. The Jacobian J_x is then equal to $J_x = rR$.

2.2. Simplified magnetic configuration and current

Consistently with the chosen coordinate system, the magnetic topology is fixed and consists of concentric toroidal magnetic surfaces with circular poloidal cross-sections. The magnetic field \mathbf{B} is defined as $\mathbf{B} = (B_0 R_0 / R) [\zeta(r) \mathbf{e}_\theta + \mathbf{e}_\varphi]$ with $\zeta(r) = r / (q R_0)$. B_0 corresponds to the magnetic field on the magnetic axis. The vectors $\mathbf{e}_\theta = r \nabla \theta$ and $\mathbf{e}_\varphi = R \nabla \varphi$ are the unit vectors in the poloidal and toroidal periodic directions. The safety factor profile $q(r)$ is defined by three parameters q_1 , q_2 , and q_3 as $q(r) = q_1 + q_2 \exp(q_3 \log(r/a))$. With this choice of angles, $\mathbf{B} \cdot \nabla \varphi / \mathbf{B} \cdot \nabla \theta = q(r) R_0 / R$, namely the local field line pitch depends not only on r but also on θ . The current is decoupled from the field and the magnetic field is assumed to satisfy the Ampère equation, but not the force balance equation. Then the Ampère equation leads to a current of the form $\mu_0 \mathbf{J} = \mu_0 J_T R \nabla \varphi$ with $\mu_0 J_T = \frac{B_0 R_0}{R} \frac{\zeta}{r} \left(1 + \frac{r}{\zeta} \frac{d\zeta}{dr} - \frac{r}{R} \cos \theta\right)$.

2.3. Full-f gyrokinetic Vlasov equation

Let us consider the gyro-center coordinate system $(\mathbf{x}_G, v_{G\parallel}, \mu_s)$ where \mathbf{x}_G corresponds to 3D space coordinates, $v_{G\parallel}$ is the velocity parallel to the magnetic field line and $\mu_s = m_s v_{G\perp}^2 / (2B)$ the magnetic moment. Let F_s be the particle distribution function of species s and \bar{F}_s the one associated to the guiding-centers. The global gyrokinetic code GYSELA models for each species s , the time evolution of the guiding-center distribution function \bar{F}_s , with no separation between equilibrium and perturbation. The non-linear time evolution of \bar{F}_s is governed by the 5D collisional gyrokinetic equation described by Brizard and Hahm [2]

$$\partial_t \bar{F}_s - [H, \bar{F}_s]_{GC} = \mathcal{R} h s (\bar{F}_s) \quad (1)$$

where H the Hamiltonian of the system is defined as $H = \frac{1}{2} m_s v_{G\parallel}^2 + \mu_s B + q_s \bar{U}$ and where $[\dots]_{GC}$ are the gyrokinetic Poisson brackets

expressed as (see equation (150) in [2])

$$[X, Y]_{GC} = \frac{\mathbf{B}_s^*}{m_s B_{\parallel s}^*} \cdot (\nabla X \partial_{v_{G\parallel}} Y - \partial_{v_{G\parallel}} X \nabla Y) - \frac{\mathbf{b}}{q_s B_{\parallel s}^*} \cdot (\nabla X \times \nabla Y) \quad (2)$$

with $\mathbf{b} = \mathbf{B}/\|\mathbf{B}\|$ the unit vector along the magnetic field line at the guiding-center position. Here, $\bar{U} = \mathcal{J}_\mu \cdot U$ is the gyro-average of the fluctuating electrostatic potential U . It corresponds to an average over a cyclotron motion: $\mathcal{J}_\mu \cdot U = \int_0^{2\pi} U \frac{d\varphi_c}{2\pi}$, where φ_c stands for the cyclotron phase. This gyro-average operator \mathcal{J}_μ will be discussed in more detail in Section 2.5. The scalar $B_{\parallel s}^*$ corresponds to the volume element in guiding-center velocity space. It is simply $B_{\parallel s}^* = \mathbf{B}_s^* \cdot \mathbf{b}$ with \mathbf{B}_s^* defined as

$$\mathbf{B}_s^* \equiv \mathbf{B} + \frac{m_s}{q_s} v_{G\parallel} \nabla \times \mathbf{b} \quad (3)$$

i.e

$$B_{\parallel s}^* \equiv B + \frac{m_s}{q_s} v_{G\parallel} \mathbf{b} \cdot (\nabla \times \mathbf{b}). \quad (4)$$

In our case, the right hand side $\mathcal{R}hs$ of the previous Boltzmann equation (1) is given by

$$\mathcal{R}hs(\bar{F}_s) = B_{\parallel s}^* (\mathcal{D}_r(\bar{F}_s) + \mathcal{K}(\bar{F}_s) + \mathcal{C}(\bar{F}_s) + \mathcal{S})$$

where \mathcal{D}_r and \mathcal{K} are respectively a diffusion term and a Krook operator applied on a radial buffer region (see Section 2.10), \mathcal{C} corresponds to a collision operator (see Section 2.7) and \mathcal{S} refers to source terms which are detailed in Section 2.9.

Let us define the Poisson bracket as $[F, G] = \mathbf{b} \cdot (\nabla F \times \nabla G)$, and the parallel projection as $\nabla_{\parallel}^* F = \mathbf{b}_s^* \cdot \nabla F$. Let b_k represent the covariant components of the unitary magnetic field vector \mathbf{b} and J_x the Jacobian in space of the system. Then it can be easily checked that $[F, G] = J_x^{-1} \epsilon^{ijk} \partial_i F \partial_j G b_k$ where ϵ^{ijk} is the Levi-Civita symbol and $\mathbf{b}_s^* \cdot \nabla F = \mathbf{b}_s^{*i} \partial_i F$. By using this formalism, it can be proven that the Hamiltonian form (1) is equivalent to the following conservative form

$$B_{\parallel s}^* \frac{\partial \bar{F}_s}{\partial t} + \nabla \cdot \left(B_{\parallel s}^* \frac{d\mathbf{x}_G}{dt} \bar{F}_s \right) + \frac{\partial}{\partial v_{G\parallel}} \left(B_{\parallel s}^* \frac{dv_{G\parallel}}{dt} \bar{F}_s \right) = \mathcal{R}hs(\bar{F}_s) \quad (5)$$

where the evolution of the gyro-center coordinates of species s are described (within the electrostatic limit) by:

$$\frac{d\mathbf{x}_G^i}{dt} = v_{G\parallel} \mathbf{b}_s^* \cdot \nabla \mathbf{x}_G^i + \mathbf{v}_{E \times B_s} \cdot \nabla \mathbf{x}_G^i + \mathbf{v}_{D_s} \cdot \nabla \mathbf{x}_G^i \quad (6)$$

$$m_s \frac{dv_{G\parallel}}{dt} = -\mu_s \mathbf{b}_s^* \cdot \nabla B - q_s \mathbf{b}_s^* \cdot \nabla \bar{U} + \frac{m_s v_{G\parallel}}{B} \mathbf{v}_{E \times B_s} \cdot \nabla B \quad (7)$$

where \mathbf{b}_s^* is defined as²

$$\mathbf{b}_s^* = \frac{\mathbf{B}}{B_{\parallel s}^*} + \frac{m_s v_{G\parallel}}{q_s B_{\parallel s}^* B} \nabla \times \mathbf{B}. \quad (8)$$

The i th contravariant components of the ' $\mathbf{E} \times \mathbf{B}$ ' drift are given by

$$\mathbf{v}_{E \times B_s} \cdot \nabla \mathbf{x}_G^i = \mathbf{v}_{E \times B_s}^i = \frac{1}{B_{\parallel s}^*} [\bar{U}, \mathbf{x}_G^i] \quad (9)$$

and the i th contravariant components of the 'grad- \mathbf{B} ' and 'curvature' drifts read (at low $\beta = nT/(B^2/2\mu_0)$ limit)

$$\mathbf{v}_{D_s} \cdot \nabla \mathbf{x}_G^i = \mathbf{v}_{D_s}^i = \left(\frac{m_s v_{G\parallel}^2 + \mu_s B}{q_s B_{\parallel s}^* B} \right) [B, \mathbf{x}_G^i]. \quad (10)$$

Besides, using the fact that the axi-symmetric equilibrium is determined by three of the ideal MagnetoHydroDynamic (MHD) equations $\nabla p = \mathbf{J} \times \mathbf{B}$, $\nabla \times \mathbf{B} = \mu_0 \mathbf{J}$ and $\nabla \cdot \mathbf{B} = 0$, the i th contravariant components of \mathbf{b}_s^* appearing in Eq. (6) read

$$\mathbf{b}_s^* \cdot \nabla \mathbf{x}_G^i = \mathbf{b}_s^{*i} = \frac{\mathbf{B} \cdot \nabla \mathbf{x}_G^i}{B_{\parallel s}^*} + \frac{m_s v_{G\parallel} \mu_0 \mathbf{J} \cdot \nabla \mathbf{x}_G^i}{q_s B_{\parallel s}^* B}. \quad (11)$$

2.4. Self-consistent coupling with the quasi-neutrality equation

The electron density n_e is supposed to follow an adiabatic (Boltzmann) response on a flux surface, namely $n_e(\mathbf{x}, t) = n_{e0}(r) \exp(e [U(\mathbf{x}, t) - \langle U \rangle_{FS}(r, t)]/T_e(r))$ with T_e the electron temperature. $\langle U \rangle_{FS}$ represents the flux surface average of the electrostatic potential U , i.e

$$\langle U \rangle_{FS}(r) = \frac{\int U(r, \theta, \varphi) J_x \, d\theta \, d\varphi}{\int J_x \, d\theta \, d\varphi}.$$

Let us define, for each species s , its initial radial density profile n_{s0} and its concentration $c_{s0} \equiv n_s/n_{e0}$. We also assume that $n_{e0} = \sum_s Z_s n_{s0}$ so that $\sum_s c_{s0} Z_s = 1$. Under these assumptions, the quasi-neutrality equation, self-consistently coupled to the gyrokinetic equation (5), reads

$$-\frac{1}{n_{e0}} \sum_s Z_s \nabla_{\perp} \cdot \left(\frac{n_{s0}}{B_0 \Omega_s} \nabla_{\perp} U \right) + e \left(\frac{U - \langle U \rangle_{FS}}{T_e} \right) = \frac{1}{n_{e0}} \sum_s Z_s (n_{G_s} - n_{G_s,eq}) \quad (12)$$

with $\Omega_s = q_s B_0/m_s$ and $\nabla_{\perp} = (\partial_r, \frac{1}{r} \partial_\theta)$. Here, the polarization density (first term of Eq. (12)) is approximated by its expression in the limit of large wavelengths with respect to the Larmor radius (limit $k_{\perp} \rho_s \ll 1$). The gyro-center density n_{G_s} of species s is defined by $n_{G_s}(\mathbf{x}, t) = \int J_v \, d\mu \, dv_{G\parallel} \mathcal{J}_\mu \cdot \bar{F}_s(\mathbf{x}, \mathbf{v}, t)$ – where $J_v = (2\pi B_{\parallel s}^*/m_s)$ stands for the Jacobian in the velocity space – similarly $n_{G_s,eq}$ is the gyro-center density for $\bar{F}_s = \bar{F}_{s,eq}$. In practice, the right hand side of (12) the charge density of guiding-centers ρ , is computed as

$$\rho(\mathbf{x}, t) = \frac{1}{n_{e0}} \sum_s Z_s \int d\mu \mathcal{J}_\mu \cdot \left[\int J_v \, dv_{G\parallel} (\bar{F}_s - \bar{F}_{s,eq}) \right]. \quad (13)$$

To avoid the problem of the singularity in $1/r$, the problem is solved within a ring $r_{\min} \leq r \leq r_{\max}$ where $r_{\min} \geq 10^{-5}$. One difficulty with Eq. (12) is to deal with the flux surface average term $\langle U \rangle_{FS}$. This term is non-linear in θ , because the space Jacobian depends on θ . Therefore, it does not allow one to project simply in 2D Fourier space. To overcome this problem, solving (12) is performed in two steps as proposed in [57]. Let us define the differential operator $\mathcal{L} = -\frac{1}{n_{e0}} \sum_s Z_s \nabla_{\perp} \cdot \left(\frac{n_{s0}}{B_0 \Omega_s} \nabla_{\perp} \cdot \right)$ and $\langle \cdot \rangle_{\theta, \varphi}$ the average on θ and φ directions. Then, the first step consists in finding \mathcal{U} solution of the following differential system,

$$\left(\mathcal{L} + \frac{e}{T_e} \right) \mathcal{U} = \rho - \langle \rho \rangle_{\theta, \varphi} \quad (14)$$

with $\mathcal{U}(r, \theta, \varphi) = U(r, \theta, \varphi) - \langle U \rangle_{\theta, \varphi}(r)$.

² Let us mention that in this definition \mathbf{b}_s^* is not equal to $\mathbf{B}_s^*/B_{\parallel s}^*$ but equal to $\mathbf{b}_s^* = \frac{\mathbf{B}_s^*}{B_{\parallel s}^*} - \frac{m_s v_{G\parallel}}{q_s B_{\parallel s}^* B} (\mathbf{b} \times \frac{\nabla B}{B})$.

The second step consists in solving the following 1D radial differential equation

$$\mathcal{L}\langle U \rangle_{\text{FS}} = \langle \rho \rangle_{\theta, \varphi} + \left(\mathcal{L} + \frac{e}{T_e} \right) \langle \mathcal{U} \rangle_{\text{FS}}. \quad (15)$$

In this equation, φ plays the role of a parameter. A Fourier projection is performed in the θ direction. In the radial direction, for both differential systems (14) and (15), finite differences are used. Finally, the electrostatic potential is reconstructed with the formula $U = \mathcal{U} - \langle U \rangle_{\text{FS}} + \langle \mathcal{U} \rangle_{\text{FS}}$. For both Eqs. (14) and (15), Dirichlet boundary conditions are applied at the outer boundary at r_{max} , while Dirichlet or Neumann can be chosen at the inner boundary at r_{min} . Notice that these boundary conditions then apply to \mathcal{U} , not to the actual electric potential U . Given the relationship between U and \mathcal{U} , imposing the Dirichlet condition $\mathcal{U}(r_{\text{BC}}) = 0$, with $r_{\text{BC}} = \{r_{\text{min}}, r_{\text{max}}\}$, is then equivalent to the following conditions on U : $U(r_{\text{BC}}) = \langle U \rangle_{\theta, \varphi}(r_{\text{BC}})$ and $\langle U \rangle_{\text{FS}}(r_{\text{BC}}) = 0$. The Neumann condition proceeds in a similar way. In GYSELA, it can be only applied to the inner boundary provided $r_{\text{min}} \leq 10^{-2}$. In this case, $J_x(r_{\text{min}}, \theta)$ is fairly independent of θ , so that the flux surface average is almost equal to the average over both angles: $\langle \cdot \rangle_{\text{FS}} \approx \langle \cdot \rangle_{\theta, \varphi}$. In the framework of this approximation, imposing the Neumann condition $\partial_r \mathcal{U}(r_{\text{min}}) = 0$ is equivalent to $\partial_r U(r_{\text{min}}) = \partial_r \langle U \rangle_{\theta, \varphi}(r_{\text{min}}) \approx \partial_r \langle U \rangle_{\text{FS}}(r_{\text{min}}) = 0$.

2.5. Gyro-average operator

The gyro-radius ρ_s is transverse to $\mathbf{b} = \mathbf{B}/B$ and depends on the gyrophase angle φ_c , i.e. $\rho_s = (\mathbf{b} \times \mathbf{v})/\Omega_s = \rho_s (\cos \varphi_c \mathbf{e}_{\perp 1} + \sin \varphi_c \mathbf{e}_{\perp 2})$. Here $\mathbf{e}_{\perp 1}$ and $\mathbf{e}_{\perp 2}$ are the unit vectors of a basis in the plane perpendicular to the magnetic field direction \mathbf{b} . Let \mathbf{x}_G be the guiding-center radial coordinate and \mathbf{x} the position of the particle in real space. These two quantities differ by a Larmor radius ρ_s as $\mathbf{x} = \mathbf{x}_G + \rho_s$. The gyro-average \bar{g} of any function g depending on the spatial coordinates corresponds to the following operation

$$\begin{aligned} \bar{g}(\mathbf{x}_G, v_{\perp}) &= \oint_0^{2\pi} \frac{d\varphi_c}{2\pi} g(\mathbf{x}) \\ &= \left\{ \oint_0^{2\pi} \frac{d\varphi_c}{2\pi} \exp(\rho_s \cdot \nabla) \right\} g(\mathbf{x}_G). \end{aligned} \quad (16)$$

The operator $e^{\rho_s \cdot \nabla}$ corresponds to the change of coordinates $(\mathbf{x}, \mathbf{p}) \rightarrow (\mathbf{x}_G, \mathbf{p}_G)$. This gyro-average process consists in computing an average on the Larmor circle. It weakens fluctuations that develop at sub-Larmor scales. Introducing $\hat{g}(\mathbf{k})$ the Fourier transform of g , with \mathbf{k} the wave vector, it is possible to prove that the gyro-average operation reads

$$\bar{g}(\mathbf{x}_G, v_{\perp}) = \int_{-\infty}^{+\infty} \frac{d^3 \mathbf{k}}{(2\pi)^3} J_0(k_{\perp} \rho_s) \hat{g}(\mathbf{k}) e^{i\mathbf{k} \cdot \mathbf{x}_G} \quad (17)$$

where k_{\perp} is the norm of the transverse component of the wave vector $\mathbf{k}_{\perp} = \mathbf{k} - (\mathbf{b} \cdot \mathbf{k})\mathbf{b}$, and J_0 is the Bessel function³ of first order. Considering the expression (17), in Fourier space the gyro-average reduces to the multiplication by the Bessel function of argument $k_{\perp} \rho_s$. This operation is straightforward in simple geometry with periodic boundary conditions, such as in local codes. Conversely, in the case of global codes, the use of Fourier transform is not applicable for two main reasons: (i) radial boundary conditions are non periodic, and (ii) the radial dependence of the Larmor radius has to be accounted for. Several approaches have been developed to overcome this difficulty.

2.5.1. A Padé approximation for the gyro-average operator

The first one, currently used in the code, consists in simplifying the treatment of the gyro-average operator by approximating the Bessel function with a Padé expansion $J_{\text{Padé}}(k_{\perp} \rho_s) = 1/[1 + (k_{\perp} \rho_s)^2/4]$ (e.g. see [58]). The advantage of this Padé representation is that it does no longer requires to use the Fourier space as required by the Bessel function. Indeed, since it involves k_{\perp}^2 , it can easily be treated in the configuration space by using the relation $\nabla_{\perp}^2 \leftrightarrow -k_{\perp}^2$. Using this Laplacian equivalence, the gyro-average operation of any g function is defined such that each m Fourier mode of \bar{g} is solution of the equation

$$\left[1 - \frac{1}{2\Omega_s^2} \frac{B_0}{m_s} \mu_s \left(\frac{\partial^2}{\partial r^2} + \frac{1}{r} \frac{\partial}{\partial r} - \frac{m^2}{r^2} \right) \right] \bar{g}^m(r, \varphi) = g^m(r, \varphi) \quad (18)$$

where at first approximation $B(r, \theta)$ has been replaced by B_0 to be consistent with the quasi-neutrality equation. In this differential equation, first and second derivatives are computed using a Taylor expansion of second order leading to a tridiagonal matrix system. This Padé approximation is asymptotically correct in the large wavelength limit $k_{\perp} \rho_s \ll 1$ (indeed: $J_0(k_{\perp} \rho_s) \approx 1 - k_{\perp}^2 \rho_s^2/4$ for $k_{\perp} \rho_s \ll 1$), while keeping $J_{\text{Padé}}$ finite in the opposite limit $k_{\perp} \rho_s \rightarrow \infty$. The drawback is a filtering of small scales: in the limit of large arguments $x \rightarrow \infty$, $J_{\text{Padé}}(x) \approx 4/x^2$, whereas $J_0(x) \approx (2/\pi x)^{1/2} \cos(x - \pi/4)$.

2.5.2. Integration on gyro-circles using Hermite interpolation

A second widespread method for this gyro-averaging process is to use a quadrature formula. In this context, the integral over the gyro-ring is usually approximated by a sum over four points or more on the gyro-ring [9]. This is rigorously equivalent to considering the Taylor expansion of the Bessel function at order two in the small argument limit, namely $J_0(k_{\perp} \rho_s) \simeq 1 - (k_{\perp} \rho_s)^2/4$, and equivalent to computing the transverse Laplacian at second order using finite differences. This method has been extended to achieve accuracy for large Larmor radius [23], i.e. the number of points (starting with four) is linearly increased with the gyro-radius to guarantee the same number of points per arclength on the gyro-ring. In this approach – used e.g. in [15] and [17] – the points that are equidistantly distributed over the ring are rotated for each particle (or marker) by a random angle calculated every time step. This is performed on a finite element formalism and enables therefore high order accuracy by keeping the matricial formulation. In [59] the influence of the interpolation operator (which is of great importance when the quadrature points do not coincide with the grid points) has been studied and it is shown that the cubic splines are appropriate. The direct integration on gyro-circles proposed in [59] has been recently generalized to arbitrary coordinates [60] and implemented in the code. For the distribution function the gyro-average operator is applied on $\bar{F}_s - \bar{F}_{s,eq}$ to deal with values close to 0 at the domain boundaries. Two interpolations – cubic splines and Hermite polynomial – have been tested on analytical cases and basic gyrokinetic simulations with a 4D drift-kinetic model, one Larmor radius and the standard linear Cyclone benchmark case (see [60] for more details and comparison with Padé approximation). Both appear to give the same results. However, the Hermite interpolation is slightly faster and its local character is more favorable for parallelization. The number of points per circle is an input parameter comprised between 4 and 16. There is no adaptive number of points depending on the Larmor radius value because the CPU time is in fact determined by the maximum number. As shown in [60] the method converges with the number of points, so there is no interest in decreasing the number of points at small radius. It is shown in [61] that 16 points is a good compromise between accuracy and CPU time consumption (2 times slower than the previous Padé

³ The Bessel function of the first kind are defined as $J_n(z) = \frac{i^{-n}}{\pi} \int_0^{\pi} \exp(iz \cos \theta) \cos(n\theta) d\theta$.

approximation due to its higher algorithmic complexity). All numerical results presented in the following are performed with the Padé approximation. The reason for not choosing the Hermite interpolation is just chronological: this latter method has been developed only recently. First analyses of new simulations with gyro-average operators based on Hermite show similar results in terms of conservation laws. The impact on non-linear cases will be addressed in a future paper.

2.6. Initial and boundary conditions

Boundary conditions are periodic in θ and φ directions. Concerning the radial direction, GYSELA is a *global* code, *i.e.* it considers a large fraction of the plasma radius. This is in contrast to flux-tube codes which focus on a small volume around magnetic field lines by proceeding from a scale separation assumption, the fluctuation scale length being smaller than that of the equilibrium. In such codes, periodicity is almost always assumed along the radial direction. Conversely, global codes as GYSELA face the delicate problem of radial boundary conditions. Non-axisymmetric fluctuations of the electric potential and of the distribution function – *i.e.* $(m, n) \neq (0, 0)$ modes, with m and n the poloidal and toroidal wave numbers – are forced to zero at both radial boundaries of the simulated domain. As far as the axisymmetric component is concerned, the value of the potential is prescribed at the outer boundary, while the radial electric field is set to zero at the inner boundary. In addition, so as to avoid possible numerical instabilities, which might occur in the case where turbulent fluctuations reach the frontiers of the simulation domain, buffer regions have been added at both radial boundaries. They are characterized by non-vanishing ad-hoc dissipative coefficients, which aim at keeping all gradients finite and damping out all fluctuations (see Section 2.10).

Initial conditions consist of an equilibrium distribution function $\bar{F}_{s,eq}$ perturbed by a sum of accessible (m, n) Fourier modes (m and n being the poloidal and toroidal wave numbers, respectively). That means, $\bar{F}_s = \bar{F}_{s,eq} + \delta\bar{F}_s$ where the perturbation part $\delta\bar{F}_s$ reads $\delta\bar{F}_s = \bar{F}_{s,eq} g(r) h(v_{G\parallel}) \delta p(\theta, \varphi)$ with $\delta p(\theta, \varphi) = \sum_{m,n} \epsilon \cos(m\theta + n\varphi + \delta_{mn})$ where the amplitude ϵ is fixed and the phases δ_{mn} have arbitrary values. The radial function $g(r)$ (resp. $h(v_{G\parallel})$) has a polynomial dependence and vanishes at both radial (resp. $v_{G\parallel}$) boundaries. Concerning the initialization of the equilibrium distribution function two choices are possible: (i) the first one is a local conventional Maxwellian, (ii) and the second one is a *canonical* Maxwellian, *i.e.* depends on the motion invariants. The Maxwellian distribution function is defined as

$$\bar{F}_{s,eq}(r, E) = n_{s0}(r) \times [2\pi T_s(r)/m_s]^{-3/2} \exp\left(-\frac{E}{T_s(r)}\right) \quad (19)$$

where E stands for the kinetic energy $m_s v_{G\parallel}^2/2 + \mu B(r, \theta)$ which is the second invariant of the system (at vanishing electric potential). The initial radial profiles of the ion temperature and density (respectively $T_s(r)$ and $n_{s0}(r)$) are deduced by numerical integration of their gradient profiles given by the two parameters κ and Δr : $d \log T_s(r)/dr = -\kappa T_s \cosh^{-2}((r - r_p)/\Delta r T_s)$ with r_p corresponding to the middle of the radial box. $\bar{F}_{s,eq}$ is constant on a magnetic surface labeled by the radial coordinate r . As shown in [33], such initial state does not constitute an equilibrium of the system solved by GYSELA at vanishing electric field. A stationary equilibrium of the collisionless equations of the code must depend on the three motion invariants, namely the adiabatic invariant μ , the total energy E and the toroidal kinetic momentum $P_\varphi = q_s \psi + m_s R v_\varphi$ with ψ the poloidal flux and v_φ the toroidal fluid velocity. In GYSELA, a convenient choice for this equilibrium is provided by the canonical Maxwellian (19) in which the radial coordinate r is replaced –

as proposed in [62] – by an effective radial coordinate \bar{r} , with the dimension of a length, derived from P_φ

$$\bar{r} = r_p - \frac{q_p}{r_p} \left[\psi(r) - \psi(r_p) \right] - \frac{m_s q_p}{e B_0 r_p} \left[R v_{G\parallel} - R_0 v_{G\parallel}^- \right] \quad (20)$$

where $\psi(r) = -B_0 \int_0^r r'/q dr'$. The last term $v_{G\parallel}^-$ in (20) is defined as,

$$v_{G\parallel}^- = \text{sign}(v_{G\parallel}) \sqrt{2/m_s} \sqrt{E - \mu B_{\max}} \mathcal{H}(E - \mu B_{\max})$$

with \mathcal{H} the Heaviside function and B_{\max} the maximum of the magnetic field on the whole simulation box. It has been chosen to minimize parallel flows. With this expression the difference between \bar{r} and r is of order ρ_* , the ratio of ρ_s the Larmor radius of species s and the minor radius a . In the case of a decaying turbulence it is important to choose $\bar{F}_{s,eq}$ as a function of the motion invariants, especially for studying zonal flows. It had been observed in [15,62] that breaking this rule leads to the development of large scale steady flows, which can prevent the onset of turbulence. This phenomena has also been observed in GYSELA simulations where a study of the difference between both equilibrium initialization has been performed in detail [33,63]. In [63] it has also been shown that when the system is driven by an external source of free energy, the choice of a canonical equilibrium is less crucial. The turbulence onset is only delayed and its ultimate nature is unaltered; namely characterized by the same level of parallel and axisymmetric flows, the same level of transport and the same correlation times and lengths.

2.7. Simplified collision operator recovering neoclassical effects

Although fusion plasmas are weakly collisional, so that a kinetic approach is mandatory, the effect of collisions cannot be fully neglected. Collisional transport plays an important role in regions where turbulent transport is low, such as transport barriers. Even more importantly, collisional friction damps low frequency flows, and hence controls the equilibrium radial electric field. Collisions also regularize fine structures in velocity space. Finally, collisions have also an impact on microinstabilities, *e.g.* via particle detrapping that is partially stabilizing Trapped Electron Modes (TEMs). In tokamak configurations, collisions depend on Coulomb binary interactions between particles (see Landau [64] for calculations). Then it is shown in [65] that the collision operator applied to the distribution functions can take the classical Fokker–Planck operator form:

$$\mathcal{C}_{ss'}(F_s, F_{s'}) = \frac{\partial}{\partial \mathbf{v}} \cdot \left\{ \left(\mathcal{D}(F_{s'}) \cdot \frac{\partial}{\partial \mathbf{v}} + \mathcal{V}(F_{s'}) \right) F_s \right\} \quad (21)$$

where \mathcal{V} is a dynamical friction term and \mathcal{D} is a diffusion term of the order of $\mathcal{D} \sim v_{T_s}^2 \nu_{ss'}$ with the collision frequency $\nu_{ss'}$ being defined as

$$\nu_{ss'} \sim \frac{\mathcal{D}}{v_{T_s}^2} \sim \frac{n_{s'}}{m_s} \left(\frac{1}{m_s} + \frac{1}{m_{s'}} \right) \frac{q_s^2 q_{s'}^2 \log \Lambda}{(1 + \epsilon_0)^2} \left(v_{T_s}^2 + v_{T_{s'}}^2 \right)^{-3/2} \quad (22)$$

where $n_{s'}$ is the density of species s' , q_s (resp. $q_{s'}$) is the particle charge of species s (resp. s'), m_s is the particle mass of species s , ϵ_0 the permittivity of free space, $\log \Lambda \approx 17$ the Coulomb logarithm and $v_{T_s} = \sqrt{T_s/m_s}$ is the thermal velocity of species s . Let us first underline that the frequency $\nu_{ss'}$ is different from $\nu_{s's}$. Besides, let us compare the collision frequencies for the different following particle populations: (i) ion–ion collisions: $\nu_{ii} \propto Z^4 n_i / \sqrt{m_i T_i}^{3/2}$, (ii) electron–electron collisions: $\nu_{ee} \propto n_e / \sqrt{m_e T_e}^{3/2}$, (iii) electron–ion collisions: $\nu_{ei} \approx Z \nu_{ee}$ and (iv) ion–electron collisions: $\nu_{ie} \approx \frac{m_e}{m_i} Z^2 \nu_{ee} \ll \nu_{ii} \ll \nu_{ee}$. Therefore, the ion–electron collisions can be neglected. At the moment in the code, the electrons are considered adiabatic, therefore only the ion–ion collisions and impurity–ion

collisions (see Section 2.8.1) are taken into account. The full gyro-averaged and linearized Landau operator has been derived in [66] but such a full Coulomb collisional operator is difficult to implement in GYSELA without severe loss of parallelization efficiency. As described in Section 3.2, the GYSELA parallelization takes advantage of the fact that the magnetic moment μ is an adiabatic invariant, that plays the role of a parameter in Boltzmann equation. A unique value of μ is assigned to each processor. It was shown that the predictions of the neoclassical theory at low collisionality could be entirely recovered with a reduced collision operator acting in the v_{\parallel} direction only [51]. In short, this results from the fact that the main ions of tokamak plasmas are weakly collisional. In this so-called banana regime, collisions essentially perturb the banana orbits at their turning points, where the parallel velocity of trapped particles vanishes. This corresponds to the trapped-passing boundary in the $(v_{\parallel}, v_{\perp})$ plane. Accounting for diffusion in v_{\parallel} then reveals sufficient to model such a transport, governed by the broadening of the trapped-passing boundary due to collisions. It also has the advantage of keeping μ invariant, hence not degrading the efficiency of the code parallelization. The operator implemented in the code is a simplified version of the Lenard–Bernstein operator [67]. This simplified version has been derived in [50] where it is especially shown that it recovers the exact neoclassical transport in the banana and plateau regimes⁴ (see Helander's book [68] p. 149 for complete neoclassical transport regime description). This generic energy and momentum-conserving collision operator has been implemented and successfully tested in the code (see [34], [51]). A new version also valid for the Pfirsch–Schlüter regime is under development. The current collision operator is expressed as a simplified Lorentz-type operator where only the $v_{G\parallel}$ contribution is taken into account:

$$\mathcal{C}_s(\bar{F}_s) = \frac{1}{B_{\parallel s}^*} \frac{\partial}{\partial v_{G\parallel}} \left\{ B_{\parallel s}^* \mathcal{D}_{\parallel s} \bar{F}_{M_s} \frac{\partial}{\partial v_{G\parallel}} \left(\frac{\bar{F}_s}{\bar{F}_{M_s}} \right) \right\} \quad (23)$$

where \bar{F}_{M_s} is a shifted Maxwellian distribution – chosen such that $\mathcal{C}_s(\bar{F}_{M_s}) = 0$ – defined as:

$$\bar{F}_{M_s} = \frac{n_{s0}}{(2\pi T_{s,\text{coll}}/m_s)^{3/2}} \times \exp \left(-m_s \frac{(v_{G\parallel} - V_{\parallel s,\text{coll}})^2}{2T_{s,\text{coll}}} - \frac{\mu_s B}{T_{s,\text{coll}}} \right). \quad (24)$$

The collision term $\mathcal{D}_{\parallel s}$ reads for each μ_s :

$$\mathcal{D}_{\parallel s}(r, v) = \mathcal{A}_s(r) \left(\frac{\Phi(v) - G(v)}{2v} \right) \quad (25)$$

with $\mathcal{A}_s(r) = 3 \frac{\sqrt{\pi}}{2} \frac{v_{T_s,\text{coll}}^3 \epsilon^{3/2}}{qR_0} \nu_{*s}$

where $\nu(r, v_{G\parallel}) = \sqrt{E/T_{s,\text{coll}}}$. The scalar ν_{*s} , associated to the main s species, is a dimensionless ion–ion collisionality parameter depending on the ion–ion collision frequency ν_{ss} such that:

$$\nu_{*s} = \frac{qR_0}{v_{T_s,\text{coll}} \epsilon^{3/2}} \nu_{ss} \quad \text{with} \quad \nu_{ss} = \frac{4\sqrt{\pi}}{3} \frac{n_s e^4 \log \Lambda}{(4\pi \epsilon_0)^2 m_s^2 v_{T_s,\text{coll}}^3} \quad (26)$$

⁴ The physics of neoclassical transport depends on the collisionality ν_* . If the collisionality is low, $\nu_* < 1$, the particle orbits are completed by a typical thermal particle. In this so-called *banana* regime, trapped particles almost fully determine the transport coefficients. In the opposite limit, $\nu_* > \epsilon^{-3/2}$, the particle orbit is not fully completed because its motion is disturbed by collisions before. This high collisionality regime is called the *Pfirsch–Schlüter* regime or fluid regime. In between, the *plateau* regime is characterized by a weak dependence of the transport on the collisionality of the plasma.

where $v_{T_s,\text{coll}}$ denotes the initial thermal velocity $v_{T_s,\text{coll}} = (T_{s,\text{coll}}/m_s)^{1/2}$, q the safety factor, $R = R_0 + r \cos \theta$ the major radius, $\epsilon = r/R_0$ the inverse aspect ratio and n_s the density of ion species s . The explicit expression (25) also involves the error function Φ and the Chandrasekhar function G defined as

$$G(v) = \frac{\Phi(v) - v\Phi'(v)}{2v^2} \quad \text{with} \quad \Phi(v) = \frac{2}{\sqrt{\pi}} \int_0^v e^{-x^2} dx$$

and $\Phi'(v) = \frac{2}{\sqrt{\pi}} e^{-v^2}$. (27)

Considering that the ν_{*s} scalar which is given (as input data) in the code corresponds to the main species, the collision frequencies $\nu_{s's'}$ for minority species s' are deduced from this value as

$$\nu_{s's'} = \frac{v_{T_{s'},\text{coll}} \epsilon^{3/2}}{qR_0} \nu_{*s'}$$

with $\nu_{*s'} = \left(\frac{n_{s'}}{n_s} \right) \left(\frac{Z_{s'}}{Z_s} \right)^4 \left(\frac{T_{s,\text{coll}}}{T_{s',\text{coll}}} \right)^2 \nu_{*s}$. (28)

Let us express for each μ_s , the operator $\mathcal{V}_{\parallel s}$ as

$$\mathcal{V}_{\parallel s}(r, v) = - \frac{(v_{G\parallel} - V_{\parallel s,\text{coll}})}{v_{T_s,\text{coll}}^2} \mathcal{D}_{\parallel s}(r, v)$$

with $v_{T_s,\text{coll}} = \sqrt{T_{s,\text{coll}}/m_s}$ (29)

then the collision operator (23) can be expressed with a more classical Fokker–Planck structure as:

$$\mathcal{C}_s(\bar{F}_s) = \frac{1}{B_{\parallel s}^*} \frac{\partial}{\partial v_{G\parallel}} \left[B_{\parallel s}^* \left(\mathcal{D}_{\parallel s} \frac{\partial \bar{F}_s}{\partial v_{G\parallel}} - \mathcal{V}_{\parallel s} \bar{F}_s \right) \right] \quad (30)$$

where the operators $\mathcal{D}_{\parallel s}$ and $\mathcal{V}_{\parallel s}$ respectively model a diffusion and a drag in the parallel velocity direction. The conservation properties of parallel momentum and energy are ensured by constraining $\mathcal{D}_{\parallel s}$ to depend on μ_s only and defining the local fluid velocity $V_{\parallel s,\text{coll}}$ and ion temperature $T_{s,\text{coll}}$ as follows

$$V_{\parallel s,\text{coll}} = P^{-1} \left[\left\langle \frac{m_s}{B_{\parallel s}^*} \partial_{v_{G\parallel}} (B_{\parallel s}^* \mathcal{D}_{\parallel s} v_{G\parallel}) \right\rangle \langle m_s \mathcal{D}_{\parallel s} v_{G\parallel} \rangle - \left\langle \frac{1}{B_{\parallel s}^*} \partial_{v_{G\parallel}} (B_{\parallel s}^* \mathcal{D}_{\parallel s}) \right\rangle \langle m_s^2 \mathcal{D}_{\parallel s} v_{G\parallel}^2 \rangle \right] \quad (31)$$

$$T_{s,\text{coll}} = P^{-1} \left[\langle m_s \mathcal{D}_{\parallel s} \rangle \langle m_s^2 \mathcal{D}_{\parallel s} v_{G\parallel}^2 \rangle - \langle m_s \mathcal{D}_{\parallel s} v_{G\parallel} \rangle \langle m_s^2 \mathcal{D}_{\parallel s} v_{G\parallel} \rangle \right] \quad (32)$$

where

$$P = \langle m_s \mathcal{D}_{\parallel s} \rangle \left\langle \frac{m_s}{B_{\parallel s}^*} \partial_{v_{G\parallel}} (B_{\parallel s}^* \mathcal{D}_{\parallel s} v_{G\parallel}) \right\rangle - \langle m_s^2 \mathcal{D}_{\parallel s} v_{G\parallel} \rangle \left\langle \frac{1}{B_{\parallel s}^*} \partial_{v_{G\parallel}} (B_{\parallel s}^* \mathcal{D}_{\parallel s}) \right\rangle \quad (33)$$

with the brackets $\langle \cdot \rangle$ corresponding to the velocity space integral $\langle \cdot \rangle = \int \cdot v_{\parallel} d\mu_s dv_{G\parallel} F_s$. The impact of the collisions on the evolution of the distribution function \bar{F}_s is taken into account by stepping the evolution of the distribution function $\partial_t \bar{F}_s = \mathcal{C}_s(\bar{F}_s)$ with a Crank–Nicolson scheme. This collision operator forces the system to relax towards the Maxwellian distribution function, calculated from the instantaneous and local parallel flow $V_{\parallel s,\text{coll}}$ and the isotropic temperature $T_{s,\text{coll}} \sim T_{s,\text{coll} \parallel}$.

2.8. Collisional transfer between two species

The inter-species operator currently implemented in the code is highly simplified. It only ensures the moment transfers and energy transfers between species. A more complete version, satisfying neoclassical results for impurity transport, is under development.

2.8.1. Collisional energy transfer

The energy exchange between two species is approached by the following reduced collision operator

$$\frac{d\bar{F}_s}{dt} = -\frac{\eta_{ss'}^{\mathcal{E}}}{(2\pi T_{\text{mean}}/m_s)^{3/2} T_{\text{mean}}} \left(\frac{\mathcal{E}_{ss'}}{T_{\text{mean}}} - \frac{3}{2} \right) \times \exp\left(-\frac{\mathcal{E}_{ss'}}{T_{\text{mean}}}\right) \equiv C_{ss'}^{\mathcal{E}}(\mathcal{E}_{ss'}) \quad (34)$$

$$\frac{d\bar{F}_{s'}}{dt} = -\frac{\eta_{s's}^{\mathcal{E}}}{(2\pi T_{\text{mean}}/m_{s'})^{3/2} T_{\text{mean}}} \left(\frac{\mathcal{E}_{s's}}{T_{\text{mean}}} - \frac{3}{2} \right) \times \exp\left(-\frac{\mathcal{E}_{s's}}{T_{\text{mean}}}\right) \equiv C_{s's}^{\mathcal{E}}(\mathcal{E}_{s's}) \quad (35)$$

where d/dt stands for the phase space Lagrangian derivative and the following definitions have been adopted

$$T_{\text{mean}} = \frac{T_s + T_{s'}}{2}; \quad \Delta T_{ss'} = T_s - T_{s'} = -\Delta T_{s's} \quad (36)$$

$$V_{\text{mean}} = \frac{V_{\parallel s} + V_{\parallel s'}}{2}; \quad \Delta V_{ss'} = V_{\parallel s} - V_{\parallel s'} \quad (37)$$

$$\mathcal{E}_{ss'} = \frac{m_s (v_{G\parallel} - V_{\text{mean}})^2}{2} + \mu_s B; \quad (38)$$

$$\mathcal{E}_{s's} = \frac{m_{s'} (v_{G\parallel} - V_{\text{mean}})^2}{2} + \mu_{s'} B.$$

The temperatures and fluid velocities which enter these definitions are flux surface averaged, *i.e.* by considering $\langle \cdot \rangle_{\text{FS}} = \int \cdot J_x d\theta d\varphi / \int J_x d\theta d\varphi$. Then velocities correspond to $V_{\parallel s}(r) = \langle \int v_{G\parallel} \bar{F}_s d^3\mathbf{v} \rangle_{\text{FS}} / N_s(r)$ with density $N_s(r) = \langle \int \bar{F}_s d^3\mathbf{v} \rangle_{\text{FS}}$, the volume element being defined as $d^3\mathbf{v} = J_v dv_{G\parallel} d\mu_s$. Temperatures are defined as $T_s(r) = 2/3 \langle \int \mathcal{E}_s \bar{F}_s d^3\mathbf{v} \rangle_{\text{FS}} / N_s(r)$ where $\mathcal{E}_s = (m_s/2) (v_{G\parallel} - V_{\parallel s})^2 + \mu_s B$. The parameter $\eta_{ss'}^{\mathcal{E}}$ has been designed so that particles and parallel momentum are conserved

$$\eta_{ss'}^{\mathcal{E}} = \frac{8 \varepsilon^{3/2} m_s}{3\sqrt{\pi} m_{s'}} \left(\frac{Z_{s'}}{Z_s} \right)^2 \frac{n_{s'} \sqrt{T_{s,\text{coll}}/m_s}}{qR_0} \left(1 + \frac{v_{T_s}^2}{v_{T_s'}}^2 \right)^{-3/2} v_{*s} \quad (39)$$

where the normalized ion–ion collision frequency v_{*s} is given by Eq. (26) (for detailed calculation see Appendix B.1). Numerically, Eq. (34), is solved as $\bar{F}_s(t + \Delta t) = \bar{F}_s(t) + \Delta t C_{ss'}^{\mathcal{E}}(\mathcal{E}_{ss'}, t)$.

2.8.2. Parallel momentum transfer

Parallel momentum exchange between two species can be modeled by the following approximate collision operator:

$$\frac{d\bar{F}_s}{dt} = -\eta_{ss'}^{v_{G\parallel}} \Delta V_{ss'} v_{G\parallel} \exp\left(-\frac{E_s}{T_{\text{mean}}}\right) \equiv C_{ss'}^{v_{G\parallel}}(E_s) \quad (40)$$

with $E_s = \frac{1}{2} m_s v_{G\parallel}^2 + \mu_s B$

$$\frac{d\bar{F}_{s'}}{dt} = -\eta_{s's}^{v_{G\parallel}} \Delta V_{s's} v_{G\parallel} \exp\left(-\frac{E_{s'}}{T_{\text{mean}}}\right) \equiv C_{s's}^{v_{G\parallel}}(E_{s'}) \quad (41)$$

where T_{mean} is defined by Eq. (36). $\Delta V_{ss'}$ is equivalent to Eq. (37). The parameters $\eta_{ss'}^{v_{G\parallel}}$ and $\eta_{s's}^{v_{G\parallel}}$ are designed such that only parallel momentum exchanges are induced by this operator, thus leading to

$$\eta_{ss'}^{v_{G\parallel}} = n_{s'} m_s^2 \left(\frac{\varepsilon}{2\pi} \right)^{3/2} \frac{1}{qR_0} \frac{\sqrt{T_{s,\text{coll}}}}{T_{\text{mean}}^{5/2}} \left(\frac{Z_{s'}}{Z_s} \right)^2 \frac{v_{T_s}}{v_{T_s'}} v_{*s} \quad \text{and} \quad (42)$$

$$\eta_{s's}^{v_{G\parallel}} = \left(\frac{m_{s'}}{m_s} \right)^{3/2} \eta_{ss'}^{v_{G\parallel}}$$

where the velocity v_{T_s} corresponds to the maximum value between v_{T_s} and $v_{T_s'}$ (for more details see Appendix B.2).

2.9. Flux-driven code with source terms

2.9.1. Sources of heating, momentum and vorticity

As introduced previously GYSELA is a *full-f* code, namely the back reaction of turbulent transport is accounted for in the time evolution of the equilibrium. In such a framework, the turbulence regime is evanescent if no free energy is injected in the system. Turbulent transport results in the flattening of the temperature profile, which would ultimately reach marginal stability in the absence of any forcing. A heat source is mandatory in view of exploring the long time – on energy confinement times – behavior of turbulence and transport. In GYSELA, the possibility to drive the system by a prescribed source was added in 2009 [48]. This source consists of the sum of the product of Hermite and Laguerre polynomials in $v_{G\parallel}$ and μ_s , respectively, in the spirit of the pioneering work by Darmet et al. [69]. It is versatile enough to allow for separate injection of heat, parallel momentum and vorticity. Such a versatility imposes serious constraints on the expression of the source in phase space. The separation between these three kinds of sources is achieved using projections onto the bases of orthogonal Hermite polynomials in $v_{G\parallel}$ and orthogonal Laguerre polynomials in μ_s . The retained expression for the source is the following

$$\frac{d\bar{F}_s}{dt} = S_{\text{heat}}(r, \theta, v_{G\parallel}, \mu_s) + S_{\text{moment}}(r, \theta, v_{G\parallel}, \mu_s) + S_{\text{vorticity}}(r, \theta, v_{G\parallel}, \mu_s) \quad (43)$$

where the pure heating source is defined as:

$$S_{\text{heat}} = \left[\bar{v}_{G\parallel s}^2 - \frac{1}{2} - \frac{J_{\parallel B}}{2 - J_{\parallel B}} (2 - \bar{\mu}_s) (2\bar{v}_{G\parallel s} - J_{\parallel B}) \right] \times \frac{2S_0^{\mathcal{E}}}{(2\pi T_{s,\text{srce}}/m_s)^{3/2} T_{s,\text{srce}}} S_r^{\mathcal{E}} e^{-\bar{v}_{G\parallel s}^2 - \bar{\mu}_s} \quad (44)$$

with $\bar{\mu}_s = \mu_s B / T_{s,\text{srce}}$, $\bar{v}_{G\parallel s} = v_{G\parallel} / \sqrt{2T_{s,\text{srce}}/m_s}$, $J_{\parallel B} \equiv \sqrt{2m_s T_{s,\text{srce}} / (q_s B^2)} \mu_{0\parallel}$ and $\alpha = (m_s/q_s^2) \times T_{s,\text{srce}} / (2B^2)$. S_{moment} is a pure momentum source expressed as

$$S_{\text{moment}} = [2\bar{v}_{G\parallel s} (2 - \bar{\mu}_s) - J_{\parallel B} (1 + 2\bar{v}_{G\parallel s} - \bar{\mu}_s)] \times \frac{S_0^{v_{G\parallel}}}{4\pi^{3/2} (T_{s,\text{srce}}/m_s)^2} S_r^{v_{G\parallel}} e^{-\bar{v}_{G\parallel s}^2 - \bar{\mu}_s} \quad (45)$$

while $S_{\text{vorticity}}$ is a pure source of vorticity

$$S_{\text{vorticity}} = -[2\bar{v}_{G\parallel s}^2 - \bar{\mu}_s] \frac{S_0^{\Omega}}{\alpha (2\pi T_{s,\text{srce}}/m_s)^{3/2}} S_r^{\Omega} e^{-\bar{v}_{G\parallel s}^2 - \bar{\mu}_s}. \quad (46)$$

The prescribed radial envelopes $S_r^{\mathcal{E}}$, $S_r^{v_{G\parallel}}$ and S_r^{Ω} are chosen as the sum of two hyperbolic tangents but could be any radial function under the constraint that the integral over the minor radius is normalized to 1 while $S_0^{\mathcal{E}}$, $S_0^{v_{G\parallel}}$ and S_0^{Ω} correspond to the source amplitudes and $T_{s,\text{srce}}$ to the temperature of the source. They are usually localized close to the inner boundary of the simulation domain [48]. The heat source is an isotropic source that takes particles at a vanishing velocity and accelerates them up to $v \approx 1.5v_{T_h}$. There are two main advantages in dealing with a prescribed heat source: (i) the forcing of turbulence can mimic that in experiments, in contrast to simulations where the mean gradient is prescribed and (ii) the sum of the spatially and time (on the τ_E time scale) averaged turbulent and neoclassical heat fluxes must balance the prescribed driving flux. In this case, the response is the temperature gradient, which ultimately governs the internal energy and therefore the performance of the discharge. An example of initial and final temperature profiles is shown in Fig. 1. Flux driven simulations then allow investigating the impact of heating power on

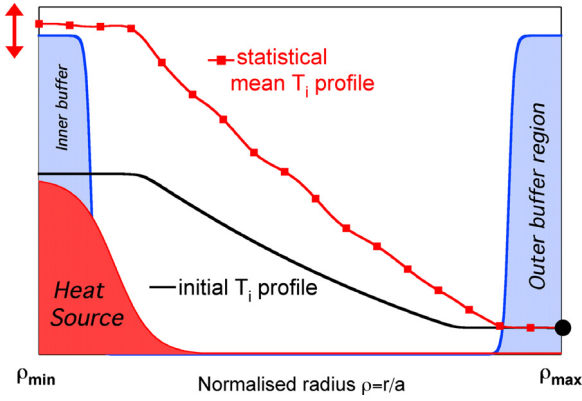


Fig. 1. Schematic view of a heat source and buffer regions in the case of a flux driven simulation. Comparison between initial temperature profile (black line) and final temperature (red line). (For interpretation of the references to colour in this figure legend, the reader is referred to the web version of this article.)

the energy confinement time [53]. The source of vorticity described before has been efficiently used to polarize the plasma [54] inducing the development of sheared electric fields in the turbulent core. The creation of ion transport barriers by these externally induced sheared $E \times B$ flows has been studied in detail in [55,54].

2.9.2. Energetic particle source

A source of energetic particles (EPs) has been also implemented in the code to study the interaction between EPs and turbulence. EPs are characterized by energies larger than the thermal energy. The excitation by EPs of the geodesic acoustic modes (GAMs) – corresponding to the oscillatory component of large scale $E \times B$ zonal flows – creates modes which are called energetic geodesic acoustic modes (EGAMs) [70,71]. For more details on the impact of EGAMs on turbulence see [72–74]. In practice this source is coupled to the heating source, such that $d_t \bar{F}_s = S_{\text{heat}} + S_{\text{EP}}$ where S_{EP} is also built, as for the previous sources, by using projection onto the Laguerre and Hermite polynomial bases, with the constraint to inject only parallel energy. For symmetry reason, the energetic particle source, is built as

$$S_{\text{EP}}(r, \theta, v_{G\parallel}, \mu_s, t) = S_0^{\text{EP}}(t) S_r^{\text{EP}}(r) (S_+ + S_-)$$

$$\text{with } S_-(\theta, v_{G\parallel}, \mu_s) = S_+(\theta, -v_{G\parallel}, \mu_s)$$

where S_0^{EP} is the source amplitude and S_r^{EP} the radial profile is normalized such that $\int r dr S_r^{\text{EP}} = 1$. After the same kind of calculation as in the previous sources, the final expression reads

$$S_{\pm} = \left[(\bar{v}_{G\parallel s} \pm \bar{v}_0)^2 - \frac{1}{2} - \mathcal{Q}_{\text{EP}}(2 - \bar{\mu}_s)(2(\bar{v}_{G\parallel s} \pm \bar{v}_0) - J_{\parallel B}) \right] \times e^{-(\bar{v}_{G\parallel s} \pm \bar{v}_0)^2} e^{-\bar{\mu}_s} \quad (47)$$

where $\bar{\mu}_s = \mu_s B(r, \theta) / T_{s\perp}$ and $\mathcal{Q}_{\text{EP}} = J_{\parallel B} / (2 - J_{\parallel B}^2(1 + 2\bar{v}_0^2))$ with $\bar{v}_0 = v_0 / \sqrt{2T_{s\parallel}}$ an arbitrary normalized velocity. The expressions of the parallel current $J_{\parallel B}$ and the velocity $\bar{v}_{G\parallel s}$ are the same as in Eq. (44) where $T_{s,\text{srce}}$ is replaced by $T_{s\parallel}$. $T_{s\parallel}$ and $T_{s\perp}$ correspond to the normalized parallel and perpendicular temperatures of the energetic particle source. Each of the terms S_+ and S_- does not inject neither mass – which is essential because electrons are considered adiabatic in the code – nor vorticity. The source mimics the effects of two tangential neutral beam injectors, oriented in the co- and counter-current directions. It is localized around the mid position $r = 0.5 (r_{\min} + r_{\max})$ and brings the distribution function out of the equilibrium by creating a positive slope in energy. As explained in [73] v_0 and $T_{s\parallel}$ are both critical parameters in view of exciting EGAMs. GYSELA results for EGAMs excitation have been successfully compared to analytical theory [73] and benchmarked [75] more recently with ORB5 code.

2.9.3. Source of impurities

Finally, it is also possible to add a source of impurities s' of the form

$$S_{n_{s'}} = \frac{S_0^{n_{s'}} S_r}{\left(\frac{2\pi T_{s',\text{srce}}}{m_{s'}} \right)^{3/2}} \left(\frac{5}{2} - \frac{\mu_{s'} B}{T_{s',\text{srce}}} - \frac{m_{s'} v_{G\parallel}^2}{2T_{s',\text{srce}}} \right) \times \exp \left(-\frac{m_{s'} v_{G\parallel}^2}{2T_{s',\text{srce}}} - \frac{\mu_{s'} B}{T_{s',\text{srce}}} \right). \quad (48)$$

Let us notice that this source of matter is not a pure source, due to the fact that it also injects some amount of vorticity. This injection is balanced by a sink for the major species s , such that

$$Z_s \int S_{n_s} J_{v_s} dv_{G\parallel} d\mu_s + Z_{s'} \int J_{v_{s'}} S_{n_{s'}} dv_{G\parallel} d\mu_{s'} = 0.$$

2.10. Diffusion terms in the buffer regions

Finally, to avoid strong gradients at the boundaries, radial diffusion and artificial damping can be added in buffer regions. These buffer regions are defined at each side of the radial domain $r \in [r_{\min}, r_{\max}]$ as a sum of hyperbolic tangents:

$$H_{\text{buff}}(r) = 1 + \frac{1}{2} \left[\tanh \left(\frac{r - r_{\max} + B_L L_r}{B_S L_r} \right) - \tanh \left(\frac{r - r_{\min} - B_L L_r}{B_S L_r} \right) \right] \quad (49)$$

where L_r is the length of the radial domain. B_L and B_S are respectively the location and the stiffness of the buffer regions. The function H_{buff} plays the role of a mask which is equal to 1 in the buffer regions and 0 elsewhere. The diffusion term which is applied in the buffer regions is of the form

$$\mathcal{D}_r(\bar{F}_s) = \frac{1}{B_{\parallel s}^*} \left[\frac{1}{r} \frac{\partial}{\partial r} \left(r \chi(r) B_{\parallel s}^* \frac{\partial}{\partial r} \bar{F}_s \right) \right] \quad (50)$$

with $\chi(r) = \chi_0 H_{\text{buff}}(r)$ (χ_0 being the diffusion coefficient). The equation $\partial_t \bar{F}_s = \mathcal{D}_r(\bar{F}_s)$ is solved by using a Crank–Nicolson scheme. An artificial damping term ν_0 is introduced in the buffer regions by defining a Krook operator $\mathcal{K}_r(\bar{F}_s) = -\nu(r)(\bar{F}_s - \bar{F}_{s,\text{eq}})$ with $\nu(r) = \nu_0 H_{\text{buff}}(r)$ and solving $\partial_t \bar{F}_s = \mathcal{K}_r(\bar{F}_s)$. Let Δt be the time step, then an analytic solution of the previous equation is given by $\bar{F}_s(t + \Delta t) = \bar{F}_{s,\text{eq}} + (\bar{F}_s(t) - \bar{F}_{s,\text{eq}}) \exp(-\nu(r)\Delta t)$. This mechanism restores the distribution function to its initial equilibrium state $\bar{F}_{s,\text{eq}}$, in the buffer regions, by slowly damping all the turbulent modes of the system. It also plays the role of a heat sink by effectively coupling the plasma with the outer thermal baths.

3. A highly parallel semi-Lagrangian code

Solving the set of gyrokinetic equations (5)–(12) is very challenging. It consists of (i) one evolution equation (5) of the distribution function for each ion species (so far, we are limited to 3 distribution functions in GYSELA. Considering that kinetic electrons will soon become operational, this leaves 2 slots for ions: either Deuterium and Tritium, or a main ion species plus any kind of impurity, either intrinsic like Helium or extrinsic, such as Tungsten for instance) in the 4D phase space parametrized by the adiabatic invariant μ ; (ii) the set of four coupled ordinary differential equations (ODE) for the trajectories (6)–(7); and (iii) 3D integro-differential equations for the field, namely the quasi-neutrality equation (12). This set of equations is nonlinear, the dominant quadratic nonlinearity being due to the $\mathbf{E} \times \mathbf{B}$ advection

term. The quasi-neutrality equation is generally solved in most of the gyrokinetic codes by using Fourier projection in all the periodic directions and finite differences or finite elements in the others. Concerning the global algorithm, the challenge consists in finding numerical schemes which preserve the first principles such as the conservation of Casimir invariants, the phase space volume and the total energy. Various numerical schemes, classifiable as PIC, Eulerian or semi-Lagrangian, have been explored until now. In the following, we focus on the semi-Lagrangian approach which is specific of the GYSELA code.

3.1. Specificity of the GYSELA code: the semi-Lagrangian scheme

Semi-Lagrangian (SL) schemes have been first used for the advection of vorticity in simplified models of large scale flows. It has gained maturity when the discretization approach was introduced in the relevant context of atmospheric flows. A comprehensive review of semi-Lagrangian methods in this meteorological context until 1990 is due to Staniforth [76]. It is also applied to geophysical fluid dynamics (cf. [77]). In magnetized plasma turbulence area, the SL method has been first applied to calculate a turbulence driven by passing ions in 2D (1D in space, 1D in velocity) [78] and trapped ions in 3D (2D in space, 1D in velocity) [79,58]. This method was then extended to the 4D model (3D in space and v_{\parallel} (with $\mu = 0$)) of Ion Temperature Gradient (ITG) driven turbulence in cylindrical geometry with the development of the GYSELA code (for Gyrokinetic SEmi-LAgrangian code) [32] and the CYGNE code [80]. The 4D drift-kinetic slab-ITG version of the GYSELA code has shown good properties of energy conservation in non-linear regime [32] as well as accurate description of fine spatial scales [81]. In the CYGNE code the standard Taylor expansion is replaced by a Bürlisch–Stoer scheme (for the 2D advection) to increase the spatial accuracy and the logarithmic interpolation technique is used to ensure the positivity of the distribution function. Brunetti et al. [80] have shown that (i) the positivity can be preserved but at the cost of larger diffusion and (ii) that non-equidistant meshes in radial and parallel velocity directions are a key tool for obtaining accurate results. Due to the good conservation property obtained in 4D, the gyrokinetic 5D version of the GYSELA code [46] has been based on the same numerical scheme. The global algorithm for the new 5D gyrokinetic multi-ion species version of the code will be described in the following both in terms of numerics (Section 3.1.3) and parallelization (Section 3.2). Advantages and drawbacks of such a 5D semi-Lagrangian code will be discussed. The purpose of the semi-Lagrangian method is to take advantage of both the Lagrangian and Eulerian approaches, with an accurate description of the phase space, in particular regions where the density is low, as well as an enhanced numerical stability. It is based on the fact that the most precise way to solve convection (or advection) hyperbolic PDE is to use their characteristics along which the distribution function remains constant. This method was primarily developed by Cheng and Knorr [82]. It has been cast in more general framework of SL by Sonnendrücker in 1998 [78] and Nakamura in 1999 [83]. In this approach, the phase-space mesh grid is kept fixed in time (Eulerian method) and the Vlasov equation is integrated along the trajectories (Lagrangian method) using the invariance of the distribution function along the trajectories. The GYSELA code is based on this standard semi-Lagrangian approach [78]. This approach has been recently renamed *Backward semi-Lagrangian approach (BSL)* by its author to make the distinction with the emergence of new schemes: (i) *Forward semi-Lagrangian approach (FSL)* firstly proposed in 2009 [84] and (ii) *Conservative semi-Lagrangian approach (CSL)* proposed in [85,86] through Parabolic Spline Method [87]. The main difference between BSL and FSL approaches is that the advection equations are solved backward in time in the first case

and forward in the second one. They are both based on solving the advective form of Vlasov equation while the CSL methods deal with the conservative form of the Vlasov equation. FSL and CSL schemes have both been tested in GYSELA [88,89] but the actual version of the code is the standard BSL approach as described in the following.

3.1.1. Backward semi-Lagrangian (BSL) concept

Let us consider the 5D gyrokinetic Vlasov equation

$$B_{\parallel s}^* \frac{\partial \bar{F}_s}{\partial t} + \nabla \cdot \left(B_{\parallel s}^* \frac{d\mathbf{x}_G}{dt} \bar{F}_s \right) + \frac{\partial}{\partial v_{G\parallel}} \left(B_{\parallel s}^* \frac{dv_{G\parallel}}{dt} \bar{F}_s \right) = 0 \quad (51)$$

which corresponds to Eq. (5) without collisions and source terms. By using the incompressibility property of the gyrocenter flow in the 4D phase space, i.e. $\nabla \cdot (B_{\parallel s}^* d_t \mathbf{x}_G) + \partial_{v_{G\parallel}} (B_{\parallel s}^* d_t v_{G\parallel}) = 0$, the previous conservative Vlasov equation (51) is equivalent to its advective form

$$\frac{\partial \bar{F}_s}{\partial t} + \frac{d\mathbf{x}_G}{dt} \cdot \nabla \cdot \bar{F}_s + \frac{dv_{G\parallel}}{dt} \frac{\partial \bar{F}_s}{\partial v_{G\parallel}} = 0. \quad (52)$$

Let $\Gamma = (\mathbf{x}_G, v_{G\parallel}, \mu_s)$ be a position vector in the phase space solution of the characteristic equations (6)–(7). Then Eq. (52) leads to $d_t \bar{F}_s(\Gamma(t), t) = 0$. The semi-Lagrangian method uses this invariance of the distribution function \bar{F}_s along its characteristics. Let us consider the computational 5D domain $[x_{G\min}^1, x_{G\max}^1] \times [x_{G\min}^2, x_{G\max}^2] \times [x_{G\min}^3, x_{G\max}^3] \times [v_{G\parallel\min}, v_{G\parallel\max}] \times [\mu_{s\min}, \mu_{s\max}]$ and the associated grid (fixed in time) defined by the finite set of mesh points $\Gamma_{ijklm} = (x_{G_i}^1, x_{G_j}^2, x_{G_k}^3, v_{G_{\parallel l}}, \mu_{s_m})$ with $x_{G_q}^p = q \Delta x_G^p$ for all $q = 0, \dots, N_p$ with $p = 1, 2, 3$; $v_{G_{\parallel l}} = l \Delta v_{G\parallel}$ for all $l = 0, N_{v_{\parallel}}$ and μ_{s_m} for all $m = 0, N_{\mu}$. N_1, N_2, N_3 are the number of cells in each spatial directions and $N_{v_{\parallel}}$ the number of cells in $v_{G\parallel}$ direction. The $(N_{\mu} + 1)$ values for μ_s are not necessary equidistributed. Actually, the standard choice in GYSELA corresponds to an equidistributed grid in $\sqrt{\mu}$. This choice leads to a better accuracy when computing integrals in μ . Let us also assume that \bar{F}_s is known at each point Γ_{ijklm} of this grid at time t_n . Therefore the distribution function can be computed at the next time $t_n + \Delta t$, with Δt the time step, on the same grid by using the invariance property $\bar{F}_s(\Gamma_{ijklm}(t_n + \Delta t), t_n + \Delta t) = \bar{F}_s(\Gamma(t_n, \Gamma_{ijklm}, t_n + \Delta t), t_n)$ where $\Gamma(t_n, \Gamma_{ijklm}, t_n + \Delta t)$ corresponds to the solution of the characteristic at time step t_n which is equal to Γ_{ijklm} at time $t_n + \Delta t$. The method consists in (i) finding the foot of the characteristic at the time t_n : $\Gamma(t_n, \Gamma_{ijklm}, t_n + \Delta t)$ by solving backward in time the advection equations (6)–(7) and (ii) computing $\bar{F}_s(\Gamma(t_n, \Gamma_{ijklm}, t_n + \Delta t), t_n)$ by interpolation, using the fact that at this time t_n the distribution function is known over the whole fixed grid. Cubic spline interpolations are used in the code, because it offers a good compromise between accuracy (small diffusivity) and simplicity (numerical cost) [90,91].

3.1.2. Time-splitting

In low-dimensional systems, the semi-Lagrangian method is very efficient. When applied to higher dimensional problems, one faces the problem of multidimensional interpolation, which is extremely expensive for high dimensional problems. However, this problem has been partially cured by using the time-splitting idea of Cheng and Knorr [82]. Using the incompressibility property, Strang's operator decomposition into space and velocity can be applied, replacing Eq. (5) by a set of two conservative equations. Besides, to avoid dealing with a 3D space operator, the latter is also divided into two parts. Let us denote $\mathcal{X}_G = (x_G^1, x_G^2) = (r, \theta)$ and remind that in our case $x_G^3 = \varphi$ then the Boltzmann equation (5) is solved by applying a splitting of Strang [92] as

$$B_{\parallel s}^* \frac{\partial \bar{F}_s}{\partial t} + \nabla \cdot \left(B_{\parallel s}^* \frac{d\mathcal{X}_G}{dt} \bar{F}_s \right) = 0 \quad \text{at } (\varphi, v_{G\parallel}) \text{ fixed} \quad (53)$$

$$B_{\parallel s}^* \frac{\partial \bar{F}_s}{\partial t} + \frac{\partial}{\partial \varphi} \left(B_{\parallel s}^* \frac{d\varphi}{dt} \bar{F}_s \right) = 0 \quad \text{at } (\mathcal{X}_G, v_{G\parallel}) \text{ fixed} \quad (54)$$

$$B_{\parallel s}^* \frac{\partial \bar{F}_s}{\partial t} + \frac{\partial}{\partial v_{G\parallel}} \left(B_{\parallel s}^* \frac{dv_{G\parallel}}{dt} \bar{F}_s \right) = 0 \quad \text{at } \mathbf{x}_G \text{ fixed.} \quad (55)$$

This splitting into three equations was introduced in the 4D version of the code. As explained in [32], in the 4D drift-kinetic slab case the conservative and advective forms of the equations are equivalent in the (r, θ) direction and z direction separately due to the independent vanishing divergence property, see equations (9)–(10) in [32] due to $\nabla \cdot v_{GC} = 0$ and $\partial_z v_{\parallel} = 0$. In the 5D gyrokinetic case $\nabla_{\perp} \cdot (B_{\parallel s}^* d_t \mathcal{X}_G) \neq 0$ and $\partial_{\varphi} (B_{\parallel s}^* d_t \varphi) \neq 0$ so that these terms should be taken into account as source terms of the advective form of Eqs. (53) and (54). However, they are presently set to zero. This simplification may alter the accuracy of the conservation properties of the code (see Section 5). Also, it likely has an impact on the maximal value acceptable for the discretization time step. A solution to overcome this problem could be to use a conservative scheme instead of the BSL one but the first tests we have performed [89] are not conclusive. This constraint on the numerical value of Δt is acceptable for ion turbulence simulations but could become problematic when addressing kinetic electrons. The development of more efficient semi-Lagrangian schemes is still an active axis of research. An idea currently under evaluation is to separate and to treat differently the linear and non-linear parts. Encouraging results have been presented in [93]. The splitting operation stays a drawback of the semi-Lagrangian method. An alternative method without splitting (based on a 4D advection and 4D cubic spline interpolation) is currently developed. The first drawback is an increase of the numerical diffusion due to the 4D interpolation which will require to be quantified.

In the current version, the advections in φ and $v_{G\parallel}$ directions are straightforward, but that in the \mathcal{X}_G direction requires more attention. If we consider the 2D advection in (r, θ) direction between times t and $t + \Delta t$, the value of the electric field \mathbf{E} at time $t + \Delta t/2$ is required in second order time scheme. This value is calculated by using a predictor–corrector method. Besides, computing these 2D trajectories is equivalent to solving $d\mathcal{X}_G/dt = \mathbf{V}(\mathcal{X}_G, \varphi, t)$, \mathbf{V} being the advection field. This system is solved by using the parabolic assumption developed in [78]. Let \mathcal{X}_{Gij} be the position of $\mathcal{X}_G(t_n + \Delta t)$ at time $t_n + \Delta t$, then there exists a displacement $\mathbf{d}_{ij} = (\alpha_{ij}, \beta_{ij})$ tangent to the parabola such that $\mathcal{X}_G(t_n) = \mathcal{X}_{Gij} - \mathbf{d}_{ij}$ and $\mathcal{X}_G(t_n - \Delta t) = \mathcal{X}_{Gij} - 2\mathbf{d}_{ij}$. The displacement \mathbf{d}_{ij} can be calculated by solving the implicit equation $\mathbf{d}_{ij} = \Delta t \mathbf{V}(\mathcal{X}_{Gij} - \mathbf{d}_{ij}, t_n)$ (see p. 129 in [37]). This is done with a Taylor expansion which is equivalent at second order to a Newton algorithm.

3.1.3. GYSELA global algorithm

Concerning now the complete Boltzmann equation (5) the right hand side is also split to treat separately the collision operator, the Krook operator, the diffusion and source terms. Let \mathcal{X}_G denote the shift operator in the poloidal cross-section (r, θ) associated to Eq. (53) over a time step Δt . Similarly, $\tilde{\varphi}$ and $\tilde{v}_{G\parallel}$ denote the shift operators respectively in the φ (Eq. (54)) and $v_{G\parallel}$ directions (Eq. (55)). As described in the previous paragraph, each of these three shift operators is based on a backward semi-Lagrangian scheme which means two steps for each mesh point: (i) first the computation of the characteristic feet and (ii) second an interpolation by cubic splines. Let us denote \tilde{C} the collision operator corresponding to solving $\partial_t \bar{F}_s = C(\bar{F}_s)$ and \tilde{D} the operator associated to the radial diffusion $\partial_r \bar{F}_s = \mathcal{D}_r(\bar{F}_s)$. They are both solved by applying a Crank–Nicolson scheme. The Krook operator $\tilde{\mathcal{K}}$ corresponding to the Krook diffusion equation $\partial_t \bar{F}_s = \mathcal{K}(\bar{F}_s)$ is trivial while solving $\partial_t \bar{F}_s = \mathcal{S}$ associated to the source operator \mathcal{S} is

described in Appendix C. Then, using these notations the following sequence is used to solve the 5D Boltzmann equation (5)

$$\widetilde{\text{Boltz}} \equiv \left[\left(\frac{\tilde{\mathcal{K}}_r}{2}, \frac{\tilde{\mathcal{D}}_r}{2}, \frac{\tilde{C}}{2}, \frac{\tilde{\mathcal{S}}}{2} \right), \left(\frac{\tilde{v}_{G\parallel}}{2}, \frac{\tilde{\varphi}}{2}, \tilde{\mathcal{X}}_G, \frac{\tilde{\varphi}}{2}, \frac{\tilde{v}_{G\parallel}}{2} \right), \left(\frac{\tilde{\mathcal{S}}}{2}, \frac{\tilde{C}}{2}, \frac{\tilde{\mathcal{D}}_r}{2}, \frac{\tilde{\mathcal{K}}_r}{2} \right) \right] \quad (56)$$

where the factor 1/2 means that the operator is applied on half a time step. The choice of the sequence (56) is not unique but some constraints are imposed in the code: (i) the first one is to impose a symmetry to keep second order accuracy in the splitting (Strang splitting [92]), (ii) the second one is to fix the 2D operator $\tilde{\mathcal{X}}_G$ which is the most costly at the middle of the algorithm; (iii) finally the operators coupled to the right hand side, respectively to the Vlasov equation, are contiguous. Let us also define the operator \tilde{Q} (corresponding to the Poisson solving) which denotes symbolically the four steps: (i) computation of right hand side of the quasi-neutrality equation (12) using expression (13), (ii) solving the QN equation (12) to deduce the electrostatic potential U , (iii) computation of the gyro-averaged electric potential $\bar{U} = \mathcal{J}_{\mu} \cdot U$ with a Padé approximation (18) or with an integration on the gyro-circles as described in Section 2.5 and (iv) computation of the electric field as $\mathbf{E} = -\nabla \bar{U}$.

Finally, the global numerical algorithm of the GYSELA code can be summarized (see schematic view in Fig. 2) as follows:

1. Initialization

Considering a prescribed magnetic field $B(r, \theta)$ (see Section 2.2) and equilibrium profiles of density $n_0(r)$, ion temperatures $T_s(r)$ and safety factor $q(r)$ (see Section 2.6), then

- Computation of the equilibrium distribution function $\bar{F}_{s,eq}$ as a local or canonical Maxwellian by using (19) and (20).
- Initialization of $\bar{F}_s(t = 0)$ as $\bar{F}_s(t = 0) = \bar{F}_{s,eq}(1 + \text{perturbation})$ as described in Section 2.6.

2. For each time iteration

Considering the distribution function $\bar{F}_s^n = \bar{F}_s(t = t_n)$ at time t_n known on the 5D mesh grid, then the distribution function \bar{F}_s^{n+1} at the next time $t_{n+1} = t_n + \Delta t$ on the same mesh grid is computed by using a predictor–algorithm as

- Computation of the electric field $\mathbf{E}(t_n)$ by using the \tilde{Q} sequence.
- Prediction on $\Delta t/2$:**
 - Computation of $\bar{F}_s(t = t_n + \Delta t/2)$ by solving $\widetilde{\text{Boltz}}/2$ sequence with $\mathbf{E}(t_n)$.
 - Computation of $\mathbf{E}(t_n + \Delta t/2)$ by solving \tilde{Q} .
- Correction on Δt :**
 - Starting from $\bar{F}_s(t = t_n)$ – given that this 5D distribution function has been stored before prediction – computation of $\bar{F}_s(t = t_n + \Delta t)$ by solving $\widetilde{\text{Boltz}}$ on a time step Δt with the electric field $\mathbf{E}(t_n + \Delta t/2)$ at time $t_{n+1/2}$.

3.2. An efficient hybrid OpenMP/MPI parallelization

The code is developed in Fortran 90 with some I/O routines in C (47k lines of Fortran 90 and 2.3k lines of C code) using GIT as version control system. Doxygen is used to generate documentation from the source code. The only external library dependence is the HDF5 library. HDF5 is the chosen format for all output saving, both 0D to 3D diagnostics and 5D restart files. Diagnostic analyses are performed with Python. The parallelization is based on a hybrid MPI/OpenMP paradigm. This hybrid approach is suitable for cluster of SMP (symmetric shared memory multi-processor) nodes where MPI provides communication capability

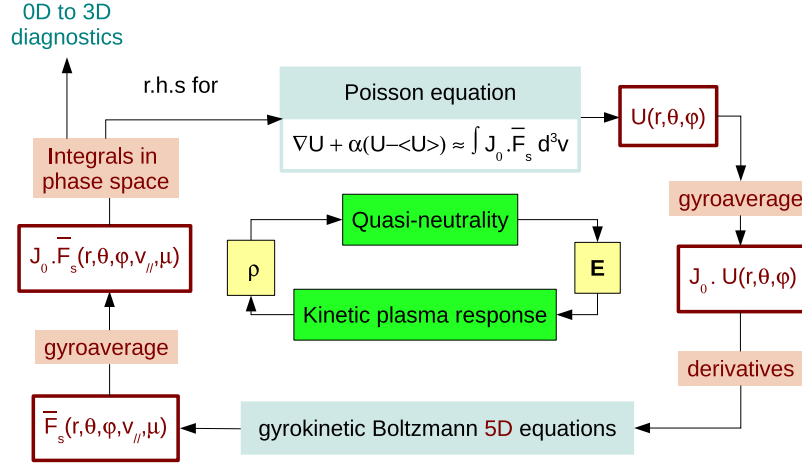


Fig. 2. Schematic view of the coupling between the Poisson and Vlasov solvers in the GYSELA code.

across nodes and OpenMP exploits loop level parallelism within a node. Let us denote by N_{species} the number of ion species and by N_{μ} the number of μ values. As the magnetic momentum μ is an adiabatic invariant it plays the role of a parameter. So for each species we have N_{μ} independent Boltzmann equations (5) to solve. Let N_r , N_{θ} , N_{φ} and $N_{v_{G\parallel}}$ be the number of points in each direction r , θ , φ and $v_{G\parallel}$. Large data structures are used in GYSELA: 5D data of size $N_r \times N_{\theta} \times N_{\varphi} \times N_{v_{G\parallel}} \times N_{\mu}$ for distribution functions and 3D data of size $N_r \times N_{\theta} \times N_{\varphi}$ for the electrostatic potential and its derivatives as for first moments of the distribution function (used for diagnostics). An MPI parallelization is mandatory to treat such large amount of data. Let us take the example of a typical 5D mesh used for our simulations,⁵ namely $(N_r \times N_{\theta} \times N_{\varphi} \times N_{v_{G\parallel}} \times N_{\mu}) = (256 \times 128 \times 128 \times 128 \times 16)$. It corresponds to a mesh of almost 8.6 billion points. The size of one 5D array for the distribution function is of the order of 68 Gbytes, which is not tractable on a single node. For information, the biggest simulation run so far with GYSELA was an ITER simulation [94] with 272 billion points. Taking into account the fact that two distribution functions are necessary for the numerical integration over time due to predictor–corrector scheme, more than 1 Tbytes of data (just for 5D arrays) were manipulated. So, as described in the following, we use a domain decomposition so that a MPI process never contains the complete 5D distribution function.

Concerning the MPI parallelization, an MPI communicator is defined per species. Inside each one of the MPI_SPECIES communicators, an MPI communicator is defined for each value of the magnetic moment μ . Within each MPI_MU communicator a 2D domain decomposition allows us to assign to each MPI process a sub-domain in (r, θ) dimensions. Let us consider p_r (resp. p_{θ}) the number of sub-domains in r (resp. θ) direction. The number of MPI processes used during one run is equal to $N_{\text{MPI}} = p_r \times p_{\theta} \times N_{\mu} \times N_{\text{species}}$. This MPI decomposition of the default MPI_COMM_WORLD communicator is summarized in Fig. 3. Thus, each MPI process is then responsible for the sub-domain of the distribution function $\bar{F}_s(r = [i_{\text{start}}, i_{\text{end}}], \theta = [j_{\text{start}}, j_{\text{end}}], \varphi = *, v_{G\parallel} = *, \mu = \mu_{\text{id}})$ with the integer $\mu_{\text{id}} \in [0, N_{\mu} - 1]$. The local values i_{start} , i_{end} , j_{start} and j_{end} associated to the

⁵ For current GYSELA simulations, N_{μ} is chosen equal to 16 or 32 while the choice of $N_{v_{G\parallel}}$ is much larger (typically, $N_{v_{G\parallel}} \sim 4N_{\mu}$). Notice however that N_{μ} should be compared to $N_{v_{G\parallel}}/2$, since the grid in μ goes from 0 to μ_{max} , while that in $v_{G\parallel}$ covers the range $-v_{G\parallel, \text{max}}$ to $+v_{G\parallel, \text{max}}$. The choice of $N_{v_{G\parallel}} > 128$ is necessary to take correctly into account the trapping and de-trapping of particles and also to solve accurately the collision operator (at this time, only in parallel velocity). The same number of points for μ direction will be required when collision operator effects will be added in perpendicular direction (mandatory step for kinetic electrons).

parallel decomposition are initially set by using a classical domain decomposition in $(p_r \times p_{\theta})$ blocks. The OpenMP paradigm is used in addition to MPI. Let us denote by N_{thread} the number of threads in each MPI process, then the number of cores for a simulation corresponds to $N_{\text{thread}} \times N_{\text{MPI}}$.

3.2.1. Parallel Vlasov solver: How to treat non-local interpolation aspects?

A difficulty when parallelizing the semi-Lagrangian Vlasov solver is due to the cubic spline interpolation. Cubic splines are a good compromise between simplicity and accuracy but a drawback is that they are non-local. Indeed, a lot of the values of the distribution function F_s are required to reconstruct the interpolated value of the function at any position in the domain. Two strategies are available in the code to overcome the problem: (i) local cubic spline interpolation or (ii) transposition. The Hermite spline interpolation on patches [95–97] has been specifically developed for dealing with 2D domains distributed on several MPI processes. The idea is to compute local cubic spline coefficients on each 2D (r, θ) sub-domains by solving reduced linear systems. Then one ensures a C^1 global interpolator similar to the sequential one by imposing Hermite boundary conditions at the interface of each patch [95]. The first limitation of this technique is that a minimum of 32 points per directions is needed per MPI process [97] (*i.e.* $N_r/p_r \geq 32$ and $N_{\theta}/p_{\theta} \geq 32$) to provide good numerical stability and small communication overhead (in 2D, each processor has to exchange derivatives with its 8 neighboring processors). The second constraint is that the shift at one point on the border of a sub-domain, which results from the motion along the trajectories in the 4D phase space, must not exceed the elementary cell width. This constraint is linked to the choice made to limit the size of the interface transferred between processors. This CFL condition can be extremely restrictive specially in the θ direction where large shifts can occur but also in the radial direction when a source is imposed in the case of flux-driven simulations. For these reasons the choice of a 4D data transposition is now often preferred. This transposition consists in modifying in each MPI_COMM_MU communicator the parallel decomposition of \bar{F}_s such that each processor then contains only part of the data in φ and $v_{G\parallel}$ direction but all the information in the poloidal cross-section. Standard cubic spline interpolation in (r, θ) plane are then possible. Let us define the transposition operation T_F and its inverse T_F^{-1} as

$$\bar{F}_s(r_{\text{block}}, \theta_{\text{block}}, \varphi = *, v_{G\parallel} = *, \mu = \mu_{\text{id}})$$

$$\xrightarrow{T_F} \bar{F}_s(r = *, \theta = *, \varphi_{\text{block}}, v_{G\parallel, \text{block}}, \mu = \mu_{\text{id}})$$

$$\xleftarrow{T_F^{-1}}$$

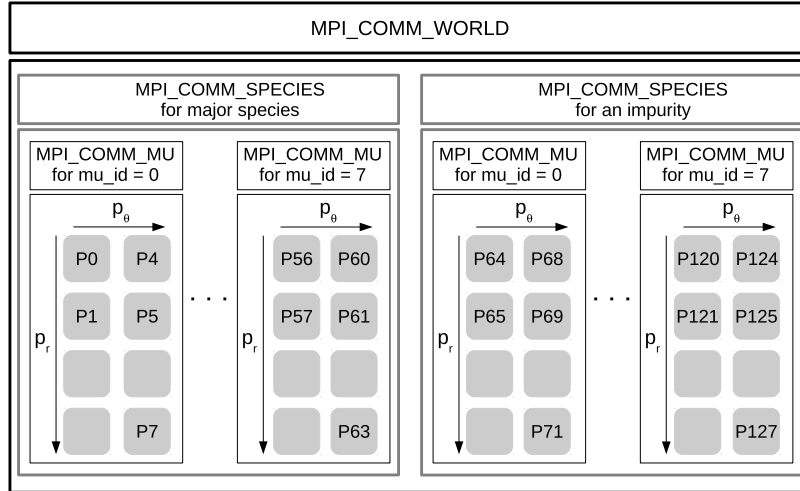


Fig. 3. MPI_COMM_WORLD communicator decomposition for two species, 8 values of μ , $p_r = 4$ radial sub-domains and $p_\theta = 2$ sub-domains in the poloidal direction. In this case, the number of MPI processes is equal to 128.

then the sequence (56) described above for solving the Boltzmann equation is replaced by the following one

$$\widetilde{\text{Boltz}}_{\text{transp}} \equiv \left[\left(\frac{\tilde{\mathcal{K}}_r}{2}, \frac{\tilde{\mathcal{D}}_r}{2}, \frac{\tilde{\mathcal{C}}}{2}, \frac{\tilde{\mathcal{S}}}{2} \right), \left(\frac{\tilde{v}_{G\parallel}}{2}, \frac{\tilde{\varphi}}{2} \right), T_F (\tilde{\mathcal{X}}_G) T_F^{-1}, \right. \\ \left. \left(\frac{\tilde{\varphi}}{2}, \frac{\tilde{v}_{G\parallel}}{2} \right), \left(\frac{\tilde{\mathcal{S}}}{2}, \frac{\tilde{\mathcal{C}}}{2}, \frac{\tilde{\mathcal{D}}_r}{2}, \frac{\tilde{\mathcal{K}}_r}{2} \right) \right].$$

3.2.2. A scalable quasi-neutral solver

The parallel quasi-neutrality algorithm presently used in the code is summarized in Algorithm 1. For more details on the different improvements which have been performed to obtain this parallel solver see [98,99]. The presence of the non-local term $(U)_{\text{FS}}(r)$ couples the θ and φ directions and penalizes the parallelization but the most important cost is the communication induced by the computation of the r.h.s, namely task 2 in algorithm 1. Indeed this calculation requires a collective communication step that involves all MPI processes. Instead of broadcasting $U(r = *, \theta = *, \varphi = *)$ to all MPI processes, a refined strategy has been setup to reduce the large communication cost. It consists in sending to each process only a sub-domain in φ direction of U . With this decomposition the gyro-average computation of U as the partial derivatives in r and θ directions are straightforward. Afterwards, a transposition is performed to calculate $\partial_\varphi U$. For a complete performance analysis of the different steps of the algorithm see [100].

3.2.3. Performing weak and strong scaling

The weak and strong scalings, presented in this section, have been performed on two different high performance computers. The strong scaling has been tested on the thin nodes of the Curie machine at TGCC,⁶ Bruyères-le-Châtel, France which are based on bullx B510 architecture. Each node contains two 8 cores processors (INTEL Xeon E5-2680 Sandy-Bridge) running at 2.7 GHz with 64 GB of 1.6 GHz memory. The weak scaling has been performed on the IBM Blue Gene/Q machine JUQUEEN at JSC/IAS,⁷ Juelich, Germany which is composed of 24 racks grouping 1024 nodes.

Each node contains a single 17-cores processor running at 1.6 GHz with 16 GB of 1.33 GHz memory. These cores are twice slower compared to Sandy Bridge cores. The improvements of the code to adapt it efficiently to the BlueGene architecture are detailed in [101]. The scaling results are detailed in Figs. 4 and 5 for the 4 main components of the code, namely (i) *Vlasov solver*, solving the Boltzmann equation as described in Section 3.2.1; (ii) *Field solver*, solving the quasi-neutrality equation as summarized in algorithm 1; (iii) *Derivatives computation*, the computation of the first derivatives of the gyroaveraged electrostatic potential $\mathcal{J}_\mu \cdot U$ in the three r , θ and φ directions and (iv) *Diagnostics* corresponding to all physical quantities from 0D to 3D computed and saved in HDF5 format like densities, parallel and perpendicular temperatures, velocities, fluxes, energies etc. The strong scaling has been performed with the mesh size parameters $N_r = 512$, $N_\theta = 512$, $N_\varphi = 128$, $N_{v_{G\parallel}} = 128$ and $N_\mu = 32$. The number of threads was kept constant $N_{\text{thread}} = 8$ to assign two MPI processes per node. The couple (p_r, p_θ) of processors in r and θ directions take the following values (2, 4), (8, 2), (8, 4), (16, 4), (16, 8) and (16, 16) so that the scaling spans from 2048 to 65 536 cores. For the weak scaling the testbed case was composed from 64k to 458k cores. The considered meshes vary from 17.18 to 481 billion points defined with $N_r = 512$, $N_\theta = 1024$, $N_\varphi = 128$, $N_{v_{G\parallel}} = 128$ and 7 different values of $N_\mu = 2, 4, 8, 16, 32, 48$ and 56. The triplet $(p_r, p_\theta, N_{\text{thread}})$ is kept constant equal to (16, 32, 64). The number of threads is chosen equal to 64 such that a single MPI process is mapped per node and 4 threads are dedicated per core as determined for BlueGene/Q optimization. The results of both scalings are summarized in Figs. 4 and 5. Let us first remark that the weak scaling test (Fig. 5) exhibits an excellent scalability of the code with 90.9% of relative efficiency at 458 752 cores – which corresponds to the totality of the JUQUEEN computer – compared to 16k. Concerning the strong scaling GYSELA globally scales with a relative efficiency of 89% at 16k cores and 60.6% on 65k cores compared to 2048 cores (Fig. 4). This is already a very good result for such a semi-Lagrangian code. Looking into more detail, we see that the deterioration from 89% at 16k to 60.6% at 65k is mainly due to the diagnostics and field solver. Indeed, the Vlasov solver which represents 60% of the application at 2k cores and 48% at 65k cores exhibits a good efficiency of 74.6% at 65k processors. Conversely, the diagnostics which correspond to 37.5% of the total time for the reference case, end taking as much time as the Vlasov solver due to the decreased efficiency at 55.8%. A lot of work has already been done to improve the field solver [99,98,100] but this work must continue because an efficiency of 41% impacts the global

⁶ <http://www-hpc.cea.fr/en/complexe/tgcc.htm>.

⁷ http://www.fz-juelich.de/ias/jsc/EN/Home/home_node.html.

Algorithm 1: Quasi-neutrality algorithm in the GYSELA code

Input: $\bar{F}_s(r_{\text{block}}, \theta_{\text{block}}, \varphi = *, v_{G\parallel} = *, \mu = \mu_{\text{id}})$

1. $v_{G\parallel}$ integration of \bar{F}_s to compute within each MPI_COMM_MU communicator

$$\text{intdvpar_Fs}(r_{\text{block}}, \theta_{\text{block}}, \varphi = *, \mu = \mu_{\text{id}}) = \int J_v dv_{G\parallel} (\bar{F}_s - \bar{F}_{s,\text{eq}}).$$

2. Remapping within each MPI_COMM_MU communicator of `intdvpar_Fs` – because the gyroaverage operation requires to have all the data for each (r, θ) plane – as

$$\text{intdvpar_Fs}(r_{\text{block}}, \theta_{\text{block}}, \varphi = *, \mu = \mu_{\text{id}}) \Rightarrow \text{intdvpar_Fs}(r = *, \theta = *, \varphi_{\text{block}}, \mu_{\text{block}}).$$

3. For all φ , computation of the gyroaverage of `intdvpar_Fs` and integration over μ to obtain

$$\rho_s(r = *, \theta = *, \varphi_{\text{block}}) = \int d\mu_s \mathcal{J}_\mu \cdot (\text{intdvpar_Fs}(r = *, \theta = *, \varphi_{\text{block}})).$$

4. MPI reduction towards the N_{species} MPI_COMM_SPECIES communicators to finally compute $\rho = \sum_s Z_s \rho_s$, the right hand side of the quasi-neutrality equation (12).

5. Solving (14) and (15) to deduce $U(r = *, \theta = *, \varphi_{\text{block}})$ and broadcast to the $N_{\text{species}} \times N_\mu$ communicators.

Output: $U(r = *, \theta = *, \varphi_{\text{block}})$ on each MPI process.

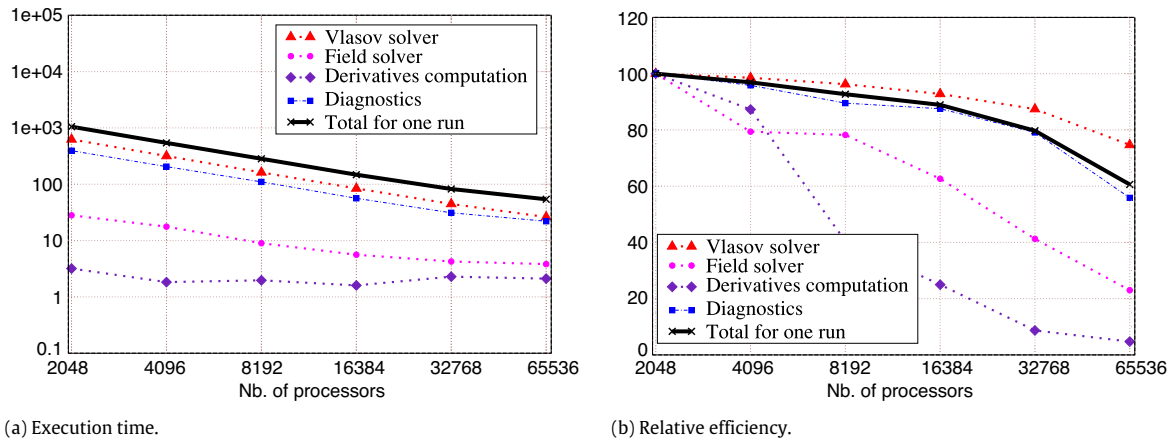


Fig. 4. Strong scaling performed on the Curie machine from 2048 to 65 536 cores: Execution time (a) and relative efficiency (b) for one GYSELA run of 4 iterations for a mesh $(N_r \times N_\theta \times N_\varphi \times N_{v_{G\parallel}} \times N_\mu) = (512 \times 512 \times 128 \times 128 \times 32)$ with 8 threads and 32 values in μ direction.

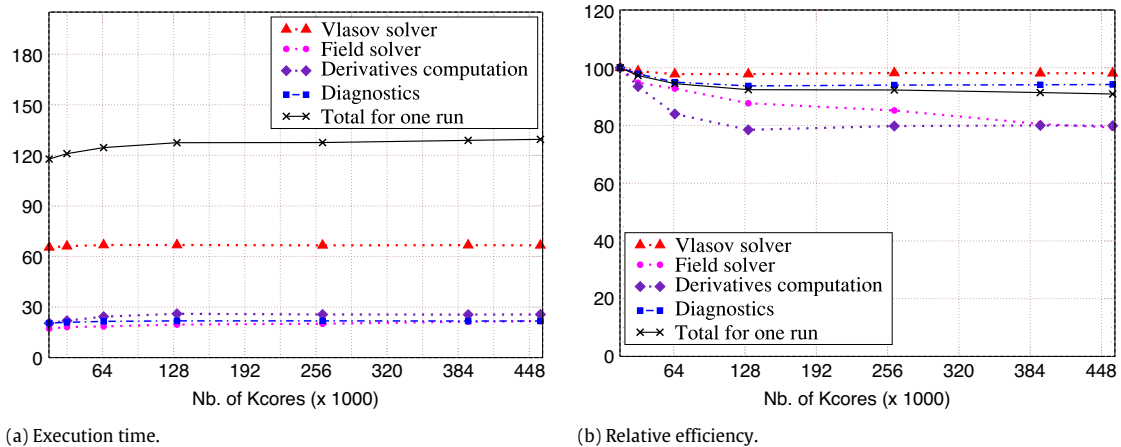


Fig. 5. Weak scaling performed on the JUQUEEN machine from 64k to 458k cores: Execution time (a) and relative efficiency (b) for one GYSELA run of 4 iterations for a mesh fixed in 4D as $(N_r \times N_\theta \times N_\varphi \times N_{v_{G\parallel}}) = (512 \times 1024 \times 128 \times 128)$ but for 7 different values of $\mu = 2, 4, 8, 16, 32, 48, 56$. The number of parallel domains in r, θ directions and the number of threads are fixed such that $(p_r, p_\theta, N_{\text{thread}}) = (16, 32, 64)$. The number of cores varies as $p_r \times p_\theta \times N_\mu \times N_{\text{thread}}/4$ because 4 threads per core are used for BlueGene optimization.

scalability. Let us finally notice that even if the computation time of the derivatives remains negligible until 16k, a further effort is needed to prepare the code to future exascale machines.

The execution times are not comparable in the two scalings presented here because the considered meshes are not the same. Performance comparisons between BlueGene/Q and Bullx

Table 1

Memory peak (in GBytes) depending on the number of MPI procs and of OpenMP threads for a 5D mesh ($N_r \times N_\theta \times N_\varphi \times N_{v_{\text{CI}}} \times N_\mu$) = $(1024 \times 1024 \times 256 \times 128 \times 16)$.

MPI procs	OpenMP threads			
	16	32	64	128
128	126.1 GB	126.9 GB	128.7 GB	132.2 GB
512	35.2 GB	36.1 GB	37.8 GB	41.3 GB
2048	16.4 GB	16.4 GB	16.5 GB	23.2 GB
8192	12.5 GB	12.5 GB	12.5 GB	19.1 GB

architectures are found in [101]. Production runs are commonly running on both architectures. In general, depending on simulation parameters, the code is a factor 2.5–3 times faster on bullx machines (as Curie or Helios at CSC, Rokkasho, Japan) than on BlueGene machines (as JUQUEEN or Turing at IDRIS, Orsay, France or Fermi at CINECA, Bologna, Italy). This behavior is consistent with that observed with many other codes.

3.2.4. Memory scalability

Due to the previous scalability results GYSELA uses frequently from 8k to 32k cores for one ion species with adiabatic electrons and the twice these values when an impurity is taken into account. Besides, a simulation often runs during several weeks. The annual time consumption on HPC machines is currently of 51 millions of core hours. So the code already benefits from petascale computational power of the current high performance computers. We also know that at short term when adding kinetic electrons, a simulation with ITER parameters on several confinement times will require exascale HPC capabilities. Among the Exascale challenges, the reduced memory per core has been identified as one of the most critical. This is particularly true for the GYSELA code due its global character which requires huge 5D meshes. The mesh discretization is already constrained by the memory required per node. The C/fortran MTM (Modelization & Tracing Memory consumption) library has been developed [102] to investigate in detail the memory consumption of the code. This library provides an Application Programming Interface (API) which replaces the standard calls to allocation/de-allocation routines. This intrusive technique permits to retrieve precisely the peak of memory consumption and all the arrays involved. External Python scripts have been designed to analyze these results and provide memory prediction. Continued efforts are made to reduce the memory footprint of the code and to improve its memory scalability (see [102] for details) but Table 1 shows that lots of work remains to be done to be able to run ITER simulations on machines with only 16 GB per node. Indeed, for a minimum ITER mesh, namely $(N_r \times N_\theta \times N_\varphi \times N_{v_{\text{CI}}} \times N_\mu) = (1024 \times 1024 \times 256 \times 128 \times 16)$, Table 1 shows that such simulations can run on Curie Machine (64 GB/node) with 8192 cores but would require 524 288 cores on the BlueGene current architecture (16 GB/node)—knowing that the optimal number of threads is 64. This number of cores is still out of reach on European high performance computers. Currently, as shown in Table 2 and in Fig. 6, the global memory scalability of the code is of 47.8%. This strong scaling was performed with a constant 5D mesh of $(1024 \times 4096 \times 1024 \times 128 \times 2)$ points using MTM prediction mode and varying the number of MPI processes from 128 to 2048 by increasing the number of points in r and θ directions. The 4D structures are very scalable (relative efficiency of 89.9%) compared to the others (see Fig. 6). Indeed, 3D structures with 23.8% represent 32% of the global cost for 32k cores against 16% for 2048 cores. The 3D structures are then no more negligible. The scalability of the 1D structures is with 19% of the order of the 3D arrays but the cost is still not significant. At the opposite, the incompressibility of 2D structures between 256 and 2k MPI processes is extremely penalizing leading to an increase of the cost percentage by a factor 10. The fact that the memory for 2D

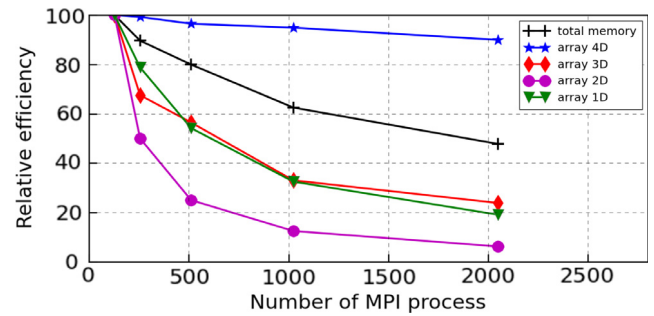


Fig. 6. Memory relative efficiency for a GYSELA simulation at the memory peak of time consumption for the four kinds of structures used in the code (1D arrays to 4D arrays). The results are extracted from Table 2. The reference point corresponds to 128 MPI processes.

structures remains constant (equal to 7.1 GBytes) is probably due to incompressible temporary arrays allocated for OpenMP loops. Improvement of memory footprint of 3D and 2D structures will be pursued in the future.

Another bottleneck for Exascale applications will be the possibly increased crash probability following that of the number of cores of future machines [103]. The Weibull law [104] gives an estimate of the time between two crashes which is of the order of the minute for a number on nodes larger than 10^5 . Two approaches have been explored until now to try to improve the fault tolerance of the code. The first one consists in employing an asynchronous method to increase the frequency of the restart file writing. A GYSELA simulation runs typically several days or even weeks. So the complete simulation is split into a series of jobs of approximately 10 h with automatic re-submission. The restart files are not only saved at the end of each job but several times during the job in parallel to calculations (see [105] for complete description). Another checkpointing using the FTI library [106] (high performance Fault Tolerance Interface for hybrid systems) is under investigation. The main idea is to benefit from fast access local SSD disks available on some HPC architectures.

4. GYSELA verification

Since the first steps 15 years ago, the code has evolved significantly, including more and more physics with more and more numerical complexity and high level of parallelism. Portability of the code on several HPC architectures has been achieved. In such a complex code it becomes very difficult to track or to propagate changes by being sure to reproduce previous results and simulations. Over the past two years, a large effort has been made to improve the development process with due regard to modularity, reproducibility and efficiency. This approach is based on the joint use of a version control system (GIT⁸) together with that of a continuous integration platform such as JENKINS.⁹ At each commit on the GIT reference branch, automatic compiling and executing are submitted. For more details on our strategy the reader can refer to [107]. A database of non-regression tests is also under construction with the objective to be run less frequently (every night or week) but to ensure that new changes have no impact on well-established results. All the tests proposed in this section, which were used for GYSELA verification,¹⁰ are detailed with the objective to become part of the non-regression database. They all correspond to 5D gyrokinetic simulations for one species. Other verification tests can be founded on simpler 4D models in [32,93].

⁸ <http://git-scm.com/>.

⁹ <http://jenkins-ci.org>.

¹⁰ The numerical results presented in the following are based on the GIT release 17.0 of the code.

Table 2
Strong scaling for each kind of data for a 5D mesh ($1024 \times 4096 \times 1024 \times 128 \times 2$): (first lines) memory allocation size in GBytes and (second lines) percentage with respect to the total memory at the peak of the memory consumption.
Source: Table from [102].

Number of cores		2k	4k	8k	16k	32k
Number of MPI processes		128	256	512	1024	2048
4D structures	Memory size	207.2 GB	104.4 GB	53.7 GB	27.3 GB	14.4 GB
	Memory percentage	79.2%	71.5%	65.6%	52.2%	42.0%
3D structures	Memory size	42.0 GB	31.1 GB	18.6 GB	15.9 GB	11.0 GB
	Memory percentage	16.1%	21.3%	22.7%	30.4%	32.1%
2D structures	Memory size	7.1 GB	7.1 GB	7.1 GB	7.1 GB	7.1 GB
	Memory percentage	2.7%	4.9%	8.7%	13.6%	20.8%
1D structures	Memory size	5.2 GB	3.3 GB	2.4 GB	2.0 GB	1.7 GB
	Memory percentage	2.0%	2.3%	3.0%	3.8%	5.1%
Total per MPI process in GBytes		261.5	145.9	81.8	52.3	34.2

4.1. Normalization

The GYSELA code is written in normalized units based on the following normalization choices. We use SI units and a thermal energy scale in electron volts ($1 \text{ eV} = 1.6022 \cdot 10^{-19} \text{ J}$). The four fundamental dimensional normalizing quantities are: a reference ionic mass $m_0 = A_0 m_p$ (Kilogram), a reference ionic charge $q_0 = Z_0 e$ (Coulomb), a reference magnetic induction B_0 (Tesla) and a reference thermal energy T_0 (eV). Here, A_0 and Z_0 are the (dimensionless) mass number and charge state of the main ion species and e the modulus of the electron charge. These quantities are used to define the reference ion cyclotron frequency Ω_{c_0} , the reference thermal speed v_{T_0} and the reference Larmor-radius ρ_0 as $\Omega_{c_0} = \frac{Z_0 e B_0}{m_0}$, $v_{T_0} = \sqrt{\frac{T_0}{m_0}}$ and $\rho_0 = \frac{v_{T_0}}{\Omega_{c_0}} = \frac{\sqrt{T_0 m_0}}{Z_0 e B_0}$. Finally, we choose the equilibrium electron density at mid radius n_0 as reference density. Physical quantities (mass, length, time, charge and density) can be recovered from the normalized quantities used in the code (denoted with a hat symbol) by choosing values for $[A_0, Z_0, B_0, T_0, n_0]$ and applying $m_s = A_s m_p = m_0 \hat{A}_s$ with $A_s = A_0 \hat{A}_s$, $q_s = Z_0 e \hat{Z}_s$, $l = \rho_0 \hat{l}$, $t = \frac{\hat{t}}{\Omega_{c_0}}$ and $n_s = n_0 \hat{n}_s$. The velocities are normalized to the corresponding thermal velocities $v_{T_{s0}} = \sqrt{T_0/m_s}$, i.e. $v = v_{T_{s0}} \hat{v}_s = \frac{v_{T_0}}{\sqrt{\hat{A}_s}} \hat{v}_s$. The main normalizations are thus $U = \frac{T_0}{Z_0 e} \hat{\phi}$, $B = B_0 \hat{B}$, $T_s = T_0 \hat{T}_s$ while $\mu_s = \frac{T_0}{B_0} \hat{\mu}_s$ with $\hat{\mu}_s = \frac{\hat{v}_s^2}{2\hat{B}}$ and $\mu_0 \mathbf{j} = \frac{B_0}{\rho_0} \hat{\mathbf{j}}$ with $\hat{\mathbf{j}} = \hat{\mathbf{V}} \times \hat{\mathbf{B}}$. By deduction, $\mathbf{E} = E_0 \hat{\mathbf{E}}$ with $E_0 = v_{T_0} B_0$ and the normalized distribution function \hat{F}_s , which evolves in the code, is defined as $\hat{F}_s = F_s v_{T_{s0}}^3 / n_0$. Finally, the energy is normalized to the reference thermal energy T_0 . The subsequent normalized equations used in the code are presented in Appendix D. In what follows, all the quantities considered are normalized coordinates, but hat symbols are omitted for the sake of readability.

4.2. Invariance test

In the present work the source terms are not taken into account. Let us call `simu1` a first fixed gradient simulation (i.e. no source term) for one unique species of charge Z_1 and mass A_1 and `simu2` a second one for a species of charge $Z_2 = \alpha_Z Z_1$ and mass $A_2 = \alpha_A A_1$. Then it is possible to define the other parameters of the second simulation, only depending on the multiplying factors $\alpha_Z \in \mathbb{N}$ and $\alpha_A \in \mathbb{N}$ such that both simulations `simu1` and `simu2` are identical. The idea is to define an invariance test which permits to verify that charge and mass are correctly taken into account in the code. Notice that such a transformation departs from a simple ρ_* scaling, where only the ρ_* parameter is modified (via e.g. a change of the minor radius at constant aspect ratio) [108,109]. Such a test can be defined as a non-regression test of any gyrokinetic

Table 3

Parameter dependence between two equivalent simulations. α_Z and α_A are the multiplying factors between both cases respectively for charge and mass.

	Simulation 1	Simulation 2
Charge	Z_1	$Z_2 = \alpha_Z Z_1$
Mass	A_1	$A_2 = \alpha_A A_1$
Mesh discretization	Δx_1	$\Delta x_2 = \frac{\sqrt{\alpha_A}}{\alpha_Z} \Delta x_1$
Time step Δt	Δt_1	$\Delta t_2 = \frac{\alpha_A}{\alpha_Z} \Delta t_1$
Temperature T_e	T_{e1}	$T_{e2} = \frac{1}{\alpha_Z} T_{e1}$
Collision coefficient	$K_{\text{coll}1}$	$K_{\text{coll}2} = K_{\text{coll}1}$
Krook coefficient	$K_{\text{krook}1}$	$K_{\text{krook}2} = \frac{\alpha_Z}{\alpha_A} K_{\text{krook}1}$
Diffusion coefficient	$K_{\text{diff}1}$	$K_{\text{diff}2} = \frac{1}{\alpha_Z} K_{\text{diff}1}$

code but it is not generic. It depends on the equations treated in each code. For any code, the solved equations (gyrokinetic + quasi-neutrality) are invariant under certain groups of transformations. Within these groups, the invariance is exact provided that the code actually solves the equations it is supposed to. We have derived in Appendix E such a group of transformations which leaves the solution unchanged for the GYSELA code. Seven control parameters are required $\alpha_x, \alpha_t, \alpha_{T_e}, \alpha_\phi, \alpha_{\text{coll}}, \alpha_{\text{diff}}$ and α_{krook} that respectively rescale space, time, electron temperature, electrostatic potential, collision operator, diffusion term and Krook operator. The only issue which cannot be accounted for (i.e. which cannot be rescaled) in this operation is the impact of the boundary conditions. The invariance constraints (i.e. the relationships between the various scaling factors which leave the Boltzmann equation invariant under these transformations), as summarized in Table 3, are $\alpha_x = \sqrt{\alpha_A}/\alpha_Z$, $\alpha_t = \alpha_A/\alpha_Z$, $\alpha_{T_e} = 1/\alpha_Z$, $\alpha_{\text{coll}} = 1$, $\alpha_{\text{diff}} = 1/\alpha_Z$ and $\alpha_{\text{krook}} = \alpha_Z/\alpha_A$. Then, the relation between the electrostatic potential ϕ_1 solution of the first simulation and ϕ_2 the electrostatic potential of the second one is $\phi_2 = \alpha_\phi \phi_1$ with $\alpha_\phi = 1/\alpha_Z$.

Three different simulations were run to test the invariance property of the code, considering first a reference plasma with Hydrogen (mass $A_s = 1$ and charge $Z_s = 1$), then Helium ($A_s = 4$ and $Z_s = 2$) and finally Tungsten ($A_s = 150$ and $Z_s = 50$). For the following, let us respectively call `simu1_A1Z1`, `simu2_A4Z2` and `simu3_A150Z50` these three simulations. These cases are not relevant in terms of physics but have been designed for numerical tests. The idea was to define small cases tractable as non-regression tests. So the reference simulation is based on a small plasma ($\rho_* = 1/150$) for a radial domain between 0.15ρ and 0.85ρ (with $\rho = r/a$) and for half a torus. The parallel velocity space is defined as $-7v_{T_{s0}} \leq v_{G\parallel} \leq 7v_{T_{s0}}$ and the perpendicular direction is represented by 16 values of μ between 0 and $12 T_0/B_0$. The radial profiles of density $n_{s_0}(r)$, temperature $T_{s_0}(r)$ and safety factor $q(r)$ are analytically prescribed as $d \log n_{s_0}(r)/dr = -2.2 \cosh^{-2}((\rho - 0.5)/0.04)$, $d \log T_{s_0}(r)/dr = -8 \cosh^{-2}((\rho - 0.5)/0.04)$ with $\rho = r - r_{\text{min}}/(r_{\text{max}} - r_{\text{min}})$

Table 4

Main parameters for reference simulation `simu1_A1Z1`. The velocity phase space is defined by $-nb_{vth0}v_{T_{S0}} \leq v_{C||} \leq nb_{vth0}v_{T_{S0}}$ and $0 \leq \mu \leq \mu_{\max}T_0/B_0$. Torus indicates the fraction of the torus simulated. The safety factor radial profile is defined as $q(r) = q_1 + q_2 \exp(q_3 \log(r/a))$. The radial density profile is defined by its gradient as $d \log n_{S_0}(r)/dr = -\kappa_{n_{S_0}} \cosh^{-2}((r - 0.5)/\Delta r_{n_{S_0}})$. The same analytical expression is used for the temperature with $\kappa_{T_{S_0}}$ and $\Delta r_{T_{S_0}}$.

N_r	N_θ	N_φ	$N_{v_{C }}$	N_μ	nb_{vth0}	μ_{\max}	
256	256	128	128	16	7.	12.	
ρ_*	R_0/a	r_{int}/a	r_{ext}/a	Torus	Z_s	A_s	$\Omega_{c_0} \Delta t$
1/150	3.3	0.15	0.75	1/2	1.	1.	5.
q_1	q_2	q_3	$\kappa_{n_{S_0}}$	Δn_{S_0}	$\kappa_{T_{S_0}}$	ΔT_{S_0}	T_i/T_e
1.5	1.7	2.8	2.2	0.04	8.	0.04	1.

Table 5

Main parameters for `simu1_A1Z1` simulation concerning buffer region and collisions. B_L and B_S correspond respectively to the location and the stiffness of the buffer regions where both diffusion and Krook operator are applied with respective amplitude D_{coeff} and $\text{Krook}_{\text{coeff}}$. The collision operator is applied every $nb_{\text{step}}_{\text{coll}}$ iterations but refreshed every $nb_{\text{refresh}}_{\text{coll}}$ iterations.

Buffer region					Collision operator		
B_L	B_S	D_{coeff}	$\text{Krook}_{\text{coeff}}$	$v_{*,\text{buff}}$	$v_{*,\text{coeff}}$	$nb_{\text{step}}_{\text{coll}}$	$nb_{\text{refresh}}_{\text{coll}}$
0.06	0.017635	0.015	0.01	20.	0.28	1	10

Table 6

Modified parameters according to the scaling law for the three simulations used in invariance tests.

	A_s	Z_s	$1/\rho_*$	τ	$\Omega_{c_0} \Delta t$	$\Omega_{c_0} \Delta t_{\text{diag}}$	D_{coeff}	$\text{Krook}_{\text{coeff}}$
<code>simu1_A1Z1</code>	1.	1.	150.	1.	5.	50.	0.015	0.01
<code>simu2_A4Z2</code>	4.	2.	150.	2.	10.	100.	0.0075	0.005
<code>simu3_A150Z50</code>	150.	50.	36.7423	50.	15.	150.	0.0003	0.00333333

and $q(r) = 1.5 + 1.7 \exp(2.8 \log(r/a))$. A Krook operator (see Section 2.10) of amplitude 0.01 and a diffusion (Eq. (50)) of 0.015 are applied in a buffer region defined by Eq. (49) with a location $B_L = 0.06$ and a stiffness of 0.017635. The collision operator (Eq. (30)) is applied every iterations while $T_{s,\text{coll}}$ (Eq. (32)) and $V_{||s,\text{coll}}$ (Eq. (31)) are refreshed every 10 iterations. All the numerical parameters of this `simu1_A1Z1` simulation are summarized in Tables 4 and 5. So taking into account the equivalences defined in Table 3, the second simulation `simu2_A4Z2` is defined with the same parameters as `simu1_A1Z1` except the fact that Helium is considered instead of Hydrogen and (i) $\tau = 2.$, (ii) $\Omega_{c_0} \Delta t = 10.$, (iii) $D_{\text{coeff}} = 0.0075$, (iv) $\text{Krook}_{\text{coeff}} = 0.005$ while (v) the diagnostic time step $\Omega_{c_0} \Delta t_{\text{diag}} = 100$ instead of 50. The species concentration c_s has been divided by 2 to satisfy the constraint $\sum_s c_s Z_s = 1$. The third simulation `simu3_A150Z50` is performed for a Tungsten species $A_s = 150$ and $Z_s = 50$ and differs from `simu1_A1Z1` by the following parameters: (i) $1/\rho_* = 36.7423 (1/\rho_{*,\text{simu1}} \times \sqrt{150/50})$, (ii) $c_s = 0.02$, (iii) $\tau = 50$, (iv) $\Omega_{c_0} \Delta t = 15$, (v) $\Omega_{c_0} \Delta t_{\text{diag}} = 150$, (vi) $D_{\text{coeff}} = 0.0003$ and (vii) $\text{Krook}_{\text{coeff}} = 0.01/3$. The differences between the three considered simulations are highlighted in Table 6. The time evolution of the zonal flow component ($m = 0$, $n = 0$), where m and n are respectively poloidal and toroidal mode number in the middle of the radial domain is presented in Fig. 7 for the three simulations. It exhibits a relative error of 10^{-15} when Hydrogen case is compared to Helium case and of 10^{-7} when compared with Tungsten simulation. The loss of accuracy for Tungsten is probably due to the small size of the plasma considered ($a = 36.7423/\rho_0$). In this case boundary conditions can play a more important role. For each test the results are sufficiently accurate to consider that the charge and mass factors have been correctly implemented in the code equations. The same order of magnitude is obtained when the distribution function values are compared.

The same invariance exercise was performed for a smaller reference case: $\rho_* = 1/75$, $N_r = 128$, $N_\theta = 128$ and a full torus (all the other simulation parameters being identical to the ones described in Tables 4 and 5). The two other simulations defined for comparison follow the same rules as previously which corresponds to a ρ_* of 1/18.37 for the Tungsten case. The relative error is also of the order of 10^{-15} when comparing Hydrogen and Helium but of

10^{-6} when considering the Tungsten. The two cases $\rho_* = 1/75$ for Hydrogen and Helium will be good candidates as non-regression tests. Regarding the Tungsten simulations more work could be done. The first idea would be to consider a $\rho_* = 1/75$ plasma for Tungsten, but this would imply a reference case with $\rho_* \sim 1/306.205$ for the Hydrogen (i.e a mesh of the order of 68 billion of points with $(N_r, N_\theta, N_\varphi, N_{v_{C||}}, N_\mu) = (512, 512, 128, 128, 16)$). Such a simulation is feasible but extremely time consuming for a verification test (several hours on 8192 cores). It would not be possible on the development cluster Poincare (92 nodes of 8 Sandy Bridge E5-2670 bi-processors (2.60 GHz)) at IDRIS French supercomputing center that has been used for all tests presented above (performed on 512 cores).

4.3. Usual linear and non-linear gyrokinetic benchmarks

Together with the verification invariance test described above, several other benchmarks have already been performed in the past to validate the code. The so-called ‘‘Rosenbluth–Hinton test’’ (R–H) [110] – which became an essential test for gyrokinetic codes to check the validity of zonal flows and Geodesic-Acoustic-Modes (GAMs) treatment – was verified in 2008 [111]. Linear and non-linear benchmarks were successfully achieved [111] with the classical Cyclone DIII-D base case (CBC) [112]. Non-linear benchmarks were also performed [46] with the global PIC code ORB5 [17]. We also participated to the European turbulence code benchmarking effort [43]. Finally, flux-driven simulations have been compared [53] between GYSELA, ORB5 and XGC1 [113,19]. In the following we present only the tests which have been recently investigated again with the new multi-species version of the code to be added as non-regression tests, namely the R–H test and the linear CBC test. These tests have been re-designed with the objective of being sufficiently small to be automatically launched on the continuous integration platform (JENKINS) at a reasonable frequency with the aim of recovering the predicted results. Here are described the results of our investigation. This work is still in progress and we plan to continue decreasing the CPU time consumption of such tests in the future.

Table 7
Common parameters for Rosenbluth–Hinton test. The velocity phase space is defined by $-nb_{vth0}v_{T50} \leq v_{G\parallel} \leq nb_{vth0}v_{T50}$ and $0 \leq \mu \leq \mu_{\max}T_0/B_0$. Torus indicates the fraction of the torus simulated. The safety factor radial profile is defined as $q(r) = q_1 + q_2 \exp(q_3 \log(r/a))$. The radial density profile is defined by its gradient as $d \log n_{s0}(r)/dr = -\kappa_{ns0} \cosh^{-2}((r - r_{\text{peak}}/a)/\Delta r_{ns0})$. The same analytical expression is used for the temperature with κ_{T50} and Δr_{T50} .

ρ_*	A_s	Z_s	R_0/a	r_{int}/a	r_{ext}/a	Torus	nb_{vth0}	μ_{\max}
1/100	1.	1.	2.78	0.2	0.8	1.	7.	12.
q_1	q_2	q_3	r_{peak}/a	κ_{ns0}	Δ_{ns0}	κ_{T50}	Δ_{T50}	T_i/T_e
1.9	0.	0.	0.5	$1.e^{-7}$	0.2	$1.e^{-7}$	0.2	1.

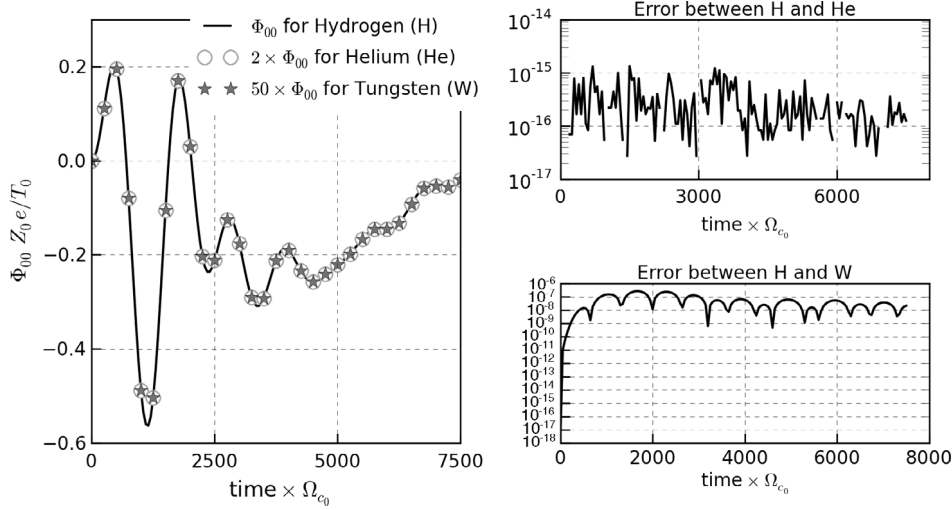


Fig. 7. Invariance test between three simulations. Left figure: Time evolution of zonal flows Φ_{00} at a fixed radial position 0.5ρ with $\rho = (r_{\text{max}} - r_{\text{min}})/a$. Φ_{00} for simu1_A1Z1 with Hydrogen must be compared to $2\Phi_{00}$ of simu2_A4Z2 for Helium and $50\Phi_{00}$ obtained with simu3_A150Z50 for Tungsten. Right figures: Relative errors in function of time: (top) between simu1_A1Z1 and simu2_A4Z2, (bottom) between simu1_A1Z1 and simu3_A150Z50.

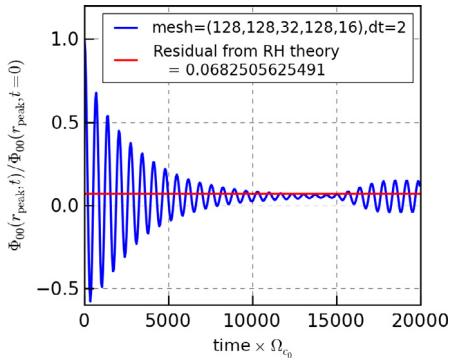


Fig. 8. Comparison of the residual value of the $(0, 0)$ mode $\phi_{00}(r_{\text{peak}}, t)/\phi_{00}(r_{\text{peak}}, t=0) = A_r$ where $A_r = 1/(1 + 1.6q^2/\sqrt{r/R}) = 0.06825$ is given by Rosenbluth–Hinton theory. This result corresponds to simulation 1 described in Table 8.

4.3.1. Rosenbluth–Hinton test as a non-regression test

This test consists in computing the linear evolution of the zonal flow component ϕ_{00} for an initial electrostatic perturbation. In practice it corresponds to initializing the code with the distribution function $\bar{F}_s = \bar{F}_{s,eq}(1 + \epsilon \sin(2\pi(r - r_{\text{min}})/2L_r))$ with a perturbation amplitude ϵ equal to 10^{-3} . This initial state leads to the development of GAMs which correspond to the $(m, n) = (0, 0)$ mode coupled to sidebands $(m, n) = (\pm 1, 0)$ as a result of toroidal coupling. These GAMs are Landau-damped because of the finite poloidal wavenumber of the sideband while the zonal flows relax towards a residual value which has been analytically predicted in the case of large aspect ratio and small ρ_* [114] as $\phi_{00}(t_\infty) = \phi_{00}(t_0) \times A_r$ with $A_r = 1/(1 + 1.6q^2/\sqrt{r/R})$, r being the minor radius of the considered magnetic surface, R and q corresponding respectively to the major radius and the safety factor on this surface of interest. Eight simulations (detailed in Table 8) were performed varying both time and phase space discretizations. For all simulations

(see Table 7 for common parameters), the safety factor profile is constant ($q(r) = 1.9 \forall r \in [r_{\text{min}}, r_{\text{max}}]$). The density and temperature profiles are quasi-constant with $\kappa_{T50} = \kappa_{ns0} = 10^{-7}$. Time evolution of the $(0, 0)$ mode is plotted in Fig. 8 for the highest discretized simulation (simu 1 in Table 8). The theoretically predicted residual value A_r is found to be recovered up to 20% in this case. A much better agreement can be found by decreasing the ρ_* value of the simulation as noticed by Biancalani (see figure 4 in [115]). One of the possible reasons is that the radial boundaries may have a stronger impact at large ρ_* values. A detailed analysis of both the transient GAM oscillation and damping on the one hand, and of the residual value of zonal flows on the other hand, is presented in Appendix F. The numerical echo appearing at time $t = 15000\Omega_{c0}^{-1}$ is due to finite discretization of the velocity phase space. The numerical damping rates γ_{GAM} and frequencies ω_{GAM} reported in Table 8 are all computed between $t \in [0, 15000\Omega_{c0}^{-1}]$. We observe that all the values are equal to $\gamma_{\text{GAM}} = 2.46459 \cdot 10^{-4}\Omega_{c0}$ and $\omega_{\text{GAM}} = 9.11061 \cdot 10^{-3}\Omega_{c0}$ with an error smaller than 3% except for simulations number 4, 6 and 8 in Table 8. The error larger than 7% for both simulations 4 and 6 is due to the fact that the numerical echo appears at time $t = 9000\Omega_{c0}^{-1}$ instead of $t = 15000\Omega_{c0}^{-1}$, making the numerical residual estimation impossible. Error in simulation 4 is due to the fact that four values of μ are not sufficient for μ integral computation required for the r.h.s. of the quasi-neutrality equation. Results for simulation 6 shows that 64 in parallel velocity direction are not sufficient. The CPU times reported as results in Table 8 correspond to mono-core hours on the Poincaré machine where all simulations were performed with 4 threads and $(2 \times N_\mu)$ MPI processes for a final time equal to $t = 20000\Omega_{c0}^{-1}$. Simulation 7 corresponding to 30 min on 64 cores is a non-regression test for the code.

4.3.2. Linear benchmark based on Cyclone DIII-D case for global codes

For the present benchmark, the considered physical parameters are the same as the ones defined in Lapillonne's paper [116]

Table 8

Rosenbluth–Hinton test: Values of numerical damping γ_{GAM} and frequency ω_{GAM} for 8 GYSELA simulations varying according to 5D mesh size (N_r , N_θ , N_φ , $N_{v_{\parallel}}$, N_μ) and time discretization.

Simu.	N_r	N_θ	N_φ	$N_{v_{\parallel}}$	N_μ	$\Omega_{C_0} \Delta t$	γ_{GAM}	ω_{GAM}	CPU time (monoproc)
1	128	128	32	128	16	2.	$2.46459 \cdot 10^{-4}$	$9.11061 \cdot 10^{-3}$	7219. h.
2	128	128	32	128	16	5.	$2.46459 \cdot 10^{-4}$	$9.11061 \cdot 10^{-3}$	2921. h.
3	64	64	16	128	8	5.	$2.46459 \cdot 10^{-4}$	$9.11061 \cdot 10^{-3}$	159. h.
4	64	64	16	128	4	5.	$2.63456 \cdot 10^{-4}$	$9.73893 \cdot 10^{-3}$	79. h.
5	64	64	16	128	8	10.	$2.46459 \cdot 10^{-4}$	$9.11061 \cdot 10^{-3}$	41. h.
6	64	64	16	64	8	10.	$2.54957 \cdot 10^{-4}$	$9.42477 \cdot 10^{-3}$	83. h.
7	64	64	16	128	8	25.	$2.46459 \cdot 10^{-4}$	$9.11061 \cdot 10^{-3}$	37. h.
8	64	64	16	128	8	50.	$2.54957 \cdot 10^{-4}$	$9.42477 \cdot 10^{-3}$	21. h.

Table 9

Main parameters of the $\rho_* = 1/180$ linear CBC simulation. The velocity phase space is defined by $-\text{nb}_{v_{\parallel}0} v_{r_{\text{so}}} \leq v_{\parallel} \leq \text{nb}_{v_{\parallel}0} v_{r_{\text{so}}}$ and $0 \leq \mu \leq \mu_{\text{max}} T_0/B_0$. The safety factor radial profile is defined as $q(r) = q_1 + q_2(r/a) + q_3(r/a)^2$. The radial density profile is defined by its gradient as $d \log n_{\text{so}}(r)/dr = -\kappa_{n_{\text{so}}} \cosh^{-2}((r - 0.5)/\Delta r_{n_{\text{so}}})$. The same analytical expression is used for the temperature with $\kappa_{T_{\text{so}}}$ and $\Delta r_{T_{\text{so}}}$.

ρ_*	R_0/a	r_{int}/a	r_{ext}/a	$\text{nb}_{v_{\parallel}0}$	μ_{max}	Z_5	A_5
1/180	2.78	0.1	0.9	6.	7.	1.	1.
q_1	q_2	q_3	$\kappa_{n_{\text{so}}}$	$\Delta_{n_{\text{so}}}$	$\kappa_{T_{\text{so}}}$	$\Delta_{T_{\text{so}}}$	T_i/T_e
0.86	-0.16	2.52	2.23	0.3	6.96	0.3	1.

Table 10

CBC results: Linear growth rate γ and frequencies ω estimated in the time interval $\Omega_{C_0} [t_{\text{init}}, t_{\text{end}}]$ for 6 different toroidal mode numbers n . The poloidal wave number k_θ is computed as $k_\theta \rho_* = |n|q(r_{\text{peak}})\rho_*/r_{\text{peak}} = |n| \times 1.4/(2 \times 180)$, r_{peak} being the middle of the radial box. These results are compared to GENE results in Fig. 9.

n	m_{max}	N_θ	N_φ	$k_\theta \rho_*$	$\Omega_{C_0} \Delta t$	$\Omega_{C_0} [t_{\text{init}}, t_{\text{end}}]$	γ	err_γ	ω
-5	7	256	128	0.078	40.	[5000, 50 000]	0.045	0.00258	0.106
-10	14	256	128	0.156	40.	[4000, 18 000]	0.158	0.0069	0.238
-15	21	256	128	0.233	40.	[4000, 18 000]	0.217	0.00123	0.476
-20	25	256	128	0.311	10.	[4000, 18 000]	0.257	0.00127	0.636
-25	35	512	256	0.389	10.	[4000, 18 000]	0.271	0.00468	0.827
-30	42	512	256	0.467	10.	[4000, 18 000]	0.253	0.002	0.978

corresponding to the standard linear Cyclone base case (CBC) [112]. The circular concentric magnetic equilibrium is defined with an aspect ratio of $R/a = 2.78$ and a safety factor profile $q(r) = 0.86 - 0.16r/a + 2.52(r/a)^2$. This corresponds to a local safety factor $q(r_{\text{peak}}) = 1.4$ and a local magnetic shear $s(r_{\text{peak}}) = 0.8$ with $r_{\text{peak}} = r_{\text{min}} + 0.5(r_{\text{max}} - r_{\text{min}})$ and $s(r) = (r/q) dq/dr$. The initial density and temperature profiles are defined with the radial form function $f(r) = \exp(-\kappa_X \Delta r_X \tanh((r - r_{\text{peak}})/\Delta r_X))$. The κ_X and Δr_X parameters are chosen to obtain peaked profiles at the middle of the radial box r_{peak} with $\Delta_{n_{\text{so}}} = \Delta_{T_{\text{so}}} = 0.3$, $\kappa_{n_{\text{so}}} = 2.23$ and $\kappa_{T_{\text{so}}} = 6.96$ (see Figure 1 in [116]). To be consistent with the DIII-D shot ρ_* is chosen equal to 1/180 (see Table 9).

The first difficulty with a full- f code as GYSELA is that the separation between linear and non-linear terms is not possible. So non-linear mode coupling cannot be avoided, which implies that the time window for linear growth rate estimation is limited. To prevent this coupling all the toroidal mode numbers n are filtered except the one n initialized as perturbation in the initial distribution function $\bar{F}_s(t = 0) = \bar{F}_{s,\text{eq}}(1 + \epsilon \sum_{m=1}^{m_{\text{max}}} \cos(m\theta + n\varphi + \delta_{mn}))$ with a perturbation amplitude $\epsilon = 10^{-6}$. This filtering is performed by applying, after the quasi-neutrality equation solving, the condition $\mathcal{F}(\phi)_{mn} = 0$ for all $1 \leq m \leq m_{\text{max}}$ where \mathcal{F} denotes the 2D Fourier transform in (θ, φ) . Besides, the global aspect of the code implies that large toroidal mode numbers n are hardly accessible because a large mesh discretization is then necessary. For the 6 cases which were run for $|n|$ ranging from 5 to 30 (see Table 10) the discretization of the velocity space was kept constant ($N_{v_{\parallel}}, N_\mu = (64, 16)$) but increased in real space for $|n| > 15$. The number of radial points is kept constant ($N_r = 128$) but doubled in both poloidal and toroidal directions for $|n| \geq 25$. This corresponds to a mesh of 8 billions of points for the smallest poloidal mode numbers but of 32 billions of points for the largest.

The time step Δt is equal to $40./\Omega_{C_0}$ for $|n| \geq 15$ and divided by a factor 4. The linear growth rate is estimated by a linear fit of the exponential growth of $\int \phi^2 d^3\mathbf{x} d^3\mathbf{v}$ during the linear phase. An example of this exponential growth is plotted at the top of Fig. 10 for the smallest $k_\theta \rho_* = |n|q(r_{\text{peak}})\rho_*/r_{\text{peak}} = 0.078$. So the linear fit is performed on a time interval $\Omega_{C_0} [t_{\text{init}}, t_{\text{end}}]$ depending on the duration of this linear phase. This interval is taken equal to [5000, 50 000] for $k_\theta \rho_* = 0.078$ and [4000, 18 000] for the others. The frequency is estimated on the same time intervals by spectra analysis. Both have been compared with GENE results [116] and show a very good agreement (see Fig. 9). This work is in progress in the framework of the Eurofusion project [117]. The smallest runs were performed on Poincaré machine on 512 cores (with $(p_r, p_\theta, p_\mu, N_{\text{thread}}) = (2, 4, 16, 4)$) with a CPU time cost of 9k hours/monoprocessor (for 1300 iterations). The two largest cases ran on Turing (IDRIS-France) BlueGene machine using 32 768 processors ($(p_r, p_\theta, p_\mu, N_{\text{thread}}) = (8, 4, 16, 64)$) with an expensive CPU time cost of 1.7 millions of monoprocessor hours for 2000 iterations (equivalent to $1.3 \cdot 10^6$ h on an INTEL machine as Curie (CCRT-France)). Such simulations are definitively more expensive for a global full- f code than for δf flux-tube codes. This explains why the two last points performed by GENE for $k_\theta \rho_* > 0.5$ (Fig. 9) have not been simulated with GYSELA. Nevertheless, the global aspect can give access to useful information like the time evolution of the radial structure of poloidal modes (for toroidal mode $|n| = 5$). This radial structure is plotted at 4 different times in Fig. 10, going from initialization to the end of the linear phase. It shows that the linear phase, i.e. the exponential growth, starts as soon as the global eigenmode – characterized by a single n and several m mode numbers – acquires its radial structure. The process of mode reorganization and the main physical parameters involved (as q profile, $1/L_T$ shape or...) would be interesting to investigate in more detail.

Table 11

Main parameters of the $\rho_* = 1/180$ simulation used to check conservation law properties. The velocity phase space is defined by $-\text{nb}_{v_{th0}} v_{T_{i0}} \leq v_{G\parallel} \leq \text{nb}_{v_{th0}} v_{T_{i0}}$ and $0 \leq \mu \leq \mu_{\text{max}} T_0/B_0$. Torus indicates the fraction of the torus simulated. The safety factor radial profile is defined as $q(r) = q_1 + q_2(r/a) + q_3(r/a)^2$. The radial density profile is defined by its gradient as $d \log n_{s0}(r)/dr = -\kappa_{ns0} \cosh^{-2}((r-0.5)/\Delta r_{ns0})$. The same analytical expression is used for the temperature with κ_{Ts0} and Δr_{Ts0} .

N_r	N_θ	N_ϕ	$N_{v_{G\parallel}}$	N_μ	$\text{nb}_{v_{th0}}$	μ_{max}	
256	256	128	64	16	7.	12.	
ρ_*	R_0/a	r_{int}/a	r_{ext}/a	Torus	Z_s	A_s	$\Omega_{c_0} \Delta t$
1/180	2.78	0.1	0.9	1/2	1.	1.	10.
q_1	q_2	q_3	κ_{ns0}	Δ_{ns0}	κ_{Ts0}	Δ_{Ts0}	T_i/T_e
0.86	-0.16	2.52	2.23	0.3	6.96	0.3	1.

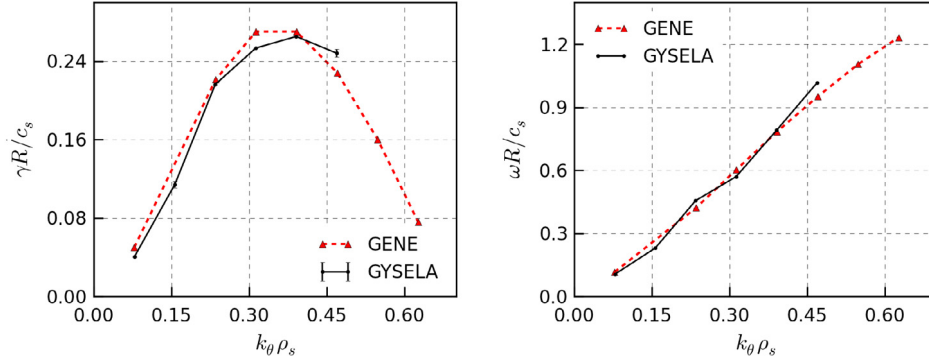


Fig. 9. Benchmark between GYSELA and GENE codes [117] for the Cyclone base case for 6 different $k_\theta \rho_s$ values: (Left) Linear growth rate (plotted with the error bar defined in Table 10), (Right) Linear frequency.

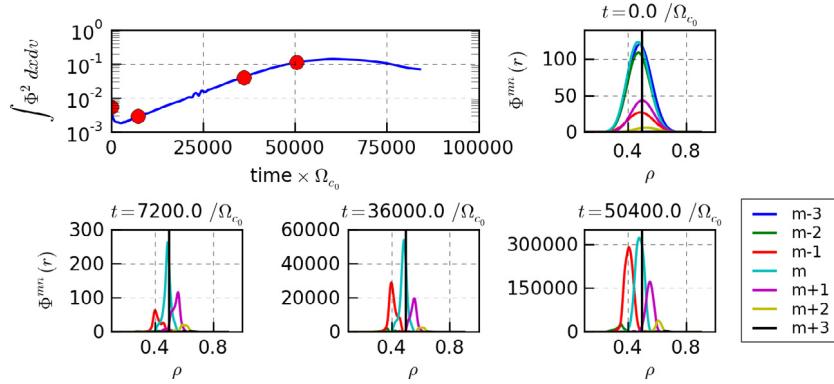


Fig. 10. Radial structure of the electrostatic potential for $(m, n) = (7, 5)$ and a bandwidth of $m \pm 3$ modes, at different times: (i) initial time, (ii) beginning of the linear phase $t = 7200 \Omega_{c_0}^{-1}$, (iii) $t = 36000 \Omega_{c_0}^{-1}$ and (iv) end of the linear phase $t = 50400 \Omega_{c_0}^{-1}$.

5. Local conservation laws

Verifying adequate conservation laws is an essential step in providing a correct description of mean flows. Since the controversy on the suitability of gyrokinetic codes for describing toroidal momentum transport [118,119] a specific effort has been devoted to address conservation equations both in the context of a reduced gyrofluid model [120] or gyrokinetic field theory [121,122]. As shown in this section, it is also possible [34] to derive local conservation equations for density, energy and toroidal momentum from the gyrokinetic electrostatic model (5)–(12) implemented in the GYSELA code (more detailed calculations can be found in Abiteboul's Ph.D. [123]). The radial force balance is presented in Section 5.1 while the conservation laws are detailed for: (i) charge density in Section 5.2, (ii) energy in Section 5.3 and toroidal momentum in Section 5.4. As explained in [34], the force balance equation added to the energy and toroidal momentum conservation equations ensures a self-consistent treatment of the radial electric field and flows. We present for each property an

example of numerical results, (see Figs. 11–14) for a simulation close to the non-linear CBC simulation proposed in [116] for $\rho_* = 1/180$. It corresponds to a collisionless simulation, with Dirichlet boundary conditions and without diffusion or Krook operators. Contrary to the linear case, there is no filtering on the toroidal modes. The initial perturbation is defined as $p(r, \theta, v_{G\parallel}) = \epsilon \sum_{m=1}^{m_{\text{max}}} \sum_{n=1}^{n_{\text{max}}} \cos(m\theta + n\varphi + \delta_{mn}) f_{eq}(r, \theta, v_{G\parallel}) / (m_{\text{max}} n_{\text{max}})$ for $m_{\text{max}} = 28$ and $n_{\text{max}} = 20$ and random values for δ_{mn} phases. The perturbation amplitude ϵ is equal to 10^{-6} . The equilibrium distribution function f_{eq} is a local Maxwellian function given by Eq. (19). The other numerical parameters of this simulation are summarized in Table 11.

The conservation equations are derived at second order in ρ_* . Accurate results (error of 2%) were already shown with the code for force balance and toroidal momentum for a simulation with $\rho_* = 1/512$ (see Figure 2 in [34]). For a larger $\rho_* = 1/180$ the results are still accurate with a relative error of 5%–10%. As expected, boundary conditions play a more important role leading to a degradation of the accuracy outside an internal region $0.4 \leq r/a \leq$

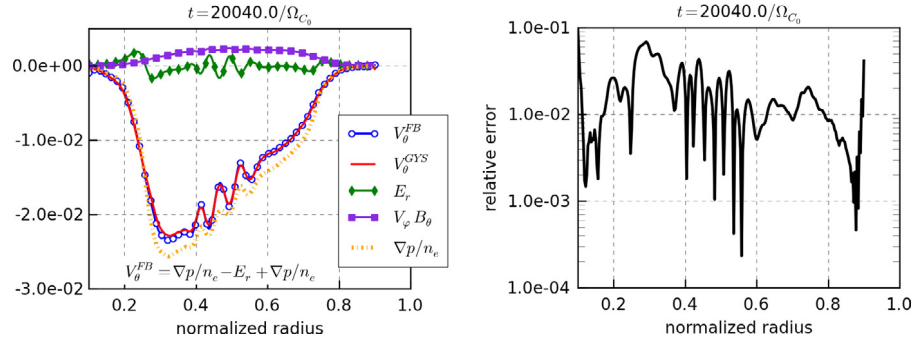


Fig. 11. Left: Numerical test of the radial force balance equation (57) at time $t = 20040.0\Omega_{c_0}^{-1}$, comparing the poloidal velocity v_θ^{GVS} directly computed in the code and v_θ^{FB} the sum of the three contributions $-E_r$, $\nabla p/n_e$ and $v_\phi B_\theta$. Right: Relative error between both. The parameters used for this simulation are summarized in Table 11.

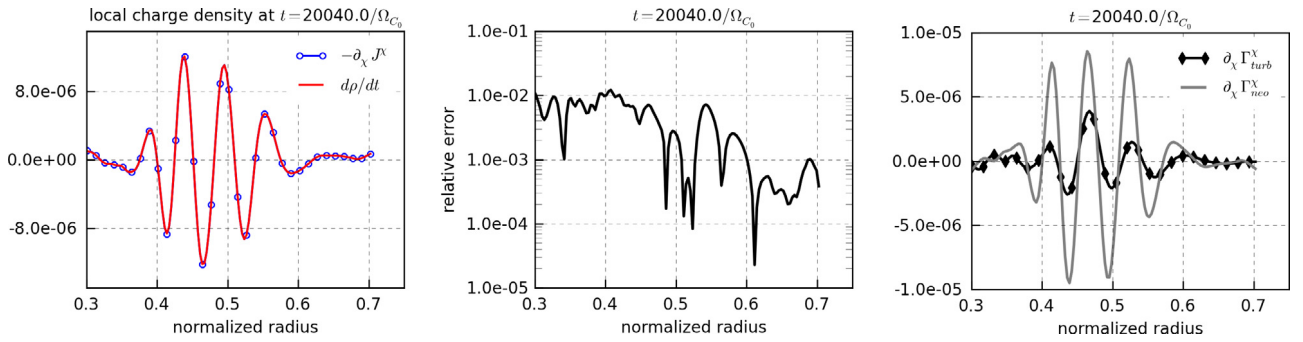


Fig. 12. Numerical test of the charge density conservation for simulation defined in Table 11. All the quantities are flux-surface averaged. Left: Comparison of the two terms $-\partial_\chi J^X$ and $d\rho/dt$ which must be equivalent according to Eq. (59). Middle: Relative error (defined as the difference normalized to the quadratic mean). Right: Contribution of the neoclassical and turbulent parts.

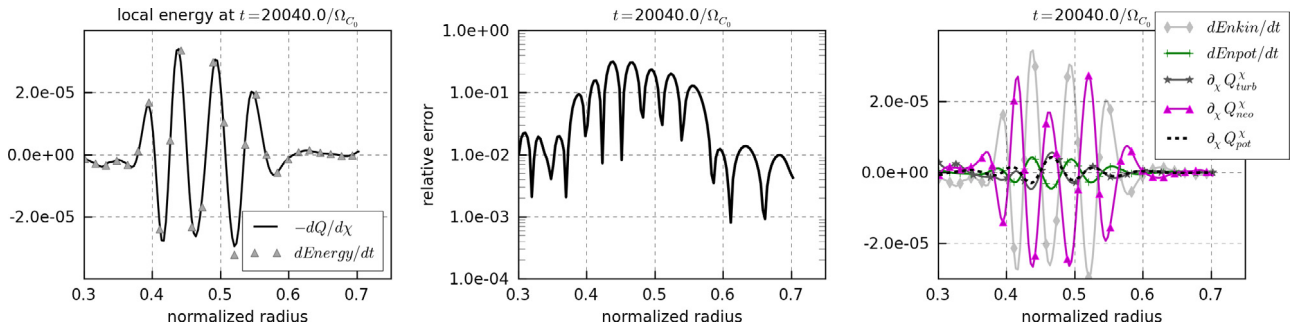


Fig. 13. Numerical test for local energy conservation for simulation defined in Table 11. Left: Comparison between $-(\partial_\chi Q)_{FS}$ and $d(E)_{FS}/dt$ with $Q = Q_s + Q_{s,pot} + Q_{s,pol}$ and $E = E_{Ks} + E_{ps}$ defined by Eqs. (66)–(71). Middle: Relative error (defined here as the difference normalized to the quadratic mean). Right: Detailed contribution of each term.

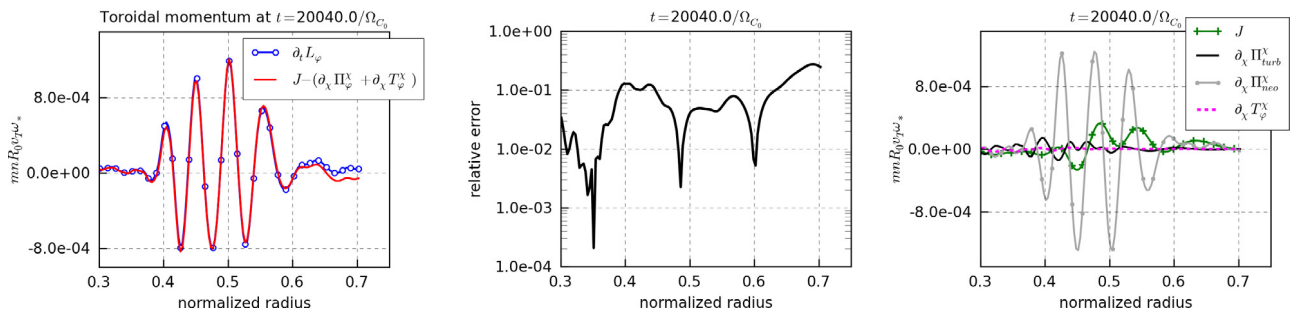


Fig. 14. Numerical test for local toroidal momentum conservation for simulation detailed in Table 11. All the quantities are flux-surface averaged. Left: Comparison between $\partial_\chi \mathcal{L}_\phi$ and $J^X - \partial_\chi \Pi_\phi^X - T_{pol}^X$ which must be equal according to Eq. (76). Middle: Relative error (defined here as the difference normalized to the quadratic mean). Right: Detailed contributions of neoclassical and turbulent parts.

0.7. Comparing to relative errors for all conservation properties (Figs. 11–14), the local energy conservation (Fig. 13) is the least accurate. It was not possible to analyze the energy behavior for smaller ρ_* (as 1/300 and 1/512) because such simulations are extremely expensive (several millions of mono-processor hours) and the diagnostic was not fully implemented in large simulations until present. This will be investigated in more detail in the upcoming big simulations. Complete flux driven simulations with source terms and collisions have also been analyzed (but not presented here). Even for large $\rho_* = 1/150$, the force balance equation, local charge density and toroidal momentum are conserved with less than 10% error even at times when turbulence is fully developed. The fact that this requirement is not met for energy is still under investigation.

5.1. Radial force balance equation

In the fluid description, the radial electric field and the flows are related via the force balance equation. It was verified that this relation holds also in gyrokinetics [33,50]. Indeed the radial force balance can be recovered analytically from the conventional first order gyrokinetic equations (see Appendix E in [34]), yielding the standard fluid expression

$$\partial_\chi \phi_{eq} + \frac{\partial_\chi P_{eq}}{n_{eq}e} + \frac{B}{I} V_{\parallel eq} = q \frac{B^2 R^2}{I^2} (\mathbf{V} \cdot \nabla \theta) \quad (57)$$

where the equilibrium density n_{eq} , pressure P_{eq} , velocity $V_{\parallel eq}$ and potential ϕ_{eq} are functions of $-P_\phi/e$ (which is approximately equal to χ at first order in ρ_s). The label of flux surfaces χ is chosen as the opposite of the poloidal flux of the magnetic field, i.e. $\chi \equiv -\psi_{pol}$ with $\psi_{pol} = -(2\pi)^{-1} \int_{S_\phi} dS \mathbf{B} \cdot \nabla \theta / |\nabla \theta|$. Considering the form of the magnetic field used presently in the code $\mathbf{B} = (B_0 R_0 / R(r, \theta)) [\zeta(r) \mathbf{e}_\theta + \mathbf{e}_\varphi]$ with $\zeta(r) = r / (q R_0)$, the label χ is determined by $\chi = B_0 \int_0^r r' / q(r') dr'$ which implies $d\chi / dr = B_0 r / q$.

In order to check that the force balance equation is verified numerically, we compare v_θ^{GYS} the poloidal velocity directly computed within GYSELA – from the distribution function as the sum of the poloidal ExB, curvature, grad-B and magnetization flows – with the expected velocity from the force balance equation, namely v_θ^{FB} corresponding to the left-hand side of Eq. (57) (see Fig. 11 (left)). This agreement was robustly verified in GYSELA simulations for a wide range of parameters for temperature gradient, collisionality and normalized gyroradius ρ_s [52,51]. A precision of 2% was obtained for a ITER parameter case with $\rho_* = 1/512$ [34]. In Fig. 11 (right), we recover this good agreement for the case $\rho_* = 1/180$ described in Table 11. Indeed, even for a larger $\rho_* = 1/180$, the relative error – defined here as the difference normalized to the quadratic mean – is smaller than 0.08 at time $t = 20\,040 \Omega_{C_0}^{-1}$ which corresponds to the beginning of the non-linear phase.

5.2. Local charge density conservation

To obtain local conservation equations, we perform integrations of the conservative form of the gyrokinetic equation (5) over the velocity space and over the magnetic flux surfaces, i.e. over $d\tau^* \equiv J_\chi d\theta d\varphi d^3\mathbf{v}$ with $d^3\mathbf{v} = J_\nu dv_{G\parallel} d\mu_s$. We recall that $J_\chi = 1 / (\mathbf{B} \cdot \nabla \theta)$ is the Jacobian in real space and $J_\nu = 2\pi B_{\parallel s}^* / m_s$ is the Jacobian in gyro-center velocity-space.

We consider a radial region outside the buffer region and without source terms, i.e. we consider the following simplified version of the conservative Boltzmann equation (5)

$$\frac{d\bar{F}_s}{dt} = \frac{\partial \bar{F}_s}{\partial t} + \frac{1}{B_{\parallel s}^*} \nabla_z \cdot (\mathbf{z} B_{\parallel s}^* \bar{F}_s) = \mathcal{C}(\bar{F}_s) \quad (58)$$

where $\mathbf{z} = (\chi, \theta, \varphi, v_{G\parallel}, \mu_s)$ and $\dot{\mathbf{z}} = d_t \mathbf{z}$. We integrate Eq. (58) in a small phase-space volume between two surfaces χ and $\chi + \delta\chi$ and apply a divergence theorem. Using the collision operator conservation property $\int \mathcal{C}(\bar{F}_s) d\tau^* = 0$ and summing over all species, this leads directly to the usual expression for local transport of charge density

$$\partial_t \bar{\rho} + \partial_\chi J^\chi = 0 \quad (59)$$

where $\bar{\rho}$ is the charge density and J^χ is the radial current of gyrocenters:

$$\bar{\rho} = \sum_{\text{species}} q_s \int d\tau^* \bar{F}_s \quad \text{and} \quad J^\chi = \sum_{\text{species}} q_s \int d\tau^* (\dot{\mathbf{z}} \cdot \nabla \chi) \bar{F}_s \quad (60)$$

Fig. 12 shows that Eq. (60) is numerically satisfied with an error of less than 1%. Part of this error is due to the fact that the time derivative $\partial_t \bar{\rho}$ is computed from post-processed data ($\bar{\rho}$ is not saved at each time step Δ_t but at each diagnostic time step ($\Delta_t^{\text{diag}} = 12 \Delta_t$ for this simulation)). Another error source is the fact that the terms $\nabla_\perp \cdot (B_{\parallel s}^* d_t \chi_G)$ and $\partial_\varphi (B_{\parallel s}^* d_t \varphi)$ are neglected in the splitting algorithm (see Section 3.1).

5.3. Local energy conservation

Similarly, a conservation equation for the total energy can be derived by multiplying the gyrokinetic equation (58) by the gyrocenter Hamiltonian, which reads

$$\bar{H}_s = \frac{1}{2} m_s v_{G\parallel}^2 + \mu_s B + q_s \bar{U} \quad \text{with} \quad \bar{U} = J_{0s} \cdot \mathbf{U}. \quad (61)$$

Using the fact that our collision operator is constructed to conserve the total Hamiltonian and integrating over $d\tau^*$ yields

$$\begin{aligned} \partial_t \int d\tau^* \left(\frac{1}{2} m_s v_{G\parallel}^2 + \mu_s B \right) \bar{F}_s + \int d\tau^* q_s \bar{U} \partial_t \bar{F}_s \\ + \int d\tau^* \bar{H}_s \frac{1}{B_{\parallel s}^*} \nabla_z \cdot (\mathbf{z} B_{\parallel s}^* \bar{F}_s) = 0. \end{aligned} \quad (62)$$

Then for each species s , Eq. (62) can be rewritten as an equation for the radial energy transport as

$$\partial_t E_{K_s} + \partial_\chi Q_s = W_s \quad (63)$$

where E_{K_s} corresponds to the kinetic energy of the gyrocenters for the species; the term Q_s is equivalent to a radial flux of energy and the right-hand side W_s appears as a kinetic energy source

$$\begin{aligned} E_{K_s} &\equiv \int d\tau^* \left(\frac{1}{2} m_s v_{G\parallel}^2 + \mu_s B \right) \bar{F}_s; \\ Q_s &= \int d\tau^* \bar{H}_s (\dot{\mathbf{z}} \cdot \nabla \chi) \bar{F}_s; \quad W_s = -q_s \int d\tau^* \bar{U} \partial_t \bar{F}_s. \end{aligned}$$

The term W_s corresponds to an exchange of energy between a given species and the turbulence, and is generally referred to as turbulent heating [124–128]. It corresponds to a transfer of energy between particles and the electromagnetic field. The numerical computation of this term is expensive because it requires saving the 5D distribution function of each species at two successive time steps which corresponds to a large amount of memory. So to obtain a local conservation equation with no source term, we consider the total energy by summing (63) over all species. Then,

$$\begin{aligned} \partial_t E_K + \partial_\chi Q = W \quad \text{with} \quad E_K = \sum_s E_{K_s}, \\ Q = \sum_s Q_s \quad \text{and} \quad W = \sum_s W_s. \end{aligned} \quad (64)$$

The term W is decomposed into two parts as

$$\begin{aligned} \sum_s q_s \int d\tau^* \bar{U} \partial_t \bar{F}_s &= \sum_s q_s \int d\tau^* U (J_{0s} \cdot \partial_t \bar{F}_s) \\ &+ \sum_s q_s \int d\tau^* \{ (J_{0s} \cdot U) \partial_t \bar{F}_s - U (J_{0s} \cdot \partial_t \bar{F}_s) \}. \end{aligned} \quad (65)$$

The first term in Eq. (65) can be expressed in function of the potential energy E_p as

$$\begin{aligned} \sum_{\text{species}} q_s \int d\tau^* U (J_{0s} \cdot \partial_t \bar{F}_s) &\equiv \partial_t E_p \\ \text{with } E_p &\equiv \frac{1}{2} \sum_{\text{species}} q_s \int d\tau^* U (J_{0s} \cdot \bar{F}_s). \end{aligned}$$

Besides, the second term $\mathcal{L}_E = \sum_s q_s \int d\tau^* \{ (J_{0s} \cdot U) \partial_t \bar{F}_s - U (J_{0s} \cdot \partial_t \bar{F}_s) \}$ in Eq. (65) corresponds to a polarization term, due to the difference between particles and gyro-center densities. As a remark, considering that the gyroaverage operator J_{0s} is a self-adjoint operator, this term vanishes when integrating over the whole phase-space volume. It is indeed the divergence of a flux in the local conservation equation. To express this term explicitly as a flux contribution, let us consider the low wavenumber approximation of the gyroaverage operator used in the code, *i.e.* the Padé approximation $J_{0s} \simeq 1 + \frac{1}{2} \nabla \cdot \left(\frac{m_s \mu_s}{q_s^2 B} \nabla_{\perp} \right)$ (see Section 2.5.1 for more details). Using this approximation, \mathcal{L}_E can be expressed for each species as

$$\begin{aligned} \mathcal{L}_E &= \frac{m_s}{2q_s} \partial_{\chi} \left[\int d\tau^* \partial_t \bar{F}_s \frac{\mu}{B} \nabla \chi \cdot \nabla_{\perp} U \right. \\ &\quad \left. - \int d\tau^* U \frac{\mu}{B} \nabla \chi \cdot \nabla_{\perp} (\partial_t \bar{F}_s) \right]. \end{aligned}$$

It can also be expressed in a more compact form using the gyro-center perpendicular stress $P_{s,\perp} = \int d^3 \mathbf{v} \bar{F}_s \mu_s B$. This leads to the following conservation equation summed over all species

$$\partial_t (E_K + E_p) + \partial_{\chi} (Q + Q_{\text{pot}} + Q_{\text{pol}}) = 0 \quad (66)$$

where $E_K = \sum_s E_{K_s}$, $E_p = \sum_s E_{p_s}$, $Q = \sum_s Q_s$, $Q_{\text{pot}} = \sum_s Q_{s,\text{pot}}$ and $Q_{\text{pol}} = \sum_s Q_{s,\text{pol}}$ with

$$E_{K_s} = \int d\tau^* \mathcal{E}_s \bar{F}_s \quad \text{with } \mathcal{E}_s = \frac{1}{2} m_s v_{G\parallel}^2 + \mu_s B \quad (67)$$

$$E_{p_s} = \frac{q_s}{2} \int d\tau^* U (J_{0s} \cdot \bar{F}_s) \quad (68)$$

$$Q_s = \int d\tau^* \mathcal{E}_s (\mathbf{z} \cdot \nabla \chi) \bar{F}_s \quad (69)$$

$$Q_{s,\text{pot}} = \int d\tau^* (J_{0s} \cdot U) (\mathbf{z} \cdot \nabla \chi) \bar{F}_s \quad (70)$$

$$Q_{s,\text{pol}} = \frac{m_s}{2q_s} \int J_{\chi} d\theta d\varphi \frac{1}{B^2} \left\{ \partial_t P_{s,\perp} \nabla U \cdot \nabla \chi - U \nabla (\partial_t P_{s,\perp}) \cdot \nabla \chi \right\}. \quad (71)$$

We recall that, although the polarization term is necessarily the divergence of a flux term, the expression for Q_{pol} given here is not exact as it relies on an approximation of the gyroaverage operator. Q_s corresponds to the energy flux of species s while $Q_{s,\text{pot}}$ corresponds to the flux due to the electric potential. For the numerical results presented in Fig. 13 the term $Q_{s,\text{pol}}$ is not taken into account. Indeed, it requires 3D values of U and $P_{s,\perp}$ which were not saved for this simulation because this possibility has been more recently implemented in the code. Analyzing recent non-linear flux-driven simulations where this computation is available shows that the assumption $Q_{s,\text{pot}} \approx 0$ is justified. Even in regimes where turbulence is well developed the term $Q_{s,\text{pot}}$ stays sufficiently small to have no impact on the local energy conservation law.

The numerical validation of Eq. (66) is performed on flux surface average quantities. The comparison between $\langle \partial_{\chi} (Q + Q_{\text{pot}} + Q_{\text{pol}}) \rangle_{\text{FS}}$ and $\langle (E_K + E_p) \rangle_{\text{FS}}$ seen in Fig. 13 (left) shows an agreement better than 15% at time $t = 20\,040 \Omega_{c0}^{-1}$. The separate contributions of each term given by Eqs. (67)–(71) are plotted at Fig. 13 (right) showing that this energy conservation derives from the compensation of different complex radial profiles.

5.4. Local toroidal momentum conservation

Formally, the derivation of a conservation law for toroidal angular momentum is very similar to that for energy in the previous section. The general idea is to multiply the conservative gyrokinetic equation (58) by an invariant of motion. For the energy, this invariant was the gyro-center Hamiltonian \bar{H}_s given by Eq. (61). For this conservation law, let us consider the gyrocenter toroidal canonical momentum P_{φ} defined as

$$P_{\varphi} = m_s u_{\varphi} - q_s \chi \quad (72)$$

with the definition $u_{\varphi} = (I/B)v_{G\parallel} = R^2 \mathbf{b} \cdot \nabla \varphi v_{G\parallel}$. P_{φ} is an exact invariant of the *unperturbed gyrocenter motion* described by the Hamiltonian $\bar{H}_{s,\text{eq}} = \frac{1}{2} m_s v_{G\parallel}^2 + \mu_s B + \bar{U}_{\text{eq}}$, which corresponds to collisionless motion in a fully axisymmetric system. \bar{U}_{eq} is the gyroaverage of the equilibrium electric potential U_{eq} independent on the toroidal angle. When axisymmetry is broken, which can occur for instance due to turbulence or magnetic field ripple, P_{φ} is no longer a motion invariant. In particular, when the electric potential becomes non-axisymmetric, the evolution of P_{φ} is governed by the equation $d_t P_{\varphi} = -q_s \partial \varphi \bar{U}$. This result can be obtained by using the expression of the gyrokinetic Poisson brackets in the gyro-center coordinates $[\cdot, \cdot]_{\text{GC}}$ (see [2], equation (150))

$$\begin{aligned} [X, Y]_{\text{GC}} &= \frac{\mathbf{B}_s^*}{m_s B_{\parallel s}^*} \cdot (\nabla X \partial_{v_{G\parallel}} Y - \partial_{v_{G\parallel}} X \nabla Y) \\ &\quad - \frac{\mathbf{b}}{q_s B_{\parallel s}^*} \cdot (\nabla X \times \nabla Y). \end{aligned} \quad (73)$$

From the definition of P_{φ} given by Eq. (72), φ define the local toroidal angular momentum as

$$\mathcal{L}_{\varphi} = \sum_{\text{species}} m_s \int d\tau^* u_{\varphi} \bar{F}_s. \quad (74)$$

Note that \mathcal{L}_{φ} is the momentum for *gyrocenters*, which differs from the particle momentum by terms of order $\mathcal{O}(\rho_s^2)$. As said before, in order to derive a local conservation equation for \mathcal{L}_{φ} , we multiply the conservative gyrokinetic equation (58) by P_{φ} and integrate over all variables other than χ , leading to

$$\int d\tau^* P_{\varphi} \frac{\partial \bar{F}_s}{\partial t} + \int d\tau^* P_{\varphi} \frac{1}{B_{\parallel s}^*} \nabla_{\mathbf{z}} \cdot (\mathbf{z} B_{\parallel s}^* \bar{F}_s) = \int d\tau^* P_{\varphi} \mathcal{C}(\bar{F}_s).$$

Using the conservation properties of the collision operator $\int d\tau^* P_{\varphi} \mathcal{C}(\bar{F}_s) = 0$ and integrating by parts the second term, then

$$\begin{aligned} \partial_t \left(\int d\tau^* P_{\varphi} \bar{F}_s \right) &- \int d\tau^* \bar{F}_s \frac{\partial P_{\varphi}}{\partial t} - \int d\tau^* \bar{F}_s \frac{1}{B_{\parallel s}^*} \nabla_{\mathbf{z}} \cdot (\mathbf{z} B_{\parallel s}^* P_{\varphi}) \\ &+ \partial_{\chi} \int d\tau^* (\mathbf{z} \cdot \nabla \chi) \bar{F}_s P_{\varphi} = 0. \end{aligned}$$

Finally, using the fact that $d_t P_{\varphi} = -q_s \partial \varphi \bar{U}$, we obtain for each species s ,

$$\begin{aligned} m_s \partial_t \int d\tau^* u_{\varphi} \bar{F}_s - q_s \int d\tau^* \chi \partial_t \bar{F}_s + q_s \int d\tau^* \bar{F}_s \partial_{\varphi} \bar{U} \\ + \partial_{\chi} \int d\tau^* (\mathbf{z} \cdot \nabla \chi) \bar{F}_s P_{\varphi} = 0. \end{aligned} \quad (75)$$

Summing over all species, this leads to

$$\begin{aligned} & \partial_t \left(\sum_s m_s \int d\tau^* u_\varphi \bar{F}_s \right) - \chi \sum_s q_s \int d\tau^* \partial_t \bar{F}_s \\ & + \sum_s q_s \int d\tau^* \bar{F}_s \partial_\varphi \bar{U} + \partial_\chi \left(\sum_s m_s \int d\tau^* (\hat{\mathbf{z}} \cdot \nabla \chi) \bar{F}_s u_\varphi \right) \\ & - \partial_\chi \left(q_s \sum_s \chi \int d\tau^* (\hat{\mathbf{z}} \cdot \nabla \chi) \bar{F}_s \right) = 0. \end{aligned}$$

Using the local particle conservation equation (59), the second term can be written as $\chi \partial_\chi J^\chi$. We also identify the last term as $-\partial_\chi (\chi J^\chi)$. Then the conservation equation of the local toroidal momentum $\mathcal{L}_\varphi = \sum_s m_s \int d\tau^* u_\varphi \bar{F}_s$ reads

$$\partial_t \mathcal{L}_\varphi + \partial_\chi \Pi_\varphi^\chi + T_{\text{pol}}^\chi = J^\chi \quad (76)$$

where

$$\begin{aligned} \Pi_\varphi^\chi &= \sum_{\text{species}} m_s \int d\tau^* \bar{F}_s u_\varphi v_G^\chi; & T_{\text{pol}}^\chi &= \sum_{\text{species}} q_s \int d\tau^* \bar{F}_s \partial_\varphi \bar{U}; \\ J^\chi &= \sum_{\text{species}} q_s \int d\tau^* v_G^\chi \bar{F}_s. \end{aligned}$$

Eq. (76) is an *exact* equation for the transport of gyrocenter toroidal momentum, in the sense that it was obtained directly from the gyrokinetic model, with no specific assumptions regarding the ordering. The term T_{pol}^χ corresponds to a polarization flux of momentum term.

The numerical results obtained with the code are presented in Fig. 14 with the contribution of the different terms of Eq. (76) (at the right) averaged on the flux surface. The relative error plotted at the middle shows an accuracy better than 10%.

6. Conclusion

A complete description of the multi-ion species version of the 5D non-linear gyrokinetic code GYSELA has been presented. Adding to its global full- f character its original semi-Lagrangian scheme, the GYSELA code is unique. It can tackle the complex problem of ion turbulence self-organization (in adiabatic electrons and electrostatic limits), a special care having been taken to fully consistently model the interplay between turbulence and collisions as well as the interplay between all possible scales in the problem, with no assumption of scale separation. Code verification has been successfully performed with a permanent concern for improving its reliability, namely (i) comparison with analytical theory; (ii) benchmarks with other gyrokinetic codes; (iii) invariance tests to check the correct implementation of mass and charge parameters; and (iv) conservation law properties of the semi-Lagrangian method. Particular attention was recently paid to ensure the traceability of the code for the two main developments under progress; the implementation of kinetic electrons and taking into account of a more realistic magnetic configuration. The code is scalable up to actual parallel machine sizes.

Acknowledgments

The authors acknowledge the fruitful and lively discussions held during the Festival de Théorie in Aix-en-Provence. This work was supported by ANR grant GYPSI ANR-10-BLAN-941 and G8-Exascale action NuFUSE project. The simulations were performed not only with national HPC resources of CCRT, CINES and IDRIS under GENCI (Grand Equipement National de Calcul Intensif) allocations but also with Helios/IFERC machine dedicated

to Fusion at Rokkasho in Japan and with PRACE (Partnership for Advanced Computing in Europe) Research infrastructure. This work, supported by the European Communities under the contract of Association between EURATOM and CEA, was carried out within the framework of the European Fusion Development Agreement. The views and opinions expressed herein do not necessarily reflect those of the European Commission. One of the authors (D.Z.) is supported by the A*MIDEX project (no. ANR-11-IDEX-0001-02) funded by the ‘‘Investissements d’Avenir’’ French Government program, managed by the French National Research Agency (ANR).

Appendix A. How to overcome the difficulty due to $\langle \hat{\phi} \rangle_{\text{FS}}$ term in the quasi-neutrality solver?

In this appendix, the numerical solving of the quasi-neutrality equation is described. This description is based on the normalized quasi-neutrality equation implemented in the code

$$\begin{aligned} & -\frac{1}{\hat{n}_{e0}} \sum_s \hat{A}_s \hat{\nabla}_\perp \cdot (\hat{n}_{s0} \hat{\nabla}_\perp \hat{\phi}) + \frac{1}{Z_0^2 \hat{T}_e} [\hat{\phi} - \lambda \langle \hat{\phi} \rangle_{\text{FS}}] \\ & = \frac{1}{\hat{n}_{e0}} \sum_s \hat{Z}_s [\hat{n}_{G_s} - \hat{n}_{G_s,eq}]. \end{aligned} \quad (A.1)$$

It explains the particular treatment performed to overcome the problem of the flux surface average term $\langle \cdot \rangle_{\text{FS}}$ in Fourier space. The previous Eq. (D.8) can be written as

$$\mathcal{L} \hat{\phi} + \frac{1}{Z_0^2 \hat{T}_e(\hat{r})} [\hat{\phi} - \lambda \langle \hat{\phi} \rangle_{\text{FS}}] = \rho(\hat{r}, \theta, \varphi) \quad (A.2)$$

where the differential operator of second order \mathcal{L} is defined as

$$\begin{aligned} \mathcal{L} &= -\frac{1}{\hat{n}_{e0}(\hat{r})} \sum_s \hat{A}_s \hat{n}_{s0}(\hat{r}) \\ & \times \left\{ \frac{\partial^2}{\partial \hat{r}^2} + \left[\frac{1}{\hat{r}} + \frac{1}{\hat{n}_{s0}(\hat{r})} \frac{d\hat{n}_{s0}(\hat{r})}{dr} \right] \frac{\partial}{\partial \hat{r}} + \frac{1}{\hat{r}^2} \frac{\partial^2}{\partial \theta^2} \right\} \end{aligned}$$

and the right hand side reads

$$\rho(\hat{r}, \theta, \varphi) = \frac{1}{\hat{n}_{e0}(\hat{r})} \sum_s Z_s [\hat{n}_{G_s}(\hat{r}, \theta, \varphi) - \hat{n}_{G_s,eq}(\hat{r}, \theta)].$$

The constant λ can be chosen equal to 1 (by default) or equal to 0. Let for all function g , $\langle g \rangle_{\theta, \varphi}$ being the radial function equal to

$$\langle g(\hat{r}) \rangle_{\theta, \varphi} = \frac{1}{L_\theta L_\varphi} \int \int g(\hat{r}, \theta, \varphi) d\theta d\varphi.$$

By applying the integration $\frac{1}{L_\theta L_\varphi} \int \int \cdot d\theta d\varphi$ to the previous Eq. (A.2) and by using the fact that $\langle \langle \hat{\phi} \rangle_{\theta, \varphi} \rangle_{\text{FS}} = \langle \hat{\phi} \rangle_{\theta, \varphi}$ then:

$$\mathcal{L} \langle \hat{\phi} \rangle_{\theta, \varphi} + \frac{1}{Z_0^2 \hat{T}_e} [\langle \hat{\phi} \rangle_{\theta, \varphi} - \lambda \langle \hat{\phi} \rangle_{\text{FS}}] = \langle \rho \rangle_{\theta, \varphi}. \quad (A.3)$$

Let $\hat{\phi}$ being $\hat{\phi} = \hat{\phi} - \langle \hat{\phi} \rangle_{\theta, \varphi}$ then, by subtracting (A.3) to (A.2), and by using Dirichlet boundary conditions we obtain $\forall \lambda \in \mathbb{R}$, $\forall \theta \in [0, L_\theta]$ and $\forall \varphi \in [0, L_\varphi]$:

$$\begin{cases} \left(\mathcal{L} + \frac{1}{Z_0^2 \hat{T}_e} \right) \hat{\phi}(\hat{r}, \theta, \varphi) = \varrho(\hat{r}, \theta, \varphi) \\ \text{with } \varrho = \rho - \langle \rho \rangle_{\theta, \varphi} \quad \forall \hat{r} \in [\hat{r}_{\text{min}}, \hat{r}_{\text{max}}] \\ \hat{\phi}(\hat{r}_{\text{min}}, \theta, \varphi) = \hat{\phi}(\hat{r}_{\text{max}}, \theta, \varphi) = 0. \end{cases} \quad (A.4)$$

Besides, (A.3) can be written as

$$\begin{aligned} & \mathcal{L} \left(\langle \hat{\phi} \rangle_{\theta, \varphi} - \langle \hat{\phi} \rangle_{\text{FS}} \right) + \mathcal{L} \langle \hat{\phi} \rangle_{\text{FS}} \\ & + \frac{1}{Z_0^2 \hat{T}_e} \left[\left(\langle \hat{\phi} \rangle_{\theta, \varphi} - \langle \hat{\phi} \rangle_{\text{FS}} \right) + \langle \hat{\phi} \rangle_{\text{FS}} - \lambda \langle \hat{\phi} \rangle_{\text{FS}} \right] = \langle \rho \rangle_{\theta, \varphi}. \end{aligned}$$

Then using the fact that $\langle \hat{\phi} \rangle_{\text{FS}} = \langle \hat{\phi} \rangle_{\text{FS}} - \langle \langle \hat{\phi} \rangle_{\theta, \varphi} \rangle_{\text{FS}}$ and using Dirichlet boundary conditions, the previous equation leads to the following system:

$$\begin{cases} \left(\mathcal{L} + (1 - \lambda) \frac{1}{Z_0^2 \hat{T}_e} \right) \langle \hat{\phi} \rangle_{\text{FS}} \\ = \langle \rho \rangle_{\theta, \varphi} + \left(\mathcal{L} + \frac{1}{Z_0^2 \hat{T}_e} \right) \langle \hat{\phi} \rangle_{\text{FS}} \\ \langle \hat{\phi} \rangle_{\text{FS}}(\hat{r}_{\min}) = \langle \hat{\phi} \rangle_{\text{FS}}(\hat{r}_{\max}) = 0. \end{cases} \quad (\text{A.5})$$

Using the definition of $\hat{\phi}$, then

$$\begin{aligned} \langle \hat{\phi} \rangle_{\text{FS}} &= \langle \hat{\phi} \rangle_{\text{FS}} - \langle \langle \hat{\phi} \rangle_{\theta, \varphi} \rangle_{\text{FS}} \\ &= \langle \hat{\phi} \rangle_{\text{FS}} - \langle \hat{\phi} \rangle_{\theta, \varphi} \quad (\text{because } \langle \langle \hat{\phi} \rangle_{\theta, \varphi} \rangle_{\text{FS}} = \langle \hat{\phi} \rangle_{\theta, \varphi}) \end{aligned}$$

so $\langle \hat{\phi} \rangle_{\theta, \varphi} = \langle \hat{\phi} \rangle_{\text{FS}} - \langle \hat{\phi} \rangle_{\text{FS}}$

and using the fact that $\hat{\phi} = \hat{\phi} + \langle \hat{\phi} \rangle_{\theta, \varphi}$, we obtain the expression of the electric potential $\hat{\phi}$ as:

$$\hat{\phi}(\hat{r}, \theta, \varphi) = \hat{\phi}(\hat{r}, \theta, \varphi) - \langle \hat{\phi} \rangle_{\text{FS}}(\hat{r}) + \langle \hat{\phi} \rangle_{\text{FS}}(\hat{r}). \quad (\text{A.6})$$

To summarize, the solving of Eq. (D.8) can be replaced by the solving of two simpler Eqs. (A.4) and (A.5). Indeed, Eq. (A.5) is a differential equation only depending on the radial direction. Besides, in (A.4) the variable φ plays the role of a parameter, then the discretization of the equation can be performed by projecting in Fourier space in θ direction and by using finite differences in the radial direction as described in the following paragraph. However, it is important to realize that the boundary conditions are not directly applied on $\hat{\phi}$ but on $\hat{\phi} = \hat{\phi} - \langle \hat{\phi} \rangle_{\theta, \varphi}$. So the fact to impose $\hat{\phi}(\hat{r}_{\min}) = 0$ does not imply $\hat{\phi}(\hat{r}_{\min}) = 0$ but $\hat{\phi}(\hat{r}_{\min}) = \langle \hat{\phi} \rangle_{\theta, \varphi}(\hat{r}_{\min})$ (same remark can be done at $\hat{r} = \hat{r}_{\max}$). Another treatment is available when \hat{r}_{\min} is sufficiently close to 0 ($\hat{r}_{\min} < 10^{-2}$ in the code). Indeed, let us assume that in this case $J_x(\hat{r}_{\min}, \theta)$ is equal to a constant. Then, for all function g ,

$$\langle g \rangle_{\text{FS}}(\hat{r}_{\min}) = \frac{\int g J_x(\hat{r}_{\min}, \theta) d\theta d\varphi}{\int J_x(\hat{r}_{\min}, \theta) d\theta d\varphi} = \frac{1}{4\pi} \langle g \rangle_{\theta, \varphi} \quad \forall |\hat{r}_{\min}| \ll 1.$$

In this case employing a Neumann boundary condition on the (0, 0) mode at the axis (i.e. $\partial_r \langle \hat{\phi} \rangle_{\theta, \varphi}(\hat{r}_{\min}) = 0$) is equivalent to applying $\partial_r \langle \hat{\phi} \rangle_{\text{FS}}(\hat{r}_{\min}) = 0$ in the matrix system (A.5). Matrix systems (A.4) and (A.5) are both solved by using finite differences in radial direction and Fourier projection in θ direction. Fourier space is also used in ϕ direction for (A.5). Then the different steps for solving (A.2) and obtaining $\hat{\phi}$ are the following:

- (i) Compute and save ρ ,
- (ii) Solve (A.4) to obtain $\hat{\phi}$ and save the 3D array $\hat{\phi}$,
- (iii) Compute $\langle \hat{\phi} \rangle_{\text{FS}}$ and save this 1D array,
- (iv) Compute the RHS of (A.5), i.e. $\langle \rho \rangle_{\theta, \varphi} + \left(\mathcal{L} + \frac{1}{Z_0^2 \hat{T}_e} \right) \langle \hat{\phi} \rangle_{\text{FS}}$ and save this 1D array,
- (v) Solve (A.5) to obtain $\langle \hat{\phi} \rangle_{\text{FS}}$ and store it, and finally
- (vi) Compute $\hat{\phi}(\hat{r}, \theta, \varphi)$ by using (A.6).

Appendix B. Expressions for simplified collisional transfer between two species

B.1. Conservation properties of collisional energy transfer

Let us consider the energy exchange between two species defined by Eqs. (34)–(39), i.e. $d\bar{F}_s/dt = C_{ss'}^{\mathcal{E}}(\mathcal{E}_{ss'})$ and $d\bar{F}_{s'}/dt = C_{s's}^{\mathcal{E}}(\mathcal{E}_{s's})$ with

$$\begin{aligned} C_{ss'}^{\mathcal{E}}(\mathcal{E}_{ss'}) &\equiv -\frac{\eta_{ss'}^{\mathcal{E}}}{(2\pi T_{\text{mean}}/m_s)^{3/2}} \frac{\Delta T_{ss'}}{T_{\text{mean}}} \left(\frac{\mathcal{E}_{ss'}}{T_{\text{mean}}} - \frac{3}{2} \right) \\ &\quad \times \exp\left(-\frac{\mathcal{E}_{ss'}}{T_{\text{mean}}}\right) \\ C_{s's}^{\mathcal{E}}(\mathcal{E}_{s's}) &\equiv -\frac{\eta_{s's}^{\mathcal{E}}}{(2\pi T_{\text{mean}}/m_{s'})^{3/2}} \frac{\Delta T_{s's}}{T_{\text{mean}}} \left(\frac{\mathcal{E}_{s's}}{T_{\text{mean}}} - \frac{3}{2} \right) \\ &\quad \times \exp\left(-\frac{\mathcal{E}_{s's}}{T_{\text{mean}}}\right) \end{aligned}$$

with $\mathcal{E}_{ss'}$, $\mathcal{E}_{s's}$ defined by Eq. (38) and T_{mean} , $\Delta T_{ss'}$ defined by Eq. (36). Let us consider the brackets $\langle \cdot \rangle_{v,T}$ defined as

$$\begin{aligned} \langle \cdot \rangle_{v,T} &= \frac{1}{(2\pi T/m_s)^{3/2}} \\ &\quad \times \int \int \cdot \exp\left(-\frac{v^2}{2T} - \frac{\mu B}{T}\right) \frac{2\pi}{m_s} B_{\parallel s}^* d\mu_s dv. \end{aligned} \quad (\text{B.1})$$

Let us define $\bar{v}_{\parallel} = v_{G\parallel} - V_{\text{mean}}$. Then, using the fact that $\langle 1 \rangle_{\bar{v}_{\parallel}, T_{\text{mean}}} = 1$ and $\langle m_s \bar{v}_{\parallel}^2 \rangle_{\bar{v}_{\parallel}, T_{\text{mean}}} = \langle \mu_s B \rangle_{\bar{v}_{\parallel}, T_{\text{mean}}} = T_{\text{mean}}$, it is straightforward to show that such a collision operator conserves both particles and parallel momentum, i.e. that

$$\begin{aligned} \langle C_{ss'}^{\mathcal{E}}(\mathcal{E}_s) \rangle &= \langle C_{s's}^{\mathcal{E}}(\mathcal{E}_{s'}) \rangle = 0 \quad \text{and} \\ \langle v_{G\parallel} C_{ss'}^{\mathcal{E}}(\mathcal{E}_s) \rangle &+ \langle v_{G\parallel} C_{s's}^{\mathcal{E}}(\mathcal{E}_{s'}) \rangle = 0 \quad \text{where } \langle \cdot \rangle = \int \cdot d^3\mathbf{v}. \end{aligned}$$

The parameters $\eta_{ss'}^{\mathcal{E}}$ and $\eta_{s's}^{\mathcal{E}}$ are designed such that the collisional energy exchange between species satisfy $\langle \mathcal{E}_s C_{ss'}^{\mathcal{E}}(\mathcal{E}_s) \rangle = -\langle \mathcal{E}_{s'} C_{s's}^{\mathcal{E}}(\mathcal{E}_{s'}) \rangle$. So let us compute the following integral in velocity space,

$$\langle \mathcal{E}_s C_{ss'}^{\mathcal{E}} \rangle = \int \mathcal{E}_s C_{ss'}^{\mathcal{E}} d^3\mathbf{v} = -\eta_{ss'}^{\mathcal{E}} \frac{\Delta T_{ss'}}{T_{\text{mean}}} \left\langle \mathcal{E}_s \left(\frac{\mathcal{E}_{ss'}}{T_{\text{mean}}} - \frac{3}{2} \right) \right\rangle_{\bar{v}_{\parallel}, T_{\text{mean}}}$$

which is equivalent to $\langle \mathcal{E}_s C_{ss'}^{\mathcal{E}} \rangle = -\eta_{ss'}^{\mathcal{E}} (\Delta T_{ss'}/T_{\text{mean}}) \mathcal{I}$, where

$$\begin{aligned} \mathcal{I} &= \left\langle \left(m_s \frac{\bar{v}_{\parallel}^2}{2} + m_s \frac{(V_{\parallel s}^2 - V_{\text{mean}}^2)}{2} \right) \right. \\ &\quad \left. - m_s (\bar{v}_{\parallel} + V_{\text{mean}}) \frac{\Delta V_{ss'}}{2} + \mu_s B \right\rangle_{\bar{v}_{\parallel}, T_{\text{mean}}} \\ &\quad \times \left\langle \left(\frac{1}{2} m_s \frac{\bar{v}_{\parallel}^2}{T_{\text{mean}}} + \frac{\mu_s B}{T_{\text{mean}}} - \frac{3}{2} \right) \right\rangle_{\bar{v}_{\parallel}, T_{\text{mean}}} \\ &= \left\langle \left(m_s \frac{\bar{v}_{\parallel}^2}{2} - m_s \frac{\Delta V_{ss'}}{2} \bar{v}_{\parallel} + m_s \frac{\Delta V_{ss'}^2}{8} + \mu_s B \right) \right. \\ &\quad \left. \times \left(\frac{1}{2} m_s \frac{\bar{v}_{\parallel}^2}{T_{\text{mean}}} + \frac{\mu_s B}{T_{\text{mean}}} - \frac{3}{2} \right) \right\rangle_{\bar{v}_{\parallel}, T_{\text{mean}}} \\ &= \left\langle \frac{m_s^2 \bar{v}_{\parallel}^4}{4T_{\text{mean}}} + \left(m_s \frac{\bar{v}_{\parallel}^2}{2} + \mu_s B \right) \left(m_s \frac{\Delta V_{s's}^2}{8T_{\text{mean}}} - \frac{3}{2} \right) \right. \\ &\quad \left. + \frac{m_s \bar{v}_{\parallel}^2 \mu_s B}{T_{\text{mean}}} + \frac{\mu_s^2 B^2}{T_{\text{mean}}} - m_s \Delta V_{ss'} \frac{3}{16} \right\rangle_{\bar{v}_{\parallel}, T_{\text{mean}}}. \end{aligned}$$

Then, using the properties, $\langle m_s^2 \bar{v}_{\parallel}^4 \rangle_{\bar{v}_{\parallel}, T_{\text{mean}}} = 3T_{\text{mean}}^2$ and $\langle \mu_s^2 B^2 \rangle_{\bar{v}_{\parallel}, T_{\text{mean}}} = 2T_{\text{mean}}^2$ and $\langle m_s \bar{v}_{\parallel}^2 \mu_s B \rangle_{\bar{v}_{\parallel}, T_{\text{mean}}} = T_{\text{mean}}^2$, the collisional energy exchange between species occurs at the following rate

$$\langle \mathcal{E}_s C_{ss'}^{\mathcal{E}} \rangle = -\eta_{ss'}^{\mathcal{E}} \frac{3\Delta T_{ss'}}{2} \left(1 - \frac{\Delta V_{ss'}^2}{8T_{\text{mean}}} \right). \quad (\text{B.2})$$

Let us use the property that the energy exchange term between two species is of the form (cf. [65], p. 184)

$$W_{ss'} = -\frac{4}{\sqrt{\pi}} \frac{\gamma_{ss'} n_s n_{s'} (T_s - T_{s'})}{m_{s'} (v_{T_s}^2 + v_{T_{s'}}^2)^{3/2}} \equiv \int d^3\mathbf{v} \frac{1}{2} m_s v^2 C_{ss'}$$

with $\gamma_{ss'} \sim \frac{m_s v_{T_s} v_{T_{s'}}^2}{n_{s'}} \nu_{ss'}$

where $v_{T_{>}} = \max(v_{T_s}, v_{T_{s'}})$ and the collision frequency $\nu_{ss'}$ is deduced from the ion-ion collision frequency ν_{ss} as

$$\nu_{ss'} = \left(\frac{Z_{s'}}{Z_s} \right)^2 \frac{n_{s'} v_{T_s}}{n_s v_{T_{>}}} \nu_{ss} \quad \text{and} \quad \nu_{ss} = \frac{\varepsilon^{3/2}}{qR_0} \left(\frac{T_{s,\text{coll}}}{m_s} \right)^{1/2} \nu_{*s}. \quad (\text{B.3})$$

Therefore

$$W_{ss'} = -\frac{4}{\sqrt{\pi}} \nu_{ss'} \frac{v_{T_{>}}}{v_{T_s}} n_s \frac{m_s}{m_{s'}} \Delta T_{ss'} \left(1 + \frac{v_{T_{s'}}^2}{v_{T_s}^2} \right)^{-3/2}. \quad (\text{B.4})$$

Finally, by analogy between (B.2) and Eq. (B.4) (considering $\Delta V_{ss'}^2/8T_{\text{mean}} \ll 1$), this provides for the effective collision frequency $\eta_{ss'}^{\mathcal{E}}$ the following expression,

$$\eta_{ss'}^{\mathcal{E}} = \frac{8 \varepsilon^{3/2}}{3\sqrt{\pi}} n_{s'} \frac{m_s}{m_{s'}} \left(\frac{Z_{s'}}{Z_s} \right)^2 \left(1 + \frac{v_{T_{s'}}^2}{v_{T_s}^2} \right)^{-3/2} \frac{\sqrt{T_{s,\text{coll}}/m_s}}{qR_0} \nu_{*s}$$

which is equivalent to the one given by Eq. (39).

B.2. Conservation properties of collisional parallel momentum transfer

Let us consider the parallel momentum transfer defined by Eqs. (40)–(42), i.e $d\bar{F}_s/dt = C_{ss'}^{v_{G\parallel}}(E_s)$ and $d\bar{F}_{s'}/dt = C_{s's}^{v_{G\parallel}}(E_{s'})$ with

$$C_{ss'}^{v_{G\parallel}}(E_s) \equiv -\eta_{ss'}^{v_{G\parallel}} \Delta V_{ss'} v_{G\parallel} \exp\left(-\frac{E_s}{T_{\text{mean}}}\right) \quad \text{and}$$

$$C_{s's}^{v_{G\parallel}}(E_{s'}) \equiv -\eta_{s's}^{v_{G\parallel}} \Delta V_{s's} v_{G\parallel} \exp\left(-\frac{E_{s'}}{T_{\text{mean}}}\right).$$

Considering this approximation, the momentum exchanges between two species reads¹¹

$$\langle m_s v_{G\parallel} C_{ss'}^{v_{G\parallel}}(E_s) \rangle = \int d^3\mathbf{v} m_s v_{G\parallel} \frac{d\bar{F}_s}{dt} = -\eta_{ss'}^{v_{G\parallel}} \Delta V_{ss'} \left(\frac{2\pi}{m_s} \right)^{3/2} T_{\text{mean}}^{5/2} \quad (\text{B.5})$$

$$\langle m_s v_{G\parallel} C_{s's}^{v_{G\parallel}}(E_{s'}) \rangle = \int d^3\mathbf{v} m_{s'} v_{G\parallel} \frac{d\bar{F}_{s'}}{dt} - \eta_{s's}^{v_{G\parallel}} \Delta V_{s's} \left(\frac{2\pi}{m_{s'}} \right)^{3/2} T_{\text{mean}}^{5/2}. \quad (\text{B.6})$$

¹¹ $\langle m_s v_{G\parallel} C_{ss'}^{v_{G\parallel}} \rangle = -\eta_{ss'}^{v_{G\parallel}} \Delta V_{ss'} \left(\frac{2\pi T_{\text{mean}}}{m_s} \right)^{3/2} \langle m_s v_{G\parallel}^2 \rangle_{v_{G\parallel}, T_{\text{mean}}} = -\eta_{ss'}^{v_{G\parallel}} \Delta V_{ss'} \left(\frac{2\pi T_{\text{mean}}}{m_s} \right)^{3/2} T_{\text{mean}}$.

Therefore, the action-reaction principle $\langle m_s v_{G\parallel} C_{ss'}^{v_{G\parallel}} \rangle = -\langle m_s v_{G\parallel} C_{s's}^{v_{G\parallel}} \rangle$, leads to the first constraint $\eta_{s's}^{v_{G\parallel}} = (m_{s'}/m_s)^{3/2} \eta_{ss'}^{v_{G\parallel}}$. The second constraint comes from the neoclassical friction relation,

$$-\int d^3\mathbf{v} m_{s'} v_{G\parallel} \frac{d\bar{F}_{s'}}{dt} = m_s n_s \nu_{ss'} \Delta V_{ss'} = -m_{s'} n_{s'} \nu_{s's} \Delta V_{s's}$$

then using Eq. (B.5) leads to

$$\eta_{ss'}^{v_{G\parallel}} = m_s n_s \left(\frac{2\pi}{m_s} \right)^{-3/2} T_{\text{mean}}^{-5/2} \nu_{ss'}.$$

Finally, using the relation (B.3) for $\nu_{ss'}$ expression, $\eta_{ss'}^{v_{G\parallel}}$ can be expressed as

$$\eta_{ss'}^{v_{G\parallel}} = n_{s'} m_s^2 \left(\frac{\varepsilon}{2\pi} \right)^{3/2} \frac{1}{qR_0} \frac{\sqrt{T_{s,\text{coll}}}}{T_{\text{mean}}^{5/2}} \left(\frac{Z_{s'}}{Z_s} \right)^2 \frac{v_{T_s}}{v_{T_{>}}} \nu_{*s}$$

which is equivalent to Eq. (42).

Appendix C. Numerical treatment of the source terms

The source terms are taken into account by solving $d_t \bar{F}_s = S_{\mathcal{E}} + S_{v_{G\parallel}} + S_{\Omega} + S_n$ with $S_{\mathcal{E}}$ the energy source, $S_{v_{G\parallel}}$ the parallel momentum source, S_{Ω} the vorticity source and S_n the impurity source. For the following, let us use the fact that each source is of the form $S_E(r(t), \theta(t), v_{G\parallel}(t), \mu_s) S_r(r(t))$. For more readability let us consider one unique source knowing that the numerical method described below can be generalized to a sum of sources. Let us integrate in time between t and $t + \Delta t$ the equation

$$\frac{d\bar{F}_s}{dt}(r, \theta, \varphi, v_{G\parallel}, \mu) = S(t)$$

$$\text{with } S(t) = S_E(r(t), \theta(t), v_{G\parallel}(t), \mu_s) S_r(r(t))$$

then

$$\bar{F}_s(t + \Delta t) - \bar{F}_s(t) = \int_t^{t+\Delta t} S(t') dt'$$

$$\begin{aligned} S_r(r(t')) &= S_r(r(t + \Delta t)) + [r(t') - r(t + \Delta t)] \\ &\quad \times \frac{\partial S_r}{\partial r}(r(t + \Delta t)) + \mathcal{O}(\Delta t^2) \\ &= S_r(r(t + \Delta t)) + (t' - t - \Delta t) \frac{dr}{dt} \Big|_{t+\Delta t} \\ &\quad \times \frac{\partial S_r}{\partial r}(r(t + \Delta t)) + \mathcal{O}(\Delta t^2). \end{aligned}$$

Besides, let us define $S_E(t') = S_E(r(t'), \theta(t'), v_{G\parallel}(t'), \mu_s)$, then

$$\begin{aligned} S_E(t') &= S_E(r(t + \Delta t), \theta(t'), v_{G\parallel}(t'), \mu_s) \\ &\quad + (t' - t - \Delta t) \frac{dr}{dt} \Big|_{t+\Delta t} \frac{\partial S_E}{\partial r}(r(t + \Delta t), \theta(t'), v_{G\parallel}(t'), \mu_s) \\ &\quad + \mathcal{O}(\Delta t^2) \\ &\approx S_E(r(t + \Delta t), \theta(t + \Delta t), v_{G\parallel}(t + \Delta t), \mu_s) \\ &\quad + (t' - t - \Delta t) \left[\frac{dr}{dt} \Big|_{t+\Delta t} \frac{\partial S_E}{\partial r}(r(t + \Delta t), \theta(t + \Delta t), v_{G\parallel}(t + \Delta t), \mu_s) \right. \\ &\quad \left. + \Delta t, v_{G\parallel}(t + \Delta t), \mu_s) \right. \\ &\quad \left. + \frac{d\theta}{dt} \Big|_{t+\Delta t} \frac{\partial S_E}{\partial \theta}(r(t + \Delta t), \theta(t + \Delta t), v_{G\parallel}(t + \Delta t), \mu_s) \right. \\ &\quad \left. + \frac{dv_{G\parallel}}{dt} \Big|_{t+\Delta t} \frac{\partial S_E}{\partial v_{G\parallel}}(r(t + \Delta t), \theta(t + \Delta t), v_{G\parallel}(t + \Delta t), \mu_s) \right] \\ &\quad + \mathcal{O}(\Delta t^2). \end{aligned}$$

Table D.12

Links between physical and normalized quantities.

$\begin{aligned} m_s &= m_0 \hat{A}_s \\ q_s &= Z_0 e \hat{Z}_s \\ l &= \rho_0 \hat{l} \\ t &= \hat{t} / \Omega_{c_0} \\ n_s &= n_0 \hat{n}_s \\ T_s &= T_0 \hat{T}_s \\ B &= B_0 \hat{B} \end{aligned}$	⇒	$\begin{aligned} v_{G\parallel} &= v_{T_{s0}} \hat{v}_{G\parallel s} \\ &= (v_{T_0} / \sqrt{\hat{A}_s}) \hat{v}_{G\parallel s} \\ v_{E \times B_s} &= v_{T_0} \hat{v}_{E \times B_s} \\ v_{D_s} &= v_{T_0} \hat{v}_{D_s} \\ \mu_s &= (T_0 / B_0) \hat{\mu}_s \\ U &= [T_0 / (Z_0 e)] \hat{\phi} \\ E &= (v_{T_0} B_0) \hat{E} \\ F_s &= (n_0 / v_{T_{s0}}^3) \hat{F}_s \end{aligned}$	and	$\begin{aligned} \chi &= \rho_0^2 \Omega_{c_0} \hat{\chi} \\ \nu &= \Omega_{c_0} \hat{\nu} \\ \mathcal{D}_{\parallel s} &= v_{T_{s0}}^2 \Omega_{c_0} \hat{\mathcal{D}}_{\parallel s} \\ \mathcal{V}_{\parallel s} &= v_{T_{s0}} \Omega_{c_0} \hat{\mathcal{V}}_{\parallel s} \\ S_0^\mathcal{E} &= n_0 \Omega_{c_0} T_0 \hat{S}_0^\mathcal{E} \\ S_0^{v_{G\parallel}} &= n_0 \Omega_{c_0} v_{T_{s0}} \hat{S}_0^{v_{G\parallel}} \\ S_0^\Omega &= \frac{n_0 \Omega_{c_0}}{\rho_0^2} \hat{S}_0^\Omega \end{aligned}$
--	---	---	-----	--

Therefore, the distribution function \bar{F}_s at time $t + \Delta t$ is given at second order in time by

$$\begin{aligned} \bar{F}_s(t + \Delta t) &= \bar{F}_s(t) + \Delta t S_E(t + \Delta t) S_r(t + \Delta t) \\ &\quad - \frac{\Delta t^2}{2} \left[S_E(t + \Delta t) \frac{dr}{dt} \Big|_{t+\Delta t} \frac{\partial S_r}{\partial r} \Big|_{t+\Delta t} \right. \\ &\quad + S_r(t + \Delta t) \left(\frac{dr}{dt} \Big|_{t+\Delta t} \frac{\partial S_E}{\partial r} \Big|_{t+\Delta t} \right. \\ &\quad \left. \left. + \frac{d\theta}{dt} \Big|_{t+\Delta t} \frac{\partial S_E}{\partial \theta} \Big|_{t+\Delta t} + \frac{dv_{G\parallel}}{dt} \Big|_{t+\Delta t} \frac{\partial S_E}{\partial v_{G\parallel}} \Big|_{t+\Delta t} \right) \right]. \end{aligned}$$

In the code, the radial derivatives of the sources of: (i) energy $\partial_r S_E$, (ii) momentum $\partial_r v_{G\parallel}$, (iii) vorticity $\partial_r S_\Omega$ and (iv) density $\partial_r S_n$ are computed numerically as well as the poloidal derivatives. On the other hand, the derivatives in $v_{G\parallel}$ direction are expressed analytically.

Appendix D. GYSELA normalized equations

This appendix contains the expression of all the normalized quantities and normalized equations implemented in the code GYSELA.

D.1. GYSELA normalization

Let consider $m_0 = A_0 m_p$ (kilograms) a reference ionic mass, $q_0 = Z_0 e$ (Coulombs) a reference ionic charge, B_0 (Tesla) a reference magnetic induction and T_0 (electron volts) a reference temperature. A_0 and Z_0 are the (dimensionless) mass number and charge state of the principal ionic species and e the modulus of the electron charge. These quantities are used to define the reference ion cyclotron frequency Ω_{c_0} , the reference thermal speed v_{T_0} and the reference Larmor-radius ρ_0 as:

$$\Omega_{c_0} = \frac{Z_0 e B_0}{m_0}; \quad v_{T_0} = \sqrt{\frac{T_0}{m_0}}; \quad \rho_0 = \frac{v_{T_0}}{\Omega_{c_0}} = \frac{\sqrt{T_0 m_0}}{Z_0 e B_0}. \quad (\text{D.1})$$

Actually, the seven normalizing quantities ($A_0, Z_0, n_0, T_0, B_0, a, R_0$) are not completely free. Three dimensionless parameters are further specified in the input data, which provide relationships between these seven parameters. These are the aspect ratio $A = R_0/a$, rhostar $\rho_{*0} = \sqrt{A_0 m_p T_0} / Z_0 e B_0$ and nustar $\nu_{*0} = \varepsilon^{-3/2} (q R_0 / v_{T_0}) \nu_{coll,0} \sim Z_0^4 n_0 R_0 / T_0^2$ (where ε and q are taken at $r_{\text{peak}} = r_{\text{min}} + 0.5(r_{\text{max}} - r_{\text{min}})$). It follows that, given A, ρ_{*0} and ν_{*0} , it remains only four free normalizing quantities. Hereafter, \hat{X} refers to the dimensionless expression of the X quantity. The normalizations used in the code are summarized in Table D.12.

Notice that the parallel velocity is normalized to $v_{T_{s0}}$ while all drift velocities are normalized to v_{T_0} . The normalized system of equations is made of the 5D gyrokinetic equation (including source terms and collisions) self-consistently coupled to the 3D quasi-neutrality. The gyrokinetic equation involves Poisson brackets

$[\cdot, \cdot]$. Introducing the unit vector $\mathbf{b} = \mathbf{B}/\|\mathbf{B}\|$ along the magnetic field, its covariant components b_k , and the Jacobian J_x of the configuration space, these brackets read as follows:

$$[F, G] = \mathbf{b} \cdot (\nabla F \times \nabla G) = J_x^{-1} \epsilon^{ijk} \partial_i F \partial_j G b_k. \quad (\text{D.2})$$

D.2. Normalized Boltzmann equation

The evolution of the guiding-center distribution function \hat{F}_s is governed by the following normalized Boltzmann equation:

$$\begin{aligned} \frac{d\hat{F}_s}{d\hat{t}} + \frac{1}{\hat{B}_{\parallel s}^*} \hat{\nabla} \cdot \left(\hat{B}_{\parallel s}^* \frac{d\hat{\mathbf{x}}_G}{d\hat{t}} \hat{F}_s \right) + \frac{1}{\hat{B}_{\parallel s}^*} \frac{\partial}{\partial \hat{v}_{G\parallel s}} \left(\hat{B}_{\parallel s}^* \frac{d\hat{v}_{G\parallel s}}{d\hat{t}} \hat{F}_s \right) \\ = \hat{\mathcal{D}}_r(\hat{F}_s) + \hat{\mathcal{K}}(\hat{F}_s) + \hat{\mathcal{C}}(\hat{F}_s) + \hat{\mathcal{S}} \end{aligned} \quad (\text{D.3})$$

where $\hat{\mathcal{D}}_r$ and $\hat{\mathcal{K}}$ are respectively a diffusion term and a Krook operator applied on a radial buffer region (see Appendix D.4), while $\hat{\mathcal{C}}$ refers to a collision operator (see Appendix D.5) and $\hat{\mathcal{S}}$ corresponds to source terms (see Appendix A in [53] for detailed expressions). The evolution of the gyro-center coordinates $(\mathbf{x}_G, v_{G\parallel}, \mu_s)$ of species s is given by:

$$\frac{d\hat{\mathbf{x}}_G^i}{d\hat{t}} = \frac{1}{\sqrt{\hat{A}_s}} \hat{v}_{G\parallel s} \hat{\mathbf{b}}_s^* \cdot \hat{\nabla} \mathbf{x}^i + \hat{\mathbf{v}}_{E \times B_s} \cdot \hat{\nabla} \mathbf{x}^i + \hat{\mathbf{v}}_{D_s} \cdot \hat{\nabla} \mathbf{x}^i \quad (\text{D.4})$$

$$\begin{aligned} \frac{d\hat{v}_{G\parallel s}}{d\hat{t}} &= -\frac{1}{\sqrt{\hat{A}_s}} \hat{\mu}_s \hat{\mathbf{b}}_s^* \cdot \hat{\nabla} \hat{B} - \frac{\hat{Z}_s}{\sqrt{\hat{A}_s}} \hat{\mathbf{b}}_s^* \cdot \hat{\nabla} \hat{\phi} \\ &\quad + K_{\nabla B} \hat{v}_{G\parallel s} \hat{\mathbf{v}}_{E \times B_s} \cdot \frac{\hat{\nabla} \hat{B}}{\hat{B}}. \end{aligned} \quad (\text{D.5})$$

The i th covariant coordinates of the normalized drift velocities are given by:

$$\hat{\mathbf{v}}_{E \times B_s} \cdot \hat{\nabla} \mathbf{x}^i = \hat{\mathbf{v}}_{E \times B_s}^i = \frac{1}{\hat{B}_{\parallel s}^*} \left[\hat{\phi}, \hat{\mathbf{x}}^i \right] \quad (\text{D.6})$$

$$\hat{\mathbf{v}}_{D_s} \cdot \hat{\nabla} \mathbf{x}^i = \hat{\mathbf{v}}_{D_s}^i = K_{\nabla B} \left(\frac{\hat{v}_{G\parallel s}^2 + \hat{\mu}_s \hat{B}}{\hat{Z}_s \hat{B}_{\parallel s}^* \hat{B}} \right) \left[\hat{B}, \hat{\mathbf{x}}^i \right] \quad (\text{D.7})$$

with $\hat{\mathbf{b}}_s^* = \frac{1}{\hat{B}_{\parallel s}^*} \left(\hat{\mathbf{B}} + \frac{\sqrt{\hat{A}_s}}{\hat{Z}_s} \frac{\hat{v}_{G\parallel s}}{\hat{B}} \hat{\mathbf{J}} \right)$ and $\hat{B}_{\parallel s}^* = \hat{B} + \frac{\sqrt{\hat{A}_s}}{\hat{Z}_s} \frac{\hat{v}_{G\parallel s}}{\hat{B}} \mathbf{b} \cdot \hat{\mathbf{J}}$. The

normalized magnetic field \hat{B} is defined as $\hat{B} = \frac{\hat{R}_0}{\hat{R}(r, \theta)} [\zeta(\hat{r}) \mathbf{e}_\theta + \mathbf{e}_\varphi]$

with $\zeta(\hat{r}) = \frac{\hat{r}}{q \hat{R}_0}$ while the normalized current reads $\hat{\mathbf{J}} = \hat{J}_r \hat{R} \hat{\nabla} \varphi$

with $\hat{J}_r = \frac{\hat{R}_0}{\hat{R}} \zeta \left(1 + \frac{\hat{r}}{\zeta} \frac{d\zeta}{d\hat{r}} - \frac{\hat{r}}{\hat{R}} \cos \theta \right)$. The constant $K_{\nabla B}$ has been added for tests in the code. $K_{\nabla B}$ is equal to 1 if the curvature of the magnetic field is taken into account and 0 otherwise. In equations (D.4) and (D.5) the parallel projection $\hat{\nabla}_{\parallel}^* F$ is computed as $\hat{\mathbf{b}}_s^* \cdot \hat{\nabla} F = \hat{b}^{*i} \hat{\partial}_i F$.

D.3. Normalized quasi-neutrality equation

The normalized quasi-neutrality equation is¹²:

$$\begin{aligned} & -\frac{1}{\hat{n}_{e0}} \sum_s \hat{A}_s \hat{V}_\perp \cdot \left(\frac{\hat{n}_{s0}}{\hat{B}} \hat{V}_\perp \hat{\phi} \right) + \frac{1}{Z_0^2 \hat{T}_e} \left[\hat{\phi} - \lambda \langle \hat{\phi} \rangle_{\text{FS}} \right] \\ & = \frac{1}{\hat{n}_{e0}} \sum_s \hat{Z}_s \left[\hat{n}_{G_s} - \hat{n}_{G_s,eq} \right] \end{aligned} \quad (\text{D.8})$$

where the normalized electron density \hat{n}_{e0} is defined as $\hat{n}_{e0} = \sum_s Z_0 \hat{Z}_s \hat{n}_{s0}$. Notice that, in the polarization term (first term of Eq. (D.8)), \hat{B} has been replaced by $\hat{B}_0 = 1$. The integral $\langle \hat{\phi} \rangle_{\text{FS}} = \int \hat{\phi} \hat{J}_x d\theta d\varphi / \int \hat{J}_x d\theta d\varphi$ represents the flux surface average of $\hat{\phi}$ (with $\hat{J}_x = 1/(\hat{B} \cdot \hat{V}\theta)$ being the normalized Jacobian space). The parameter λ has been added for tests. It can be chosen equal to 1 or 0. The normalized guiding-center density \hat{n}_{G_s} of species s is given by $\hat{n}_{G_s} = \int d\hat{\mu}_s \int \hat{V}_\perp d\hat{v}_{G\parallel s} \hat{J}_{0s} \cdot \hat{F}_s$ with the normalized Jacobian in velocity equal to $\hat{J}_v = 2\pi \hat{B}_{\parallel s}^* \cdot \hat{n}_{G_s,eq}$. $\hat{n}_{G_s,eq}$ is computed the same way, but from the initial equilibrium distribution function $\hat{F}_{s,eq} = c_s \frac{\hat{n}_{s0}}{(2\pi \hat{T}_s)^{3/2}} \exp\left[-\frac{(\hat{v}_{G\parallel s}^2/2 + \hat{\mu}_s \hat{B})}{\hat{T}_s}\right]$. The concentration c_s is such that $\sum_s c_s Z_0 \hat{Z}_s = 1$. The normalized gyroaverage operator \hat{J}_{0s} approximated by Padé corresponds to $\hat{J}_{0s} \approx 1 + \frac{1}{2} \frac{\hat{A}_s}{\hat{Z}_s^2} \frac{\hat{\mu}_s}{\hat{B}} \hat{V}_\perp^2$ where, as in the quasi-neutrality equation, \hat{B} is replaced by $\hat{B}_0 = 1$ in the code.

D.4. Normalized diffusion terms and Krook operator in buffer regions

A radial diffusion and an artificial damping are applied in buffer regions. These buffer regions are defined at each boundary of the radial domain $\hat{r} \in [\hat{r}_{\min}, \hat{r}_{\max}]$ as a sum of hyperbolic tangents:

$$\begin{aligned} \hat{H}_{\text{buff}}(\hat{r}) &= 1 + \frac{1}{2} \left[\tanh\left(\frac{\hat{r} - \hat{r}_{\max} + B_L \hat{L}_r}{B_S \hat{L}_r}\right) \right. \\ & \quad \left. - \tanh\left(\frac{\hat{r} - \hat{r}_{\min} - B_L \hat{L}_r}{B_S \hat{L}_r}\right) \right] \end{aligned} \quad (\text{D.9})$$

where \hat{L}_r is the normalized length of the radial domain. B_L and B_S are respectively the location and the stiffness of the buffer regions. The function \hat{H}_{buff} plays the role of a mask which is equal to 1 in the buffer regions and equal to 0 elsewhere.

¹² In the code, to avoid the expensive gyroaverage operation for each value of $v_{G\parallel}$ –which occur for the computation of the RHS of the quasi-neutrality equation (D.8)– we use the definition of $B_{\parallel s}^*$ and therefore the fact that the term $\hat{n}_{G_s} - \hat{n}_{G_s,eq}$ can be expressed as:

$$\begin{aligned} & \hat{n}_{G_s} - \hat{n}_{G_s,eq} \\ & = 2\pi \int d\hat{\mu}_s \left(\hat{B} \hat{J}_{0s} \cdot I_0(\hat{r}, \theta, \varphi, \hat{\mu}_s) + \frac{\sqrt{\hat{A}_s}}{\hat{Z}_s} \frac{\hat{v}_{G\parallel s}}{\hat{B}} \mathbf{b} \cdot \hat{J}_{0s} \cdot I_1(\hat{r}, \theta, \varphi, \hat{\mu}_s) \right) \end{aligned}$$

where the integrals I_0 and I_1 are defined by:

$$\begin{aligned} I_0(\hat{r}, \theta, \varphi, \hat{\mu}_s) &= \int (\hat{F}_s - \hat{F}_{s,eq}) d\hat{v}_{G\parallel s} \quad \text{and} \\ I_1(\hat{r}, \theta, \varphi, \hat{\mu}_s) &= \int \hat{v}_{G\parallel s} (\hat{F}_s - \hat{F}_{s,eq}) d\hat{v}_{G\parallel s}. \end{aligned}$$

A radial diffusion¹³ is applied on this buffer region by solving the following equation

$$\begin{aligned} \frac{\partial \hat{F}_s}{\partial \hat{t}} &= \hat{\mathcal{D}}_r(\hat{F}_s) \\ \text{with } \hat{\mathcal{D}}_r(\hat{F}_s) &= \frac{1}{\hat{r} \hat{B}_{\parallel s}^*} \frac{\partial}{\partial \hat{r}} \left(\hat{r} \hat{\chi}(\hat{r}) \frac{\partial}{\partial \hat{r}} \left(\hat{B}_{\parallel s}^* \hat{F}_s \right) \right) \end{aligned} \quad (\text{D.10})$$

where $\hat{\chi}(\hat{r}) = \hat{\chi}_0 \hat{H}_{\text{buff}}(\hat{r})$, where the normalized magnitude $\hat{\chi}_0$ of the diffusion coefficient in the buffer region is $\hat{\chi}_0 = \chi_0 / \rho_0^2 \Omega_{c0}$.

A Krook operator is applied by solving $\partial_t \hat{F}_s = \hat{\mathcal{K}}_r(\hat{F}_s)$ with $\hat{\mathcal{K}}_r(\hat{F}_s) = -\hat{v}(\hat{r})(\hat{F}_s - \hat{F}_{s,eq})$ where $\hat{v}(\hat{r}) = \hat{v}_0 \hat{H}_{\text{buff}}(\hat{r})$ such that $\hat{v}(\hat{r}) = v(r) / \Omega_{c0}$.

D.5. Normalized collision operator

A collision operator \mathcal{C}_s is present on the RHS of the normalized Vlasov equation (D.3), such that the normalized Boltzmann equation reads:

$$\begin{aligned} \frac{d\hat{F}_s}{d\hat{t}} &= \hat{\mathcal{C}}_s(\hat{F}_s) \\ \text{with } \hat{\mathcal{C}}_s(\hat{F}_s) &= \frac{1}{\hat{B}_{\parallel s}^*} \frac{\partial}{\partial \hat{v}_{G\parallel s}} \left[\hat{B}_{\parallel s}^* \left(\hat{\mathcal{D}}_{\parallel s} \frac{\partial \hat{F}_s}{\partial \hat{v}_{G\parallel s}} - \hat{V}_{\parallel s} \hat{F}_s \right) \right] \end{aligned} \quad (\text{D.11})$$

where the diffusion term $\hat{\mathcal{D}}_{\parallel s}$ and the drag term $\hat{V}_{\parallel s}$ in the parallel direction are defined as:

$$\begin{aligned} \hat{\mathcal{D}}_{\parallel s}(\hat{r}, \hat{v}) &= \hat{A}_s(\hat{r}) \left(\frac{\Phi(\hat{v}) - G(\hat{v})}{2\hat{v}} \right); \\ \hat{V}_{\parallel s}(\hat{r}, \hat{v}) &= -\frac{(\hat{v}_{G\parallel s} - \hat{V}_{\parallel s, \text{coll}})}{\hat{v}_{T_s, \text{coll}}^2} \hat{\mathcal{D}}_{\parallel s}(\hat{r}, \hat{v}) \end{aligned} \quad (\text{D.12})$$

where $\hat{v} = \sqrt{(\frac{1}{2} \hat{v}_{G\parallel s}^2 + \hat{\mu}_s \hat{B}_{\text{axis}})} / \hat{T}_{s, \text{coll}}$ while the Chandrasekhar function G is defined as $G(\hat{v}) = (\Phi(\hat{v}) - \hat{v} \Phi'(\hat{v})) / 2\hat{v}^2$ where $\Phi(\hat{v}) = \frac{2}{\sqrt{\pi}} \int_0^{\hat{v}} e^{-x^2} dx$ and $\Phi'(\hat{v}) = \frac{2}{\sqrt{\pi}} e^{-\hat{v}^2}$. The radial profile \hat{A}_s is given the form

$$\hat{A}_s(\hat{r}) = \frac{1}{\sqrt{\hat{A}_s}} \left(3 \frac{\sqrt{\pi}}{2} \frac{\hat{v}_{T_s, \text{coll}}^3 \epsilon^{3/2}}{q(\hat{r}) \hat{R}_0} \right) \hat{v}_{*s}. \quad (\text{D.13})$$

The normalized collisionality \hat{v}_{*s} is an input data. The normalized collisional frequency is then obtained as follows:

$$\hat{v}_{ss} = \frac{1}{\sqrt{\hat{A}_s}} \left(\frac{\hat{v}_{T_s, \text{coll}} \epsilon^{3/2}}{q(\hat{r}) \hat{R}_0} \right) \hat{v}_{*s}. \quad (\text{D.14})$$

Considering that the species s is the major ion species, the collisionality $\hat{v}_{*s'}$ of each minority ion species s' is determined by

$$\hat{v}_{*s'} = \left(\frac{\hat{n}_{s'}}{\hat{n}_s} \right) \left(\frac{\hat{Z}_{s'}}{\hat{Z}_s} \right)^4 \left(\frac{\hat{T}_{s, \text{coll}}}{\hat{T}_{s', \text{coll}}} \right)^2 \hat{v}_{*s}. \quad (\text{D.15})$$

¹³ In the code, there exists the possibility to apply the diffusion term to $(\hat{F}_s - \hat{F}_{s,eq})$ instead of \hat{F}_s .

In practice, $\hat{T}_{s,\text{coll}}/\hat{T}_{s',\text{coll}}$ is approximated by $\hat{T}_s/\hat{T}_{s'}$. The ratio $\hat{n}_{s'}/\hat{n}_s$ and $\hat{T}_{s,\text{coll}}/\hat{T}_{s',\text{coll}}$ are computed at the radial point \hat{r}_p which usually corresponds to the middle of the simulation radial domain. The normalized mean velocity $\hat{V}_{\parallel s,\text{coll}}$ and the normalized mean temperature $\hat{T}_{s,\text{coll}}$ can be calculated as $\hat{V}_{\parallel s,\text{coll}} = \hat{P}^{-1} (\hat{I}_4 \times \hat{I}_1 - \hat{I}_2 \times \hat{I}_3)$ and $\hat{T}_{s,\text{coll}} = \hat{P}^{-1} (\hat{I}_0 \times \hat{I}_2 - \hat{I}_1^2)$. The normalized mean pressure is defined by $\hat{P} = \hat{I}_0 \times \hat{I}_4 - \hat{I}_1 \times \hat{I}_3$ and where the five integrals $\hat{I}_0, \hat{I}_1, \hat{I}_2, \hat{I}_3$ and \hat{I}_4 are respectively: $\hat{I}_0 = \langle \hat{\mathcal{D}}_{\parallel s} \rangle$; $\hat{I}_1 = \langle \hat{\mathcal{D}}_{\parallel s} \hat{v}_{G\parallel s} \rangle$; $\hat{I}_2 = \langle \hat{\mathcal{D}}_{\parallel s} \hat{v}_{G\parallel s}^2 \rangle$; $\hat{I}_3 = \langle \frac{1}{\hat{B}_{\parallel s}^*} \partial_{\hat{v}_{G\parallel s}} (\hat{B}_{\parallel s}^* \hat{\mathcal{D}}_{\parallel s}) \rangle$ and $\hat{I}_4 = \langle \frac{1}{\hat{B}_{\parallel s}^*} \partial_{\hat{v}_{G\parallel s}} (\hat{B}_{\parallel s}^* \hat{v}_{G\parallel s} \hat{\mathcal{D}}_{\parallel s}) \rangle$ with the brackets $\langle \cdot \rangle = \int \cdot \hat{F}_s d\hat{v}_{G\parallel s} d\hat{\mu}_s$.

D.6. Normalized collisional transfers between two species

Normalized collisional energy transfer. Energy exchange between two species can be expressed by the following reduced collision operators:

$$\frac{d\hat{F}_s}{d\hat{t}} = -\frac{\hat{\eta}_{ss'}^e}{(2\pi \hat{T}_{\text{mean}})^{3/2} \hat{T}_{\text{mean}}} \Delta \hat{T}_{ss'} \left(\frac{\hat{\mathcal{E}}_{ss'}}{\hat{T}_{\text{mean}}} - \frac{3}{2} \right) \times \exp\left(-\frac{\hat{\mathcal{E}}_{ss'}}{\hat{T}_{\text{mean}}}\right) \quad (\text{D.16})$$

$$\frac{d\hat{F}_{s'}}{d\hat{t}} = -\frac{\hat{\eta}_{ss'}^e}{(2\pi \hat{T}_{\text{mean}})^{3/2} \hat{T}_{\text{mean}}} \Delta \hat{T}_{s's'} \left(\frac{\hat{\mathcal{E}}_{s's'}}{\hat{T}_{\text{mean}}} - \frac{3}{2} \right) \times \exp\left(-\frac{\hat{\mathcal{E}}_{s's'}}{\hat{T}_{\text{mean}}}\right) \quad (\text{D.17})$$

with $\hat{T}_{\text{mean}} = \frac{\hat{T}_s + \hat{T}_{s'}}{2}$; $\Delta \hat{T}_{ss'} = \hat{T}_s - \hat{T}_{s'} = -\Delta \hat{T}_{s's'}$; $\hat{V}_{\text{mean}} = \frac{\hat{V}_{\parallel s} + \hat{V}_{\parallel s'}}{2}$; $\hat{\mathcal{E}}_{ss'} = \frac{(\hat{v}_{G\parallel s} - \hat{V}_{\text{mean}})^2}{2} + \hat{\mu}_s \hat{B}$; $\hat{\mathcal{E}}_{s's'} = \frac{(\hat{v}_{G\parallel s'} - \hat{V}_{\text{mean}})^2}{2} + \hat{\mu}_{s'} \hat{B}$ and

$$\hat{\eta}_{ss'}^e(\hat{r}) = \frac{8 \hat{\mathcal{E}}^{3/2}}{3\sqrt{\pi}} \frac{\sqrt{\hat{A}_s}}{\hat{A}_{s'}} \left(\frac{\hat{Z}_{s'}}{\hat{Z}_s} \right)^2 \frac{\hat{n}_{s'} \sqrt{\langle \hat{T}_{s,\text{coll}} \rangle_{\text{FS}}}}{q\hat{R}_0} \times \left(1 + \frac{\hat{A}_s \hat{T}_{s'}}{\hat{A}_{s'} \hat{T}_s} \right)^{-3/2} \hat{v}_{*s}. \quad (\text{D.18})$$

Let us notice that in practice, the flux surface average of $\hat{T}_{s,\text{coll}}$ is used (compare to the general expression given by (42)), to consider only the radial dependency of $\hat{\eta}_{ss'}^e$. The normalized fluid moments $\hat{V}_{\parallel s}$ and \hat{T}_s are computed as $3\hat{T}_s(r)/2 = \langle \int \hat{\mathcal{E}}_s \hat{F}_s d^3\hat{\mathbf{v}} \rangle_{\text{FS}}/\hat{N}_s(r)$ and $\hat{V}_{\parallel s}(r) = \langle \int \hat{v}_{G\parallel s} \hat{F}_s d^3\hat{\mathbf{v}} \rangle_{\text{FS}}/\hat{N}_s(r)$ where $\hat{\mathcal{E}}_s$ is defined as $\hat{\mathcal{E}}_s = \frac{1}{2} (\hat{v}_{G\parallel s} - \hat{V}_{\parallel s})^2 + \hat{\mu}_s \hat{B}$ while $\hat{N}_s(r) = \langle \int \hat{F}_s d^3\hat{\mathbf{v}} \rangle_{\text{FS}}$.

Normalized collisional momentum transfer. Momentum exchange between two species can be expressed by the following reduced collision operator

$$\frac{d\hat{F}_s}{d\hat{t}} = -\hat{\eta}^{v_{G\parallel}} \hat{A}_s^{-1/2} \Delta \hat{V}_{ss'} \hat{v}_{G\parallel s} \exp\left(-\frac{\hat{E}_s}{\hat{T}_{\text{mean}}}\right) \quad (\text{D.19})$$

$$\frac{d\hat{F}_{s'}}{d\hat{t}} = -\hat{\eta}^{v_{G\parallel}} \hat{A}_{s'}^{-1/2} \Delta \hat{V}_{s's'} \hat{v}_{G\parallel s'} \exp\left(-\frac{\hat{E}_{s'}}{\hat{T}_{\text{mean}}}\right) \quad (\text{D.20})$$

with $\Delta \hat{V}_{ss'} = \hat{V}_{\parallel s} \hat{A}_s^{-1/2} - \hat{V}_{\parallel s'} \hat{A}_{s'}^{-1/2}$. The averages \hat{T}_{mean} and \hat{V}_{mean} have already been introduced. The energy \hat{E}_s is equal to $\frac{1}{2} \hat{v}_{G\parallel s}^2 + \hat{\mu}_s \hat{B}$. The radial profile $\hat{\eta}^{v_{G\parallel}}$ reads:

$$\hat{\eta}^{v_{G\parallel}}(r) = \left(\frac{\varepsilon}{2\pi} \right)^{3/2} \frac{1}{q\hat{R}_0 \hat{v}_{T_s}} \frac{\hat{n}_{s'} \sqrt{\hat{T}_s} \sqrt{\langle \hat{T}_{s,\text{coll}} \rangle_{\text{FS}}}}{\hat{T}_{\text{mean}}^{5/2}} \left(\frac{\hat{Z}_{s'}}{\hat{Z}_s} \right)^2 \hat{v}_{*s} \quad (\text{D.21})$$

where the velocity \hat{v}_{T_s} is calculated as $\hat{v}_{T_s} = \max(\hat{A}_s^{-1/2} \hat{v}_{T_s}, \hat{A}_{s'}^{-1/2} \hat{v}_{T_{s'}})$ where $\hat{v}_{T_s} = \sqrt{\hat{T}_s}$ and $\hat{v}_{T_{s'}} = \sqrt{\hat{T}_{s'}}$ and the collision frequencies $\hat{v}_{*s}, \hat{v}_{*s'}$ are linked by the relation (D.15).

D.7. Normalized source of impurity

Let us consider the species s as the major species and the species s' as an impurity species. The source $\hat{S}_{n_{s'}}(\hat{r}, \theta, \hat{v}_{G\parallel s}, \hat{\mu}_s)$ of impurity s' is defined by

$$\hat{S}_{n_{s'}} = \frac{\hat{S}_0^{n_{s'}} \hat{S}_r}{(2\pi \hat{T}_{s',\text{srce}})^{3/2}} \left(\frac{5}{2} - \hat{\mu}_{s'} - \hat{v}_{G\parallel s'}^2 \right) \times \exp\left(-\hat{v}_{G\parallel s'}^2 - \hat{\mu}_{s'}\right) \quad (\text{D.22})$$

where $\hat{v}_{G\parallel s'} = \hat{v}_{G\parallel s'}/\sqrt{2\hat{T}_{s',\text{srce}}}$ and $\hat{\mu}_{s'} = \hat{\mu}_{s'} \hat{B}/\hat{T}_{s',\text{srce}}$. $\hat{S}_0^{n_{s'}}$ corresponds to the normalized intensity of the source. To avoid any injection of charges, the injection of impurities must be compensated by the injection of source of matter for the majority species such that

$$Z_s \int S_{n_s} J_{v_s} d\hat{v}_{G\parallel} d\hat{\mu}_s + Z_{s'} \int S_{n_{s'}} J_{v_{s'}} d\hat{v}_{G\parallel} d\hat{\mu}_{s'} = 0$$

with J_{v_s} (resp. $J_{v_{s'}}$) the Jacobian in velocity space for species s (resp. species s'). The normalized radial profiles of the sources are assumed equal to \hat{S}_r . Therefore,

$$\hat{S}_{n_s} = \frac{\hat{S}_0^{n_s} \hat{S}_r}{(2\pi \hat{T}_{s,\text{srce}})^{3/2}} \left(\frac{5}{2} - \hat{\mu}_s - \hat{v}_{G\parallel s}^2 \right) e^{-\hat{v}_{G\parallel s}^2 - \hat{\mu}_s} \quad (\text{D.23})$$

with $\hat{S}_0^{n_s} = -\frac{\hat{Z}_{s'}}{\hat{Z}_s} \left(\frac{\hat{T}_{s',\text{srce}}}{\hat{T}_s} \right)^{3/2} \hat{S}_0^{n_{s'}}$.

In the code, the temperature profile of the density sources are taken equal, i.e. $\hat{T}_{s,\text{srce}} = \hat{T}_{s',\text{srce}}$.

Appendix E. Invariance

Let us consider a reference simulation without source terms. Let us also define a second simulation similar to the reference one but where the mass and charge have been respectively multiplied by a factor α_A and α_Z . Then, it is shown in this appendix that 7 control parameters ($\alpha_x, \alpha_t, \alpha_{Te}, \alpha_\phi, \alpha_{\text{coll}}, \alpha_{\text{diff}}$ and α_{Krook} that respectively rescale the space, the time, the electron temperature, the electrostatic potential, the collision operator, the diffusion term and the Krook operator) are sufficient to ensure that both simulations – reference and scaled – are equivalent. The constraints on the different control parameters are summarized in Table E.13 and the proof follows.

For the proof let us first consider the following normalized reference Vlasov equation for a species of charge \hat{Z}_s and

Table E.13

Scaling which must be applied to the different characteristic quantities to obtain an equivalence between any reference simulation and a scaled simulation.

	Charge	Mass	Length	Time	T_e	Elec. potential	Collision	Krook	Diffusion
Scaling	α_Z	α_A	$\sqrt{\alpha_A}/\alpha_Z$	α_A/α_Z	α_Z^{-1}	α_Z^{-1}	1	α_Z/α_A	α_Z^{-1}

mass \hat{A}_s

$$\begin{aligned} \frac{\partial \hat{F}_s}{\partial \hat{t}} + \left\{ \frac{1}{\sqrt{\hat{A}_s}} \hat{v}_{G\parallel} \hat{\mathbf{b}}_s^* + \left(\frac{\hat{v}_{G\parallel}^2 + \hat{\mu}_s \hat{B}}{\hat{Z}_s \hat{B}_{\parallel s}^* \hat{B}} \right) (\mathbf{b} \times \hat{\nabla} \hat{B}) \right. \\ \left. + \frac{1}{\hat{B}_{\parallel s}^*} (\mathbf{b} \times \hat{\nabla} \hat{\phi}) \right\} \cdot \hat{\nabla} \hat{F}_s \\ + \left(-\frac{1}{\sqrt{\hat{A}_s}} \hat{\mu}_s \hat{\mathbf{b}}_s^* \cdot \hat{\nabla} \hat{B} - \frac{\hat{Z}_s}{\sqrt{\hat{A}_s}} \hat{\mathbf{b}}_s^* \cdot \hat{\nabla} \hat{\phi} \right. \\ \left. + \hat{v}_{G\parallel} \hat{\mathbf{v}}_{E \times B_s} \cdot \hat{\nabla} \ln \hat{B} \right) \frac{\partial \hat{F}_s}{\partial \hat{v}_{G\parallel}} \\ = \frac{1}{\hat{B}_{\parallel s}^*} \frac{\partial}{\partial \hat{v}_{G\parallel}} \left[\hat{B}_{\parallel s}^* \hat{\mathcal{D}}_{\parallel s} \left(\frac{\partial \hat{F}_s}{\partial \hat{v}_{G\parallel}} + \frac{(\hat{v}_{G\parallel} - \hat{V}_{\parallel s, \text{coll}}) \hat{F}_s}{\hat{v}_{T_s, \text{coll}}^2} \right) \right] \\ + \frac{1}{\hat{B}_{\parallel s}^*} \left[\frac{1}{\hat{r}} \frac{\partial}{\partial \hat{r}} \left(\hat{r} \hat{\chi} \hat{B}_{\parallel s}^* \frac{\partial \hat{F}_s}{\partial \hat{r}} \right) \right] \\ - \hat{v}(\hat{r}) (\hat{F}_s - \hat{F}_{s, \text{eq}}) \end{aligned}$$

where

$$\hat{\mathbf{b}}_s^* = \frac{1}{\hat{B}_{\parallel s}^*} \left(\hat{\mathbf{B}} + \sqrt{\hat{A}_s} \frac{\hat{v}_{G\parallel}}{\hat{Z}_s \hat{B}} \hat{\nabla} \times \hat{\mathbf{B}} \right)$$

and

$$\hat{\mathcal{D}}_{\parallel s}(\hat{r}, \hat{v}) = \hat{\mathcal{A}}_s(\hat{r}) \left(\frac{\Phi(\hat{v}) - G(\hat{v})}{2\hat{v}} \right)$$

$$\text{with } \hat{\mathcal{A}}_s(\hat{r}) = \frac{1}{\sqrt{\hat{A}_s}} \left(3 \frac{\sqrt{\pi}}{2} \frac{\hat{v}_{T_s, \text{coll}}^3 \hat{\epsilon}^{3/2}}{q(\hat{r}) \hat{R}_0} \right) \hat{v}_{*s}.$$

The Chandrasekhar function G and the function Φ are defined by Eq. (27). Let us apply a scaling with the control parameters defined below, this leads to the following new Vlasov equation

$$\begin{aligned} \frac{1}{\alpha_t} \frac{\partial \hat{F}_s}{\partial \hat{t}} + \left\{ \frac{1}{\sqrt{\alpha_A \hat{A}_s}} \hat{v}_{G\parallel} \hat{\mathbf{b}}_s^* + \left(\frac{\hat{v}_{G\parallel}^2 + \hat{\mu}_s \hat{B}}{\alpha_Z \hat{Z}_s \hat{B}_{\parallel s}^* \hat{B}} \right) (\mathbf{b} \times \frac{1}{\alpha_x} \hat{\nabla} \hat{B}) \right. \\ \left. + \frac{1}{\hat{B}_{\parallel s}^*} (\mathbf{b} \times \frac{1}{\alpha_x} \hat{\nabla} (\alpha_\phi \hat{\phi})) \right\} \cdot \frac{\hat{\nabla} \hat{F}_s}{\alpha_x} \\ + \left(-\frac{1}{\sqrt{\alpha_A \hat{A}_s}} \hat{\mu}_s \hat{\mathbf{b}}_s^* \cdot \frac{\hat{\nabla} \hat{B}}{\alpha_x} - \frac{\alpha_Z \hat{Z}_s}{\sqrt{\alpha_A \hat{A}_s}} \hat{\mathbf{b}}_s^* \cdot \frac{\hat{\nabla} (\alpha_\phi \hat{\phi})}{\alpha_x} \right. \\ \left. + \hat{v}_{G\parallel} \frac{\alpha_\phi}{\alpha_x} \hat{\mathbf{v}}_{E \times B_s} \cdot \frac{1}{\alpha_x} \hat{\nabla} \ln \hat{B} \right) \frac{\partial \hat{F}_s}{\partial \hat{v}_{G\parallel}} \\ = \frac{1}{\hat{B}_{\parallel s}^*} \frac{\partial}{\partial \hat{v}_{G\parallel}} \left[\hat{B}_{\parallel s}^* \frac{\alpha_{\text{coll}}}{\sqrt{\alpha_A \alpha_x}} \hat{\mathcal{D}}_{\parallel s} \left(\frac{\partial \hat{F}_s}{\partial \hat{v}_{G\parallel}} + \frac{(\hat{v}_{G\parallel} - \hat{V}_{\parallel s, \text{coll}}) \hat{F}_s}{\hat{v}_{T_s, \text{coll}}^2} \right) \right] \end{aligned}$$

$$+ \frac{1}{\hat{B}_{\parallel s}^*} \left[\frac{1}{\alpha_x \hat{r}} \frac{\partial}{\partial \hat{r}} \left(\hat{r} \alpha_{\text{diff}} \hat{\chi} \hat{B}_{\parallel s}^* \frac{1}{\alpha_x} \frac{\partial \hat{F}_s}{\partial \hat{r}} \right) \right] - \alpha_{\text{Krook}} \hat{v}(\hat{r}) (\hat{F}_s - \hat{F}_{s, \text{eq}})$$

with

$$\hat{\mathbf{b}}_s^* = \frac{1}{\hat{B}_{\parallel s}^*} \left(\hat{\mathbf{B}} + \sqrt{\alpha_A \hat{A}_s} \frac{\hat{v}_{G\parallel}}{\alpha_Z \hat{Z}_s \hat{B}} \frac{\hat{\nabla} \times \hat{\mathbf{B}}}{\alpha_x} \right).$$

Concerning the left hand side, this equation is equivalent to the reference one, if and only if:

$$\frac{1}{\alpha_t} = \frac{1}{\sqrt{\alpha_A \alpha_x}} = \frac{1}{\alpha_Z \alpha_x^2} = \frac{\alpha_\phi}{\alpha_x^2} \quad (\text{E.1})$$

$$\frac{1}{\sqrt{\alpha_A} \alpha_x} = \frac{\alpha_Z \alpha_\phi}{\sqrt{\alpha_A \alpha_x}} = \frac{\alpha_\phi}{\alpha_x^2}. \quad (\text{E.2})$$

Therefore, according to the last equality of Eq. (E.2), $\alpha_x = \sqrt{\alpha_A}/\alpha_Z$. Besides, due to the last equality of Eq. (E.1), $\alpha_\phi = \alpha_Z^{-1}$. And finally, due to the first equality of Eq. (E.1), $\alpha_t = \sqrt{\alpha_A}/\alpha_x$, so $\alpha_t = \alpha_A/\alpha_Z$. Taking into account the collision operator $1/\alpha_t = \alpha_{\text{coll}}/(\sqrt{\alpha_A \alpha_x})$ which gives $\alpha_{\text{coll}} = 1$. In addition, the equivalence condition for the Krook operator leads to $1/\alpha_t = \alpha_{\text{Krook}}$ thus $\alpha_{\text{Krook}} = \alpha_Z/\alpha_A$ while for the diffusion term the condition reads $1/\alpha_t = \alpha_{\text{diff}}/\alpha_x^2$, i.e. $\alpha_{\text{diff}} = \alpha_Z^{-1}$.

Concerning the equivalence for the quasi-neutrality let us consider normalized equation

$$\begin{aligned} - \sum_s \hat{A}_s \hat{\nabla}_\perp \left(\frac{\hat{n}_{s, \text{eq}}}{\hat{B}} \hat{\nabla}_\perp \hat{\phi} \right) + \frac{1}{Z_0 \hat{T}_e} \sum_s \hat{Z}_s \hat{n}_{s, \text{eq}} \left[\hat{\phi} - \langle \hat{\phi} \rangle_{\text{FS}} \right] \\ = \sum_s \hat{Z}_s \int \hat{J}_{0s} (\hat{F}_s - \hat{F}_{s, \text{eq}}) d^3 \hat{\mathbf{v}}. \end{aligned}$$

Therefore, the rescaled equation reads:

$$\begin{aligned} - \frac{\alpha_A \alpha_\phi}{\alpha_x^2} \sum_s \hat{A}_s \hat{\nabla}_\perp \left(\frac{\hat{n}_{s, \text{eq}}}{\hat{B}} \hat{\nabla}_\perp \hat{\phi} \right) \\ + \frac{\alpha_Z \alpha_\phi}{\alpha_{T_e}} \frac{1}{Z_0 \hat{T}_e} \sum_s \hat{Z}_s \hat{n}_{s, \text{eq}} \left[\hat{\phi} - \langle \hat{\phi} \rangle_{\text{FS}} \right] \\ = \sum_s \alpha_Z \hat{Z}_s \int \hat{J}_{0s} (\hat{F}_s - \hat{F}_{s, \text{eq}}) d^3 \hat{\mathbf{v}}. \end{aligned}$$

The equivalence between reference and rescaled QN equations is ensured if and only if:

$$\frac{\alpha_A \alpha_\phi}{\alpha_x^2} = \frac{\alpha_Z \alpha_\phi}{\alpha_{T_e}} \Rightarrow \alpha_{T_e} = \frac{\alpha_x^2 \alpha_Z}{\alpha_A} \quad \text{and}$$

$$\alpha_Z = \frac{\alpha_Z \alpha_\phi}{\alpha_{T_e}} \Rightarrow \alpha_\phi = \alpha_{T_e}.$$

Therefore $\alpha_{T_e} = 1/\alpha_Z$ which confirms the previous equality $\alpha_\phi = \alpha_Z^{-1}$.

Finally, regarding the gyroaverage operator in the case of a Padé approximation, i.e. $\hat{J}_{0s} \sim 1 + \frac{1}{2} \frac{\hat{A}_s}{Z_s^2} \frac{\hat{\mu}_s}{\hat{B}} \hat{\nabla}_\perp^2$, its invariance is ensured provided the equality $\alpha_A = \alpha_Z^2 \alpha_x^2$ is fulfilled. This equality is already satisfied by the previous constraints.

Table F.14

Common parameters for GAM test. The velocity phase space is defined by $-\text{nb}_{v_{th0}} v_{T_{s0}} \leq v_{C||} \leq \text{nb}_{v_{th0}} v_{T_{s0}}$ and $0 \leq \mu \leq \mu_{\text{max}} T_0/B_0$. Torus indicates the fraction of the torus simulated. The radial density profile is defined by its gradient as $d \log n_{s0}(r)/dr = -\kappa_{ns0} \cosh^{-2}((r - r_{\text{peak}}/a)/\Delta r_{ns0})$. The same analytical expression is used for the temperature with κ_{Ts0} and Δr_{Ts0} .

ρ_*	A_s	Z_s	ϵ_0	r_{int}/a	r_{ext}/a	Torus	$\text{nb}_{v_{th0}}$
1/160	1.	1.	0.1	0.01	1.	1.	7.
μ_{max}	r_{peak}/a	κ_{ns0}	Δ_{ns0}	κ_{Ts0}	Δ_{Ts0}	T_i/T_e	
12.	0.5	$1.e^{-7}$	0.2	$1.e^{-7}$	0.1	1.	

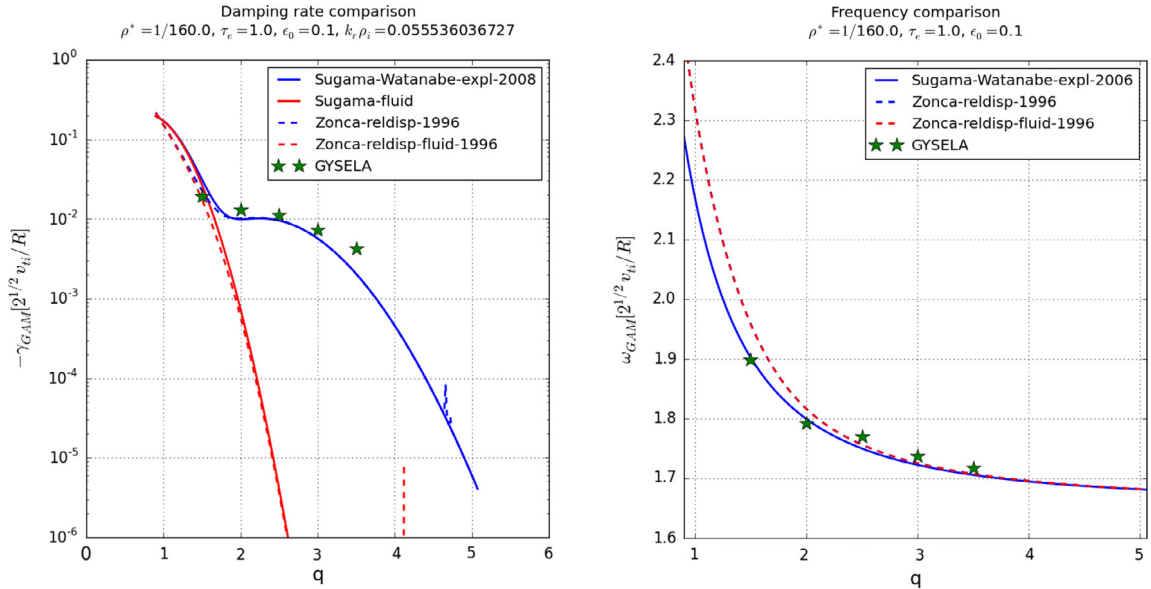


Fig. F.15. Damping rate (left) and frequency (right) of the electric field for simulation parameters given in Table F.14. Comparison with explicit analytical values given by Sugama and Watanabe [129] and Zonca [130] where FOW effects are taken into account or not.

Appendix F. Rosenbluth–Hinton test

In this appendix, we report on simulations of the so-called Rosenbluth–Hinton (R–H) test [110]. This consists in studying the collisionless relaxation of an initial $E \times B$ poloidal flow, including the transient GAM oscillation (Geodesic Acoustic Mode), towards a non vanishing residual value. Such simulations are interesting validation tests for gyrokinetic codes because the damping, the frequency and the residual value of the GAM can be compared to theoretical predictions [129,130]. In practice, a zonal perturbation in ion density is initialized, with a radial profile of the form $\sin(\pi r/a)$. This perturbation generates a zonal radial electric field which evolves in time as predicted by the R–H theory. The parameters used for the following simulations are the same as those used by Biancalani [115], namely: (i) an analytical circular equilibrium with large aspect ratio ($\epsilon = a/R = 0.1$); (ii) flat density and temperature profiles with $\tau = T_i/T_e = 1$ and (iii) flat q -profiles varying from $q = 1.5$ to 3.5 . All simulations are performed for a mesh $(N_r, N_\theta, N_\varphi, N_{v_{||}}, N_\mu) = (256, 256, 16, 128, 32)$. The results obtained with GYSELA are displayed in Figs. F.15, F.16, where the GAM frequency, the damping rate and the residual value are plotted as a function of the safety factor q . They are comparable to those published by the ORB5 team (see figures 2 and 3 in [115]). Consistently with the theory, the FOW (Finite Orbit Width) effects are already significant at moderate values of q (typically for $q \leq 2$, cf. Fig. F.15(a)). Regarding the residual values, two ratios are considered: either the ratio of the finite over the initial zonal electric potential, or the ratio of the radial electric fields. Both ratios would be equal if the radial profiles of the electric potential would not evolve in time, as assumed by the theory. As is evident from

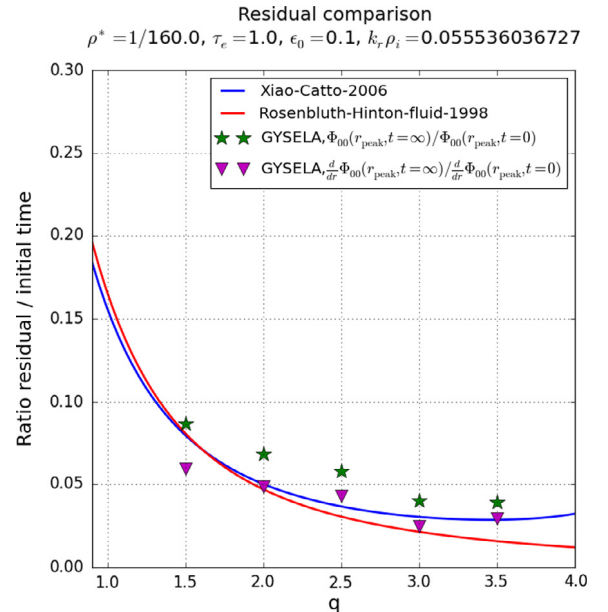


Fig. F.16. Residual values divided by the initial value of the electric potential (green stars) or electric field (magenta triangles) for the 5 different values of constant q profile: 1.5, 2., 2.5, 3. and 3.5. Comparison with analytical theory given by Rosenbluth–Hinton [110] (red line) and Xiao and Catto [131] (blue line). (For interpretation of the references to colour in this figure legend, the reader is referred to the web version of this article.)

Fig. F.16, this is actually not the case in these global simulations (see Fig. F.17).

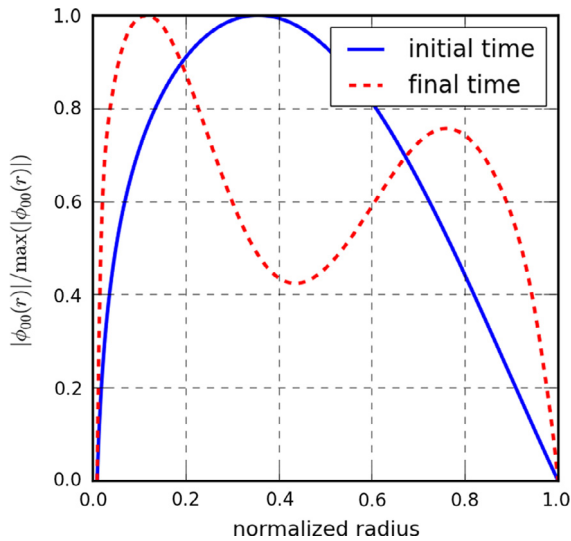


Fig. 17. Radial profile of the (0, 0) mode of ϕ at the initial time (blue line) and at the time $t = 30\,000/\Omega_{Ci}$ (red dotted line).

References

- [1] ITER Physics Expert Group on Confinement, Nucl. Fusion 39 (12) (1999) 2175. URL <http://stacks.iop.org/0029-5515/39/i=12/a=302>.
- [2] A. Brizard, T. Hahm, Rev. Modern Phys. 79 (2) (2007) 421–468.
- [3] J.A. Krommes, Annu. Rev. Fluid Mech. 44 (2012) 175–201.
- [4] X. Garbet, Y. Idomura, L. Villard, T. Watanabe, Nucl. Fusion 50 (4) (2010) 043002. URL <http://stacks.iop.org/0029-5515/50/i=4/a=043002>.
- [5] W. Dorland, F. Jenko, M. Kotschenreuther, B. Rogers, Phys. Rev. Lett. (85) (2000) 5579–5582.
- [6] F. Jenko, W. Dorland, M. Kotschenreuther, B. Rogers, Comput. Phys. Comm. (125) (2000) 196–209.
- [7] J. Candy, R. Waltz, J. Comput. Phys. 186 (2) (2003) 545–581.
- [8] A. Peeters, Y. Camenen, F. Casson, W. Hornsby, A. Snodin, D. Strintzi, G. Szepesi, Comput. Phys. Comm. 180 (12) (2009) 2650–2672.
- [9] W.W. Lee, Phys. Fluids 26 (2) (1983) 556–562. URL <http://link.aip.org/link/?PFL/26/556/1>.
- [10] S. Parker, W. Lee, Phys. Fluids B 5 (1) (1993) 77–86.
- [11] R. Sydora, V. Decyk, J. Dawson, Plasma Phys. Control. Fusion 38 (12A) (1996) A281. URL <http://stacks.iop.org/0741-3335/38/i=12A/a=021>.
- [12] A. Dimits, T. Williams, J. Byers, B. Cohen, Phys. Rev. Lett. 77 (1) (1996) 71–74.
- [13] Z. Lin, T.S. Hahm, W.W. Lee, W.M. Tang, R.B. White, Science 281 (5384) (1998) 1835–1837. URL <http://www.sciencemag.org/cgi/content/abstract/281/5384/1835>.
- [14] J.A. Heikkinen, T.P. Kiviniemi, T. Kurki-Suonio, A.G. Peeters, S.K. Sipilä, J. Comput. Phys. 173 (2) (2001) 527–548. URL <http://www.sciencedirect.com/science/article/B6WHY-45BC24W-1R2/8606267df6f0ff567b925c75c20a332a>.
- [15] Y. Idomura, S. Tokuda, Y. Kishimoto, M. Wakatani, Nucl. Fusion 41 (4) (2001) 437. URL <http://stacks.iop.org/0029-5515/41/i=4/a=308>.
- [16] A. Bottino, A.G. Peeters, R. Hatzky, S. Jolliet, B.F. McMillan, T.M. Tran, L. Villard, Phys. Plasmas 14 (1) (2007) 010701. URL <http://link.aip.org/link/?PHP/14/010701/1>.
- [17] S. Jolliet, A. Bottino, P. Angelino, R. Hatzky, T.M. Tran, B. Mcmillan, O. Sauter, K. Appert, Y. Idomura, L. Villard, Comput. Phys. Comm. 177 (5) (2007) 409–425. URL <http://www.sciencedirect.com/science/article/B6TJ5-4NVH804-1/2/bebb41e50006b7d2c03f86254d937951>.
- [18] W.X. Wang, T.S. Hahm, W.W. Lee, G. Rewoldt, J. Manickam, W.M. Tang, Phys. Plasmas 14 (7) (2007) 072306. URL <http://link.aip.org/link/?PHP/14/072306/1>.
- [19] C.S. Chang, S. Ku, P.H. Diamond, Z. Lin, S. Parker, T.S. Hahm, N. Samatova, Phys. Plasmas 056108 (5) (2009) 16.
- [20] W.M. Nevins, G.W. Hammett, A.M. Dimits, W. Dorland, D.E. Shumaker, Phys. Plasmas 12 (12) (2005) 122305. URL <http://link.aip.org/link/?PHP/12/122305/1>.
- [21] A.Y. Aydemir, Phys. Plasmas 1 (4) (1994) 822–831. URL <http://link.aip.org/link/?PHP/1/822/1>.
- [22] R. Hatzky, A. Könies, A. Mishchenko, J. Comput. Phys. 225 (1) (2007) 568–590. URL <http://www.sciencedirect.com/science/article/B6WHY-4MSPV7N-3/2/6314cfb7f80d279673263f7f6889b67e>.
- [23] R. Hatzky, T. Tran, A. Konies, R. Kleiber, S.J. Allfrey, Phys. Plasmas 9 (3) (2002) 898–912. URL <http://link.aip.org/link/?PHP/9/898/1>.
- [24] L. Villard, A. Bottino, S. Brunner, A. Casati, J. Chowdhury, T. Dannert, R. Ganesh, X. Garbet, T. Görler, V. Grandgirard, R. Hatzky, Y. Idomura, F. Jenko, S. Jolliet, S.K. Aghdam, X. Lapillonne, G. Latu, B.F. McMillan, F. Merz, Y. Sarazin, T.M. Tran, T. Vernay, Plasma Phys. Control. Fusion 52 (12) (2010) 124038. URL <http://stacks.iop.org/0741-3335/52/i=12/a=124038>.
- [25] J. Büchner, Adv. Methods Space Simul. (2007) 23–46.
- [26] M. Kotschenreuther, G. Rewoldt, W.M. Tang, Comput. Phys. Comm. 88 (2–3) (1995) 128–140. URL <http://www.sciencedirect.com/science/article/B6TJ5-40324V5-3/2/f5dfd72ad0f6e747cf2cb934e3d9fc26>.
- [27] F. Merz, Gyrokinetic simulation of multimode plasma turbulence (thesis), Universität Münster, 2009.
- [28] T.H. Watanabe, H. Sugama, Nucl. Fusion 46 (2006) 24–32.
- [29] A.G. Peeters, D. Strintzi, Phys. Plasmas 11 (8) (2004) 3748–3751. URL <http://link.aip.org/link/?PHP/11/3748/1>.
- [30] Y. Idomura, M. Ida, T. Kano, N. Aiba, S. Tokuda, Comput. Phys. Comm. 179 (6) (2008) 391–403. URL <http://www.sciencedirect.com/science/article/B6TJ5-4S85DNW-1/2/9d0bb7d210236534205003c368e38d7f>.
- [31] Y. Idomura, H. Urano, N. Aiba, S. Tokuda, Nucl. Fusion 49 (6) (2009) 065029. URL <http://stacks.iop.org/0029-5515/49/i=6/a=065029>.
- [32] V. Grandgirard, M. Brunetti, P. Bertrand, N. Besse, X. Garbet, P. Ghendrih, G. Manfredi, Y. Sarazin, O. Sauter, E. Sonnendrücker, J. Vaclavik, L. Villard, J. Comput. Phys. 217 (2) (2006) 395–423. URL <http://www.sciencedirect.com/science/article/pii/S0021999106000155>.
- [33] G. Dif-Pradalier, V. Grandgirard, Y. Sarazin, X. Garbet, P. Ghendrih, Commun. Nonlinear Sci. Numer. Simul. 13 (1) (2008) 65–71. Vlasovia 2006: The Second International Workshop on the Theory and Applications of the Vlasov Equation. URL <http://www.sciencedirect.com/science/article/pii/S1007570407001086>.
- [34] J. Abiteboul, X. Garbet, V. Grandgirard, S.J. Allfrey, P. Ghendrih, G. Latu, Y. Sarazin, A. Strugarek, Phys. Plasmas 18 (8) (2011) URL <http://scitation.aip.org/content/aip/journal/pop/18/8/10.1063/1.3620407>.
- [35] Y. Idomura, Comput. Sci. Discov. 5 (1) (2012) 014018. URL <http://stacks.iop.org/1749-4699/5/i=1/a=014018>.
- [36] Y. Idomura, M. Ida, S. Tokuda, L. Villard, J. Comput. Phys. 226 (1) (2007) 244–262. URL <http://www.sciencedirect.com/science/article/B6WHY-4NJWP0T-4/2/d311757a63c410232cc04ad156a01eab>.
- [37] V. Grandgirard, Y. Sarazin, Panor. Synthèses (39–40) (2013) 91–176.
- [38] J. Candy, R. Waltz, Phys. Rev. Lett. 91 (2003) 045001. URL <http://link.aps.org/doi/10.1103/PhysRevLett.91.045001>.
- [39] T. Goerler, X. Lapillonne, S. Brunner, T. Dannert, F. Jenko, S.K. Aghdam, P. Marcus, B.F. McMillan, F. Merz, O. Sauter, D. Told, L. Villard, Phys. Plasmas 18 (5) (2011) 056103. URL <http://link.aip.org/link/?PHP/18/056103/1>.
- [40] A. Bottino, B. Scott, S. Brunner, B. McMillan, T. Tran, T. Vernay, L. Villard, S. Jolliet, R. Hatzky, A. Peeters, IEEE Trans. Plasma Sci. 38 (9) (2010) 2129–2135.
- [41] W.A. Hornsby, P. Migliano, R. Buchholz, D. Zaroso, F.J. Casson, E. Poli, A.G. Peeters, Plasma Phys. Control. Fusion 57 (5) (2015) 054018. URL <http://stacks.iop.org/0741-3335/57/i=5/a=054018>.
- [42] on Verification Validation, T. G., Organization, U. B. P., Force, U. T. T., P.W. Terry, M. Greenwald, J.-N. Leboeuf, G.R. McKee, D.R. Mikkelsen, W.M. Nevins, D.E. Newman, D.P. Stotler, Phys. Plasmas 15 (6) (2008) 062503. URL <http://link.aip.org/link/?PHP/15/062503/1>.
- [43] G.L. Falchetto, B.D. Scott, P. Angelino, A. Bottino, T. Dannert, V. Grandgirard, S. Janhunen, F. Jenko, S. Jolliet, A. Kendl, B.F. McMillan, Y. Naulin, A.H. Nielsen, M. Ottaviani, A.G. Peeters, M.J. Pueschel, D. Reiser, T.T. Ribeiro, M. Romanelli, Plasma Phys. Control. Fusion 50 (12) (2008) 124015. URL <http://stacks.iop.org/0741-3335/50/i=12/a=124015>.
- [44] Y. Idomura, M. Nakata, S. Jolliet, Plasma Fusion Res. 9 (2014) 3503028.
- [45] Y. Idomura, Phys. Plasmas 21 (2) (2014). URL <http://scitation.aip.org/content/aip/journal/pop/21/2/10.1063/1.4867180>.
- [46] V. Grandgirard, Y. Sarazin, P. Angelino, A. Bottino, N. Crouseilles, G. Darmet, G. Dif-Pradalier, X. Garbet, P. Ghendrih, S. Jolliet, G. Latu, E. Sonnendrücker, L. Villard, Plasma Phys. Control. Fusion 49 (12B) (2007) B173. URL <http://stacks.iop.org/0741-3335/49/i=12B/a=516>.
- [47] D. Estève, X. Garbet, Y. Sarazin, V. Grandgirard, T. Cartier-Michaud, G. Dif-Pradalier, P. Ghendrih, G. Latu, C. Nordsini, Phys. Plasmas (22) (2015) 122506.
- [48] Y. Sarazin, V. Grandgirard, J. Abiteboul, S. Allfrey, X. Garbet, P. Ghendrih, G. Latu, A. Strugarek, G. Dif-Pradalier, Nucl. Fusion 50 (5) (2010) 054004. URL <http://stacks.iop.org/0029-5515/50/i=5/a=054004>.
- [49] G. Dif-Pradalier, P.H. Diamond, V. Grandgirard, Y. Sarazin, J. Abiteboul, X. Garbet, P. Ghendrih, A. Strugarek, S. Ku, C.S. Chang, Phys. Rev. E 82 (2010) 025401. URL <http://link.aps.org/doi/10.1103/PhysRevE.82.025401>.
- [50] X. Garbet, G. Dif-Pradalier, C. Nguyen, Y. Sarazin, V. Grandgirard, P. Ghendrih, Phys. Plasmas 16 (6) (2009). URL <http://scitation.aip.org/content/aip/journal/pop/16/6/10.1063/1.3153328>.
- [51] G. Dif-Pradalier, P.H. Diamond, V. Grandgirard, Y. Sarazin, J. Abiteboul, X. Garbet, P. Ghendrih, G. Latu, A. Strugarek, S. Ku, C.S. Chang, Phys. Plasmas 18 (6) (2011). URL <http://scitation.aip.org/content/aip/journal/pop/18/6/10.1063/1.3592652>.
- [52] G. Dif-Pradalier, V. Grandgirard, Y. Sarazin, X. Garbet, P. Ghendrih, Phys. Rev. Lett. 103 (2009) 065002. URL <http://link.aps.org/doi/10.1103/PhysRevLett.103.065002>.
- [53] Y. Sarazin, V. Grandgirard, J. Abiteboul, S. Allfrey, X. Garbet, P. Ghendrih, G. Latu, A. Strugarek, G. Dif-Pradalier, P. Diamond, S. Ku, C. Chang, B. McMillan, T. Tran, L. Villard, S. Jolliet, A. Bottino, P. Angelino, Nucl. Fusion 51 (10) (2011) 103023. URL <http://stacks.iop.org/0029-5515/51/i=10/a=103023>.

- [54] A. Strugarek, Y. Sarazin, D. Zarzoso, J. Abiteboul, A.S. Brun, T. Cartier-Michaud, G. Dif-Pradalier, X. Garbet, P. Ghendrih, V. Grandgirard, G. Latu, C. Passeron, O. Thomine, *Plasma Phys. Control. Fusion* 55 (7) (2013) 074013. URL <http://stacks.iop.org/0741-3335/55/i=7/a=074013>.
- [55] A. Strugarek, Y. Sarazin, D. Zarzoso, J. Abiteboul, A.S. Brun, T. Cartier-Michaud, G. Dif-Pradalier, X. Garbet, P. Ghendrih, V. Grandgirard, G. Latu, C. Passeron, O. Thomine, *Phys. Rev. Lett.* 111 (2013) 145001. URL <http://link.aps.org/doi/10.1103/PhysRevLett.111.145001>.
- [56] G. Dif-Pradalier, G. Hornung, P. Ghendrih, Y. Sarazin, F. Clairet, L. Vermare, P.H. Diamond, J. Abiteboul, T. Cartier-Michaud, C. Ehrlacher, D. Esteve, X. Garbet, V. Grandgirard, O. Gürcan, P. Hennequin, Y. Kosuga, G. Latu, P. Maget, P. Morel, C. Norscini, R. Sabot, A. Storelli, *Phys. Rev. Lett.* 114 (2015) 085004. URL <http://link.aps.org/doi/10.1103/PhysRevLett.114.085004>.
- [57] N. Crouseilles, A. Ratnani, E. Sonnendrücker, *J. Comput. Phys.* 231 (2) (2012) 373–393. URL <http://dx.doi.org/10.1016/j.jcp.2011.09.004>.
- [58] Y. Sarazin, V. Grandgirard, E. Fleurence, X. Garbet, P. Ghendrih, P. Bertrand, G. Depret, *Plasma Phys. Control. Fusion* 47 (10) (2005) 1817–1840. URL <http://stacks.iop.org/0741-3335/47/i=10/a=013>.
- [59] N. Crouseilles, M. Mehrenberger, H. Sellama, Numerical solution of the gyroaverage operator for the finite gyroradius guiding-center model, *CICP*, 1, 2010.
- [60] C. Steiner, M. Mehrenberger, N. Crouseilles, V. Grandgirard, G. Latu, F. Rozar, *Eur. Phys. J. D* 69 (1) (2015) 18. URL <http://dx.doi.org/10.1140/epjd/e2014-50211-7>.
- [61] F. Rozar, Ch. Steiner, G. Latu, M. Mehrenberger, V. Grandgirard, J. Bigot, T. Cartier-Michaud, J. Roman, *CEMRACS 2014*. Vol. submitted of ESAIM: Proc. Luminy, France, 2015.
- [62] P. Angelino, A. Bottino, R.H., et al., *Phys. Plasmas* 13 (2006) 052304.
- [63] G. Dif-Pradalier, V. Grandgirard, Y. Sarazin, X. Garbet, P. Ghendrih, P. Angelino, *Phys. Plasmas* 15 (4) (2008). URL <http://scitation.aip.org/content/aip/journal/pop/15/4/10.1063/1.2904901>.
- [64] L. Landau, *Phys. Z. Sowj. Union* 10 (1936).
- [65] R. Hazeltine, J. Meiss, *Plasma Confinement*, Dover publication, 2003.
- [66] X. Xu, M. Rosenbluth, *Phys. Fluids B* 3 (1991).
- [67] A. Lenard, I. Bernstein, *Phys. Rev.* 112 (5) (1958).
- [68] P. Helander, D. Sigmar, *Collisional Transport in Magnetized Plasmas*, in: Cambridge Monographs on Plasma Physics, Cambridge University Press, 2005. URL <http://books.google.fr/books?id=nm-V01E0H2MC>.
- [69] G. Darmet, P. Ghendrih, Y. Sarazin, X. Garbet, V. Grandgirard, *Commun. Nonlinear Sci. Numer. Simul.* 13 (1) (2008) 53–58. *vlavsovia 2006: The Second International Workshop on the Theory and Applications of the Vlasov Equation*. URL <http://www.sciencedirect.com/science/article/pii/S1007570407001104>.
- [70] G.Y. Fu, *Phys. Rev. Lett.* 101 (2008) 185002. URL <http://link.aps.org/doi/10.1103/PhysRevLett.101.185002>.
- [71] R. Nazikian, G.Y. Fu, M.E. Austin, H.L. Berk, R.V. Budny, N.N. Gorelenkov, W.W. Heidbrink, C.T. Holcomb, G.J. Kramer, G.R. McKee, M.A. Makowski, W.M. Solomon, M. Shafer, E.J. Strait, M.A. V. Zeeland, *Phys. Rev. Lett.* 101 (2008) 185001. URL <http://link.aps.org/doi/10.1103/PhysRevLett.101.185001>.
- [72] D. Zarzoso, X. Garbet, Y. Sarazin, R. Dumont, V. Grandgirard, *Phys. Plasmas* 19 (2) (2012). URL <http://scitation.aip.org/content/aip/journal/pop/19/2/10.1063/1.3680633>.
- [73] D. Zarzoso, Y. Sarazin, X. Garbet, R. Dumont, A. Strugarek, J. Abiteboul, T. Cartier-Michaud, G. Dif-Pradalier, P. Ghendrih, V. Grandgirard, G. Latu, C. Passeron, O. Thomine, *Phys. Rev. Lett.* 110 (2013) 125002. URL <http://link.aps.org/doi/10.1103/PhysRevLett.110.125002>.
- [74] R.J. Dumont, D. Zarzoso, Y. Sarazin, X. Garbet, A. Strugarek, J. Abiteboul, T. Cartier-Michaud, G. Dif-Pradalier, P. Ghendrih, J.-B. Girardo, V. Grandgirard, G. Latu, C. Passeron, O. Thomine, *Plasma Phys. Control. Fusion* 55 (12) (2013) 124012. URL <http://stacks.iop.org/0741-3335/55/i=12/a=124012>.
- [75] A. Biancalani, G. Merlo, V. Grandgirard, *Phys. Plasmas* (2016) in preparation.
- [76] A. Staniforth, J. Côté, *Mon. Weather Rev.* (119) (1991) 2206–2223.
- [77] D.R. Durran, *Numerical Methods for Wave Equations in Geophysical Fluid Dynamics*, Springer-Verlag, New York, 1998.
- [78] E. Sonnendrücker, J. Roche, P. Bertrand, A. Ghizzo, *J. Comput. Phys.* 149 (2) (1999) 201–220. URL <http://www.sciencedirect.com/science/article/B6WHY-45N4MIT-P/2/33ccd197dc83781b3eeca522915cf31a>.
- [79] G. Depret, X. Garbet, P. Bertrand, A. Ghizzo, *Plasma Phys. Control. Fusion* 23 (42) (2000) 949–971.
- [80] M. Brunetti, V. Grandgirard, O. Sauter, J. Vaclavik, L. Villard, *Comput. Phys. Comm.* 163 (1) (2004) 1–21. URL <http://www.sciencedirect.com/science/article/pii/S0010465504004126>.
- [81] Y. Sarazin, V. Grandgirard, G. Dif-Pradalier, X. Garbet, P. Ghendrih, *Phys. Plasmas* 13 (9) (2006) URL <http://scitation.aip.org/content/aip/journal/pop/13/9/10.1063/1.2345177>.
- [82] C. Cheng, G. Knorr, *J. Comput. Phys.* (22) (1976) 330–351.
- [83] T. Nakamura, T. Yabe, *Comput. Phys. Comm.* (120) (1999) 122–154.
- [84] N. Crouseilles, T. Respaud, E. Sonnendrücker, *Comput. Phys. Comm.* 180 (10) (2009) 1730–1745. URL <http://www.sciencedirect.com/science/article/B6TJ5-4W6YDWD-1/2/167e84bc1301fbd8173a59997068fd5f>.
- [85] N. Crouseilles, M. Mehrenberger, E. Sonnendrücker, *J. Comput. Phys.* 229 (6) (2010) 1927–1953. URL <http://www.sciencedirect.com/science/article/B6WHY-4XSTDBW-1/2/ed303f797cb08e5769bc541b055ce745>.
- [86] J.P. Braeunig, N. Crouseilles, M. Mehrenberger, E. Sonnendrücker, *Discrete Contin. Dyn. Syst. Ser. S* 5 (3) (2012).
- [87] M. Zerroukat, N. Wood, A. Staniforth, *J. Comput. Phys.* 225 (1) (2007) 935–948.
- [88] G. Latu, V. Grandgirard, J. Abiteboul, M. Bergot, N. Crouseilles, X. Garbet, P. Ghendrih, M. Mehrenberger, Y. Sarazin, H. Sellama, E. Sonnendrücker, D. Zarzoso, Accuracy of Unperturbed Motion of Particles in a Gyrokinetic Semi-lagrangian Code, INRIA Research Report RR-8054, Sep. 2012. URL <https://hal.inria.fr/hal-00727118>.
- [89] J.-P. Braeunig, N. Crouseilles, V. Grandgirard, G. Latu, M. Mehrenberger, E. Sonnendrücker, Some Numerical Aspects of the Conservative PSM Scheme in a 4D Drift-kinetic Code. Inria research report, Dec. 2011. URL <https://hal.archives-ouvertes.fr/hal-00650343>.
- [90] F. Filbet, E. Sonnendrücker, P. Bertrand, *J. Comput. Phys.* (172) (2001) 166–187.
- [91] N. Besse, M. Mehrenberger, *Math. Comp.* 77 (61) (2008) 93–123.
- [92] G. Strang, *SIAM J. Numer. Anal.* 5 (1968) 506–517.
- [93] G. Latu, V. Grandgirard, J. Abiteboul, N. Crouseilles, G. Dif-Pradalier, X. Garbet, P. Ghendrih, M. Mehrenberger, E. Sonnendrücker, Y. Sarazin, *Eur. Phys. J. D* 68 (11) (2014). URL <http://dx.doi.org/10.1140/epjd/e2014-50209-1>.
- [94] J. Abiteboul, P. Ghendrih, V. Grandgirard, T. Cartier-Michaud, G. Dif-Pradalier, X. Garbet, G. Latu, C. Passeron, Y. Sarazin, A. Strugarek, O. Thomine, D. Zarzoso, *Plasma Phys. Control. Fusion* 55 (7) (2013) 074001. URL <http://stacks.iop.org/0741-3335/55/i=7/a=074001>.
- [95] N. Crouseilles, G. Latu, E. Sonnendrücker, *Int. J. Appl. Math. Comput. Sci.* 17 (3) (2007) 335–349.
- [96] N. Crouseilles, G. Latu, E. Sonnendrücker, *J. Comput. Phys.* 228 (5) (2009) 1429–1446. URL <http://www.sciencedirect.com/science/article/B6WHY-4TY49KC-1/2/82184ee239ba986cedec625fba35dc3>.
- [97] G. Latu, N. Crouseilles, V. Grandgirard, E. Sonnendrücker, Recent Advances in Parallel Virtual Machine and Message Passing Interface, in: *Lecture Notes in Computer Science*, vol. 4757, Springer, Paris, France, 2007, pp. 356–364. URL <http://hal.archives-ouvertes.fr/hal-00605748>.
- [98] G. Latu, V. Grandgirard, N. Crouseilles, R. Belouar, E. Sonnendrücker, Some Parallel Algorithms for the Quasineutrality Solver of GYSELA, INRIA Research Report RR-7591, Apr. 2011. URL <https://hal.inria.fr/inria-00583521>.
- [99] G. Latu, N. Crouseilles, V. Grandgirard, Parallel Bottleneck in the Quasineutrality Solver Embedded in GYSELA, INRIA Research Report RR-7595, Apr. 2011. URL <https://hal.inria.fr/inria-00583689>.
- [100] G. Latu, V. Grandgirard, N. Crouseilles, G. Dif-Pradalier, Scalable Quasineutral Solver for Gyrokinetic Simulation, Research Report RR-7611, INRIA, May 2012. URL <http://hal.inria.fr/inria-00590561>.
- [101] J. Bigot, V. Grandgirard, G. Latu, C. Passeron, F. Rozar, O. Thomine, *CEMRACS 2012*, ESAIM: Proc. Luminy, vol. 43, France, 2013, pp. 117–135.
- [102] F. Rozar, G. Latu, J. Roman, V. Grandgirard, *Concurr. Comput. Pract. Exper.* 27 (4) (2015) 994–1009. URL <http://dx.doi.org/10.1002/cpe.3429>.
- [103] F. Cappello, *Int. J. High Perform. Comput. Appl.* 23 (3) (2009) 212–226. URL <http://dx.doi.org/10.1177/1094342009106189>.
- [104] B. Schroeder, G. Gibson, *IEEE Trans. Dependable Secure Comput.* 7 (4) (2010).
- [105] O. Thomine, J. Bigot, V. Grandgirard, G. Latu, C. Passeron, F. Rozar, *CEMRACS 2012*, in: ESAIM: Proc. Luminy, vol. 43, France, 2013, pp. 108–116.
- [106] L. Bautista-Gomez, S. Tsuboi, D. Komatitsch, F. Cappello, N. Maruyama, S. Matsuoka, *Proc. Int. Conf. High Perform. Comput. Netw. Storage Anal. (SC11)* 17 (5) (2011) 1–32.
- [107] J. Bigot, T. Cartier-Michaud, V. Grandgirard, G. Latu, C. Passeron, F. Rozar, An approach to increase reliability of HPC simulation, application to the GYSELA5D code, in: *CEMRACS 2014*. Vol. submitted of ESAIM: Proc. Luminy, France, 2015.
- [108] J. Candy, R.E. Waltz, W. Dorland, *Phys. Plasmas* 11 (5) (2004) L25–L28. URL <http://scitation.aip.org/content/aip/journal/pop/11/5/10.1063/1.1695358>.
- [109] B.F. McMillan, X. Lapillonne, S. Brunner, L. Villard, S. Jolliet, A. Bottino, T. Görler, F. Jenko, *Phys. Rev. Lett.* 105 (2010) 155001. URL <http://link.aps.org/doi/10.1103/PhysRevLett.105.155001>.
- [110] M. Rosenbluth, F. Hinton, *Phys. Rev. Lett.* 80 (4) (1998).
- [111] V. Grandgirard, Y. Sarazin, X. Garbet, G. Dif-Pradalier, P. Ghendrih, N. Crouseilles, G. Latu, E. Sonnendrücker, N. Besse, P. Bertrand, *Commun. Nonlinear Sci. Numer. Simul.* 13 (1) (2008) 81–87. *vlavsovia 2006: The Second International Workshop on the Theory and Applications of the Vlasov Equation*. URL <http://www.sciencedirect.com/science/article/pii/S1007570407001220>.
- [112] A.M. Dimits, G. Bateman, M.A. Beer, B.I. Cohen, W. Dorland, G.W. Hammett, C. Kim, J.E. Kinsey, M. Kotschenreuther, A.H. Kritz, et al., *Phys. Plasmas* 7 (3) (2000) 969–983. URL <http://link.aip.org/link/?PHP/7/969/1>.
- [113] C.S. Chang, S. Ku, *Phys. Plasmas* 15 (6) (2008) 062510.
- [114] F. Hinton, M. Rosenbluth, *Plasma Phys. Control. Fusion* 41 (1999).
- [115] A. Biancalani, A. Bottino, P. Lauber, D. Zarzoso, *Nucl. Fusion* 54 (10) (2014) 104004. URL <http://stacks.iop.org/0029-5515/54/i=10/a=104004>.
- [116] X. Lapillonne, B.F. McMillan, T. Görler, S. Brunner, T. Dannert, F. Jenko, F. Merz, L. Villard, *Phys. Plasmas* 17 (11) (2010). URL <http://scitation.aip.org/content/aip/journal/pop/17/11/10.1063/1.3518118>.
- [117] T. Goerler, N. Tronko, W. Hornsby, R. Kleiber, C. Norscini, V. Grandgirard, F. Jenko, E. Sonnendrücker, *Phys. Plasmas* (2016) in press.
- [118] F.I. Parra, P.J. Catto, *Plasma Phys. Control. Fusion* 50 (6) (2008) 065014.
- [119] F.I. Parra, P.J. Catto, *Phys. Plasmas* 17 (5) (2010) 056106.
- [120] A.J. Brizard, *Phys. Plasmas* 17 (11) (2010) 112503.
- [121] B.D. Scott, J. Smirnov, *Phys. Plasmas* 17 (11) (2010) 112302.
- [122] A.J. Brizard, N. Tronko, *Phys. Plasmas* 18 (8) (2011) 082307.

- [123] J. Abiteboul, Turbulent and neoclassical toroidal momentum transport in tokamak plasmas (thesis), Aix-Marseille Université, 2012, URL <https://tel.archives-ouvertes.fr/tel-00777996>.
- [124] W.M. Manheimer, E. Ott, W.M. Tang, *Phys. Fluids* 20 (5) (1977) 806.
- [125] R.E. Waltz, G.M. Staebler, W. Dorland, G.W. Hammett, M. Kotschenreuther, J.A. Konings, *Phys. Plasmas* 4 (7) (1997) 2482–2496. URL <http://link.aip.org/link/?PHP/4/2482/1>.
- [126] F.L. Hinton, R.E. Waltz, *Phys. Plasmas* 13 (10) (2006) 102301.
- [127] R.E. Waltz, G.M. Staebler, *Phys. Plasmas* 15 (1) (2008) 014505.
- [128] X. Garbet, D. Esteve, Y. Sarazin, J. Abiteboul, C. Bourdelle, G. Dif-Pradalier, P. Ghendrih, V. Grandgirard, G. Latu, A. Smolyakov, *Phys. Plasmas* 20 (7) (2013). URL <http://scitation.aip.org/content/aip/journal/pop/20/7/10.1063/1.4816021>.
- [129] H. Sugama, T.-H. Watanabe, *Phys. Plasmas* 13 (012501) (2006).
- [130] F. Zonca, L. Chen, R. Santoro, *Plasma Phys. Control. Fusion* 38 (11) (1996) 2011. URL <http://stacks.iop.org/0741-3335/38/i=11/a=011>.
- [131] Y. Xiao, P.J. Catto, *Phys. Plasmas* 13 (10) (2006). URL <http://scitation.aip.org/content/aip/journal/pop/13/10/10.1063/1.2358497>.